

SINGLE MOLECULE DNA MANIPULATION AND ANALYSIS USING
NANOFLUIDIC CIRCUITS

Jinsheng Zhou

A dissertation submitted to the faculty of the University of North Carolina at Chapel Hill in
partial fulfillment of the requirements for the degree of Doctor of Philosophy in the
Department of Chemistry.

Chapel Hill
2013

Approved by:

J. Michael Ramsey

Royce W. Murray

Michael Rubinstein

James W. Jorgenson

Eric M. Brustad

©2013
Jinsheng Zhou
ALL RIGHTS RESERVED

ABSTRACT

Jinsheng Zhou: Single Molecule DNA Manipulation and Analysis using Nanofluidic Circuits
(Under the direction of J. Michael Ramsey)

Nanofluidic devices have emerged as new powerful tools for biomolecule analysis. Their utility in probing single DNA molecules is of particular interest because of both the biological importance and the ideal polymer physical properties of DNA. Such applications often involve an initial step of capturing the large, globule-shaped molecules from bulk solution and linearizing them in the nanoscale confining structures. The entropic barrier inherent to this process is typically overcome by pulling DNA into a nanoconduit using a large electric field. The resulting high velocity of molecular transport, coupled with the finite temporal resolution of detection, can make single-molecule characterizations difficult.

In this dissertation, novel three-dimensional nanofunnels are described that address this problem. Focused ion beam milling is developed to fabricate complex nanostructures. The nanofunnels facilitate the capture process, enabling the introduction of DNA molecules into fluidic nanochannels with significantly lower electric fields.

The gradual confinement change of the nanofunnel produces an entropy gradient for DNA molecules transitioning from bulk solution to a nanochannel. Tuning the electric field results in the stable trapping of a single DNA molecule in the nanofunnel. The precisely defined geometry enables an accurate force analysis on the molecule. For confined

molecules placed in an electric field, electro-hydrodynamic interactions are discovered that differ from those present in freely diffusing or anchored molecules.

Concentration polarization, a phenomenon unique to nanofluidics, is also described for devices containing a nanochannel-nanofunnel structure. The phenomenon is found to correlate with the ionic current rectification, an effect which was previously studied primarily in conical pores. Both phenomena are found to evolve over several minutes in the nanochannel-nanofunnel devices. Moreover, the electro-osmotic flow is found to greatly affect the concentration polarization and ionic current rectification.

The discoveries presented in this dissertation have both theoretical and practical importance. A better understanding of the entropic and electrohydrodynamic forces on a large polyion (DNA) was achieved. The nanofunnels developed here have potential applications in nanofluidics-based DNA mapping and sequencing technologies and in the pre-concentration of biomolecules for subsequent on-chip separations or analyses.

ACKNOWLEDGEMENTS

I would like to thank my advisor, Dr. J Michael Ramsey, for the opportunity to work on this exciting project, and for his generous support and guidance. I also thank all members of Ramsey group for making this five years so memorable. Especially, Dr. Laurent D. Menard and J. P. Alarie have been of great help all the time. I would also like to thank my collaborator, Dr. Michael Rubinstein and his group members for all the stimulating discussion. Finally, I thank my parents, my sister, and my girlfriend for all the support on every part of my life, without which the pursuit of my degree wouldn't be possible.

TABLE OF CONTENTS

LIST OF TABLES	x
LIST OF FIGURES	xi
LIST OF ABBREVIATIONS	xiv
LIST OF SYMBOLS	xvii
Chapter 1: DNA, Sequencing, and the Utility of Nanofluidic Devices	1
1.1 DNA	1
1.1.1 A Historical Perspective	1
1.1.2 DNA Sequencing Technologies.....	3
1.1.2.1 Sanger Sequencing	3
1.1.2.2 Next Generation Sequencing (NGS) Methods	4
1.1.3 Physical Properties of DNA.....	7
1.2 Basic Electrokinetics	9
1.2.1 Electrostatics	9
1.2.1.1 Ion Pairs and the Bjerrum Length.....	10
1.2.1.2 Charge Distribution near a Polyion	10
1.2.1.3 Charge Distribution near a Surface	11
1.2.1.4 The Electric Double Layer and the Zeta Potential	13
1.2.2 Electrophoresis and Electroosmosis	14
1.3 DNA Analysis Using Nanopores and Nanochannels	16

1.3.1	Nanopores	16
1.3.2	Nanochannels	20
1.4	Research Objectives	24
1.5	REFERENCES	25
1.6	Figures	31
Chapter 2: Fabrication of Nanofluidic Elements		41
2.1	Introduction	41
2.1.1	Thin Membrane Nanopores	41
2.1.2	Planar Nanochannels	44
2.2	Milling Three-Dimensional Features using a Focused Ion Beam	46
2.2.1	Instrumentation	46
2.2.2	Relationship between Ion Dose and Feature Depth	48
2.2.3	Milling Nanochannels with Integrated Three-Dimensional Nanofunnels	49
2.3	Milling Nanofluidic Structures using Multiple Ion Beam Currents	50
2.3.1	Motivation and Challenges	50
2.3.2	Milling 20-nm Nanochannels with Integrated Nanofunnels	51
2.4	Fabrication of Nanochannels using a Focused Electron Beam	52
2.4.1	Introduction	52
2.4.2	Trials using a High Energy (200 kV) Electron Beam	54
2.4.3	Material Damage on Quartz Substrates using a Low Energy (10 kV) Beam ...	54
2.5	Conclusion and Future Directions	55
2.6	REFERENCES	56
2.7	Tables and Figures	60

Chapter 3: Capture of DNA Molecules Using Three-Dimensional Nanofunnel-Nanochannel Devices	68
3.1 Introduction	68
3.1.1 Background	68
3.1.2 Three-Dimensional Nanofunnel Design	71
3.2 Materials and Methods	73
3.2.1 Device fabrication	73
3.2.2 Measurement of Translocation Event Frequency	74
3.2.3 Determining the Threshold Voltage.....	75
3.4 Conclusion.....	80
3.5 REFERENCES	82
3.6 Figures	85
Chapter 4: Trapping Single DNA Molecules in a Three-Dimensional Nanofunnel.....	93
4.1 Introduction	93
4.2 Materials and Methods	97
4.3 Results and Discussion.....	98
4.4 Conclusion.....	104
4.5 REFERENCES	105
4.6 Figures	107
Chapter 5: Concentration Polarization in Three-Dimensional Nanofunnel Systems	114
5.1 Introduction	114
5.2 Materials and Methods	119
5.3 Results and Discussion.....	120
5.4 Conclusion and Future Directions.....	127

5.5	REFERENCES.....	128
5.6	Figures.....	131

LIST OF TABLES

Table 2.1 Probe size and the milling time required for sputtering a $1\mu\text{m}\times 1\mu\text{m}\times 1\mu\text{m}$ cubic volume at different ion beam currents.	64
---	----

LIST OF FIGURES

Figure 1.1 Translocation of ss-DNA or RNA through an α -hemolysin nanopore.....	31
Figure 1.2 DNA unzipping experiments.	32
Figure 1.3 DNA translocation through solid-state nanopores in various folded configurations.	33
Figure 1.4 Discrimination between unlabeled nucleoside monophosphate molecules using a modified protein nanopore.	34
Figure 1.5 Reading DNA sequence using a nanopore and polymerase.	35
Figure 1.6 Schematic of nanochannel DNA confinement in different regimes.	36
Figure 1.7 Summary of experimental results (black symbols) and simulation results (red circles) showing the scaling of the confined DNA extension length with channel dimensions.	37
Figure 1.8 Various dynamic processes observed for a DNA molecule within a nanochannel.	38
Figure 1.9 An entropic trap array for DNA separation.	39
Figure 1.10 DNA mapping using nanochannels.	40
Figure 2.1 Nanopores fabricated using different types of high energy beams.	60
Figure 2.2 Nanostructures milled using a focused electron beam. The JEOL 2010F-FasTEM was operated at 200 keV to mill these features.	61
Figure 2.3 A photo of the FEI Helios 600 Nanolab TM DualBeam TM instrument.	61
Figure 2.4 Linear relationship between the dwell time and the milled depth.	62
Figure 2.5 Bitmap images and the patterns milled according to these images.	63
Figure 2.6 SEM images showing the steps of milling a 20 nm wide nanochannel with a three-dimensional nanofunnel.	65
Figure 2.7 Secondary electron images showing the contamination in the STEM.	66
Figure 2.8 Damage induced by a 10 kV electron beam.	67

Figure 3.1 The experiment and the three dimensional nanofunnel designs.....	85
Figure 3.2 Schematic representation of the nanofluidic device fabrication.....	86
Figure 3.3 Schematic representation of the capture frequency measurements.	87
Figure 3.4 Schematic representation of the threshold electric field measurements.....	88
Figure 3.5 Qualitative picture of the free energy landscape of the DNA translocation without or with a funnel.	89
Figure 3.6 Translocation frequency results showing that a nanofunnel decreases the energy barrier for DNA threading.	90
Figure 3.7 Effect of DNA accumulation when the energy barrier for translocation is significant.	91
Figure 3.8 Threshold electric field as a function of α	92
Figure 4.1 Trapping single DNA molecules in a three dimensional nanofunnel.	107
Figure 4.2 Energy landscape for a single Kuhn segment of the DNA molecule in funnels with different shapes.	108
Figure 4.3 The data processing of the videos using a Matlab program.	109
Figure 4.4 Trapping a single DNA molecule in the nanofunnel: location changes as a function of field.....	110
Figure 4.5 Trapping a single DNA molecule in the nanofunnel.	111
Figure 4.6 Electrohydrodynamic flow profiles for DNA molecule in different systems.....	112
Figure 4.7 Dependence of the leading end of the DNA molecule in the nanofunnel (x_0) on the nanochannel electric field.	113
Figure 5.1 Schematic showing the concentration polarization.	131
Figure 5.2 Experiment configurations.	132
Figure 5.3 Fluorescence intensity change showing the concentration polarization under an electric field.	133
Figure 5.4 Data processing for constructing Figure 5.5.....	134
Figure 5.5 Simultaneous measurements of the optical and the electrical signal indicating concentration polarization.	135

Figure 5.6 Current and resistance changes reflecting the CP propagation at different voltages for a solution of fluorescein in 0.1x TBE, no PVP.....	136
Figure 5.7 Current traces and current ratios showing the concentration polarization as affected by voltage and EOF.	137

LIST OF ABBREVIATIONS

A	adenine
AFM	atomic force microscopy
ALD	atomic layer deposition
BOE	buffered oxide etch
Bp	base pairs
C	cytosine
CP	concentration polarization
DBL	diffusive boundary layer
ddATP	dideoxyadenosine triphosphate
ddCTP	dideoxycytidine triphosphates
ddGTP	dideoxyguanosine triphosphates
ddNTP	dideoxynucleoside triphosphates
ddTTP	dideoxythymidine triphosphates
DNA	deoxyribonucleic acid
dNTP	deoxynucleoside triphosphates
ds-	double-stranded
EBL	electron beam lithography
EDL	electrical double layer
EDL	electrical double layer
EDTA	ethylenediaminetetraacetic acid
EM-CCD	electron multiplying charge coupled device

EOF	electro-osmotic flow
FEB	focused electron beam
FIB	focused ion beam
G	guanine
GFP	green fluorescent protein
HIM	helium ion microscope
IBS	ion beam sputtering system
ICR	ionic current rectification
JEOL	Japan electron optics laboratory
LMIS	liquid metal ion source
MB	megabytes
NA	numerical aperture
NGS	next Generation Sequencing
NHGRI	national human genome research institute
PVP	polyvinylpyrrolidone
RIE	reactive ion etching
RNA	ribonucleic acid
SBS	sequencing by synthesis
SEM	scanning electron microscope
SMRT	single molecule real time
ss-	single-stranded
STEM	scanning transmission electron microscopy
T	thymine

TBE	Tris (base) – Borate (acid) – EDTA (Ethylenediaminetetraacetic acid)
TEM	transmission electron microscopy
UNC	University of North Carolina (at Chapel Hill)
UV	ultraviolet

LIST OF SYMBOLS

a	diameter (width) of a polymer
A	cross sectional area
a_0, a_1	constants in equation 1.25
B	a constant in Odijk's equation (1.34)
c	concentration
D	diameter of the channel
$D(x)$	geometric mean of the nanofunnel width and depth at position x
D_m	geometric means of the nanofunnel width and depth at its widest point
D_n	geometric means of the nanofunnel width and depth at its narrowest point
e	electron charge
E	electric field
E_{min}	minimal electric field required to keep DNA in the nanofunnel
E_t	threshold field strength
f	frequency
F_{eh}	electrohydrodynamic force
F_{stall}	external force holding the molecule
i	the i th ion species
I_s	ionic strength
J_{back}	background flow with flux
J_m	total ionic current in the microchannel
J_n	total ionic current in the nanochannel

k_B	Boltzmann's constant
L	contour length of a polymer
l_B	Bjerrum length
$L_{de\ Gennes}$	contour length of a polymer in de Gennes' theory
L_{funnel}	length of the nanofunnel
L_{Odijk}	contour length of a polymer Odijk's theory
l_p	persistence length of a polymer
N	volumetric density
pH	negative logarithm of the activity of the (solvated) hydronium ion
q	charges
Q	total charge of a particle
q_{eff}	effective charge
R	polymer size (root-mean-square end-to-end distance)
R_g	radius of gyration
$R_{particle}$	hydrodynamic radius
T	temperature
U	electrostatic energy
v	velocity
w	effective width of a polymer
x	distance
z	valence
β_m	ratio of the cation and anion concentrations in the microchannel
β_n	ratio of the cation and anion concentrations in the nanochannel

ε_0	vacuum permittivity
ε_r	dielectric constant
ζ	zeta-potential
ζ^*	dimensionless zeta-potential ($ez\zeta/k_B T$)
η	viscosity
κ	inverse of the Debye length
λ_D	Debye length
μ	mobility
μ_{eo}	electroosmotic mobility
ζ	friction coefficient
ζ_H	interstrand distance of a polymer
ρ	volumetric charge density
σ	surface charge density
φ	electric potential
φ^*	dimensionless potential ($ez\varphi/k_B T$)
Γ	linear number charge density
Γ_0	density to a saturated value,.
$\Delta\mu$	difference in the EOF mobilities for the solutions with or without PVP
[+]	positive mobile ion concentration
[-]	negative mobile ion concentration

Chapter 1: DNA, Sequencing, and the Utility of Nanofluidic Devices

1.1 DNA

1.1.1 A Historical Perspective

The story of DNA's discovery by Swiss physician Johannes Friedrich Miescher in the winter of 1868/1869 is quite inspiring.¹ In the spring of 1868, after graduating from the medical school at the University of Basel in Switzerland, Miescher went to the University of Tübingen in Germany to receive his scientific training in chemistry and physiology. He was inspired to pursue an academic career in part by his father and uncle, who both were professors at the University of Basel. His decision not to practice as a physician was also influenced by a partial hearing impairment incurred during childhood.

In Tübingen, Miescher attempted to analyze the composition of cells in the ambitious hope of determining the chemical basis of life. At that time, the secretion of pus was considered beneficial to wound healing and was sometimes actively induced. Absorbent cotton was recently adopted as a preferred wound dressing for soaking up the ample amount of pus. One consequence of this confluence of technology and medical convention was that Miescher had access to a large quantity of bandages from the local hospital, from which he could wash relatively pure leukocytes.

To isolate the cellular components, Miescher allowed the cells to sediment and then lysed them using diluted hydrochloric acid (the laboratory centrifuge had not been invented yet). He then extracted the lipids and other hydrophobic molecules, and observed a fine powder suspended in the remaining solution. When acidified, this became a white, flocculent

precipitate that could be dissolved when an alkaline solution was titrated into the sample solution. This precipitated substance was positive to the xanthoprotein color reaction (which was actually due to protein contamination) but unlike protein, it did not coagulate when boiled. The elementary chemical analysis indicated that the precipitate contained an unexpected large quantity of phosphorus, in addition to carbon, hydrogen, oxygen, nitrogen, and some sulfur.² Miescher believed he had found a new molecule and called it “nuclein.”

In 1872, Miescher returned to the University of Basel as a professor. He continued his work again in winter because he believed that the cold temperature was critical for protecting the samples during the extraction and analysis protocols. He switched his nuclein source to sperm extracted from salmon he caught in the nearby Rhine River on the freezing cold winter nights. He also developed new protocols to obtain large quantities of the purest nuclein, from which he determined that this new substance must be a multi-basic acid.

However, neither Miescher nor his contemporary scientists realized the real importance of this discovery. Miescher initially thought that the nuclein was used by cells as a source of phosphorus. He then suspected that it was the causative agent of fertilization but that the chemical differences of the nuclein between different species were too small to be responsible for phenotypical diversity.

Interest in Miescher’s nuclein gradually diminished until the mid-twentieth century, when nuclein (since identified as deoxyribonucleic acid, or DNA) was finally proven to be the carrier of genetic information. In 1944, Avery et al. proved that in Griffith’s “transforming principle,” the substance that is capable of transforming an innocuous bacteria into a toxic one, is DNA.³ This finding was widely accepted in 1952, when Hershey and Chase confirmed it with experiments using viral DNA.⁴

In 1953, based on Wilkins and Franklin's X-ray diffraction pattern, Watson and Crick published a 900-word paper in *Nature*,⁵ proposing the double helix structure of DNA. The story of Watson and Crick's discovery is well known and this discovery was marked as the beginning of the era of molecular biology. The double helix has become one of the icons of the twentieth century.

1.1.2 DNA Sequencing Technologies

The DNA double helix consists of two anti-parallel strands comprised of alternating phosphate groups and sugar residues. Each sugar is also linked to one of the four nitrogenous bases: Adenine, Thymine, Guanine and Cytosine (A, T, G and C). The two strands are associated through complementary hydrogen bonds, with A bonding specifically to T and C to G. This arrangement is called base pairing and the entire sequence of the bases along the backbone, which encodes the information of all the living beings, is called the genome. The human genome contains over 3 billion base pairs (bp), which is equivalent to ~800 Megabytes (MB) of data – slightly greater than the capacity of an audio compact disk. Decoding this information from the DNA molecules is considered the key to better understanding evolution, individuals' predispositions to diseases and responses to therapies, and the characteristics (and vulnerabilities) of pathogens.⁶

1.1.2.1 Sanger Sequencing

In 1977 (about twenty years after receiving the Nobel Prize in Chemistry) Frederick Sanger published a paper⁷ describing a DNA sequencing method with chain-terminating inhibitors, which led to his second Nobel prize. This method was the basis of the giant Human Genome Project, launched in 1990, and remains the most accurate DNA sequencing technique available today.⁸ A DNA sample is divided into four reaction channels, each

containing DNA primers (short sequences that bind to complementary sequences of target DNA and enable polymerase-catalyzed DNA extension), polymerase, and a complement of natural deoxynucleoside triphosphates (dNTPs). Each reaction is supplied one of four dideoxynucleoside triphosphates (ddNTPs) - ddATP, ddTTP, ddCTP, or ddGTP - at low concentrations (relative to dNTPs). The DNA extension catalyzed by polymerase is terminated when a ddNTP is incorporated. This produces DNA molecules of various lengths, all terminated with the same known nucleotides for each channel. The labeled DNA fragments are then separated using gel electrophoresis, and the sequence of DNA read from fragment lengths observed in the four channels. This method works for DNA strands up to ~1000 bases, with the limitation due to the similarity of electrophoretic mobilities once macromolecules reach a certain size. To generate longer sequences, a shotgun sequencing technique is used.⁹ DNA is first randomly fragmented, each segment is sequenced, and then longer stretches of contiguous sequence (“contigs”) are computationally assembled from the fragments. Significant improvements in ddNTP chemistry (i.e., four-color, fluorescent labeling) and parallelization of electrophoresis in capillary arrays dramatically increased throughput and enabled the completion of the Human Genome Project in 2003, two years ahead of schedule.¹⁰ Despite the development of the lower cost sequencing technologies described below, the Sanger method remains the “gold standard” of DNA sequencing with an accuracy of 99.99%.

1.1.2.2 Next Generation Sequencing (NGS) Methods

Even with highly automated parallel runs, Sanger sequencing is too expensive and slow to generate massive amounts of sequence data. Many new sequencing technologies have emerged to lower the cost, stimulated by the National Human Genome Research

Institute's (NHGRI) \$1000 genome project.^{8,11,12} The most successful of these technologies are variations of sequencing by synthesis (SBS) in which the incorporation of nucleotides into an extending DNA strand is directly detected.¹³

The sequencing method developed by Illumina, Inc. images a massive array of DNA template colonies immobilized on a substrate.⁸ The DNA templates are first attached to a glass slide and amplified locally using a bridging method to form DNA clusters.¹⁴

Subsequent reactions are initiated using reagents supplied through a system of fluidic channels. The four types of fluorescently labeled reversible terminating bases are added to react with the DNA clusters. After the unreacted nucleotides are washed away, the type of nucleotide just incorporated can be read directly from a color image. The dye and the terminating groups are then cleaved and washed away and the cycles repeated to read the DNA sequence. The advantage of this method is that a very large number of DNA clusters can be read at the same time with a single camera. The throughput is determined by the size and density of the DNA cluster array and is much higher than that of Sanger sequencing. However, the read length is typically limited to ~100 bp due to dephasing, the accumulating loss of synchrony of nucleotide additions across copies of a template within a cluster. Error rates are typically two orders of magnitude higher than in Sanger sequencing (i.e., sequence accuracy is 99%).

Both the Sanger and Illumina sequencing methods require many copies of DNA to achieve detectable signals. Limited read lengths make the subsequent sequence assembly more difficult and prone to error. Additionally, the reaction and the detection steps are separated so the full potential of the catalytic speed of the polymerase is not exploited.¹⁵ Pacific Biosciences, however, recently developed a single molecule real time (SMRT®)

sequencing technology which greatly extends the read length.¹⁵ Rather than a flat substrate, the Pacific Biosciences system utilizes an optically transparent substrate coated with an aluminum film that is ~100 nm thick. Within this film are patterned an array of holes extending through the film to the underlying substrate and having diameters of 60-100 nm. Each of these holes acts as a reaction well and polymerase enzymes are covalently bound to the bottom of individual wells. Because these wells have diameters below the wavelength of visible light, they act as zero-mode waveguides, ensuring that the excitation of fluorescent molecules in solution is localized near the substrate surface (i.e., near the polymerase).¹⁶ Single ss-DNA templates are incorporated by the bound polymerase and then a solution of labeled nucleotides is introduced, beginning extension of the complementary strand. Each nucleotide is fluorescently labeled on the terminal phosphate group, meaning that the dye molecule diffuses away from the polymerase after incorporation, leaving a natural nucleotide suitable for continued strand extension. A successful incorporation is observed as a fluorescence pulse, with the nucleotides distinguished by the color of the fluorescent dye. The continuous reaction of the polymerase enables average read lengths of 3,000-5,000 bases with some reads exceeding 20,000 bases. The misincorporation of nucleotides and detection errors result in a single-read accuracy of <90%, though the random nature of the errors ensures that accuracy can be improved by additional coverage.¹⁷

Other sequencing methods are also being developed to achieve cheaper and faster sequencing such as 454 pyrosequencing,⁷³ Helicos single molecule sequencing,⁷⁴ Ion Torrent's SBS system,¹⁸ sequencing using transmission electron microscopy (TEM) imaging,¹⁹ sequencing with mass spectrometry,²⁰ nanopore sequencing,²¹ and nanochannel sequencing.²² More will be discussed about the latter two techniques in section 1.3 below.

1.1.3 Physical Properties of DNA

The above discussion of sequencing methods focuses primarily on the chemical nature of DNA. The physical properties of DNA also play an important role in the various sequencing technologies, whether it relates to electrophoretic separations in Sanger sequencing or template incorporation in SBS methods. It becomes of critical importance in proposed nanopore and nanochannel-based sequencing technologies. A great deal is known about DNA's physical properties because it is highly amenable to single-molecule characterizations for a variety of reasons.²³ DNA molecules can be found in circular or linear form. They are available in monodisperse size distributions with contour lengths ranging from nanometer to centimeters. It is possible to fluorescently stain them using high efficiency, intercalating dyes to enable single molecule observation.²⁴

Three key parameters are used to describe the physical properties of DNA: the contour length (L), the persistence length (l_p), and the effective width (w). The contour length is the end to end length of a fully extended DNA molecule. For double-stranded DNA (ds-DNA) this corresponds to the number of base pairs, N , times the base-pair to base-pair distance (0.34 nm).²⁵ In the double helix, the aromatic bases are positioned in the helix's interior while the hydrophilic, negatively charged phosphate-sugar backbone is exposed on the helix's exterior. The hydrogen bonding and base stacking makes ds-DNA quite stiff. This stiffness is quantified using a parameter called the persistence length in polymer physics. In principle, the persistence length depends on the sequence of the DNA, as G-C pairs have three hydrogen bond, while A-T pairs only have two. However, this dependence is relatively small compared to the effect of the charge on the backbone.²⁶ Coulombic interactions make the chain stiffer, an effect that depends on the ionic strength of the solution. The persistence

length decreases as the salt concentration increases, until it reaches a saturation point, which can be explained by the Manning condensation theory.²⁷ In general, the persistence length (in nm) is given by the equation²⁸

$$l_p \approx 46.1 + 6.3\lambda_D \quad (1.1)$$

where λ_D is the Debye length (in nm). More will be discussed about the Debye length and Manning condensation in section 1.2. Note that the intercalating dye used in our fluorescence experiments increases the contour length and may affect the persistence length as well.²⁹

The charge on the back bone also contributes significantly to DNA's effective width, which can be described by

$$w = \lambda_D \left[0.7704 + \log \left(\frac{\lambda_D e^2 \Gamma^2}{2\epsilon_0 \epsilon_r k_B T} \right) \right] \quad (1.2)$$

where Γ is the number charge density (m^{-1}), e is the electron charge, ϵ_0 is the vacuum permittivity, ϵ_r is the fluid dielectric constant, k_B is Boltzmann's constant, and T is the temperature.³⁰ The physical width of B-form ds-DNA, as determined from the crystal structure, is ~ 2 nm. The effective width, however, is about 5 nm in a 100 mM monovalent salt solution and about 20 nm in a 5 mM solution.²⁶

Assuming the polymer behaves as an ideal random coil, the polymer's contour can be treated as a random walk of Kuhn monomers with a step length of $2l_p$. The scaling of the polymer size (root-mean-square end-to-end distance, R) is²³

$$R \sim (l_p L)^{1/2} \quad (1.3)$$

In reality, a polymer chain occupies an "excluded volume," which depends on the hard-core repulsion and the extent of solvation of the monomers. Flory theory takes into account this "self-avoidance" and the corrected root-mean-square end-to-end distance is³¹

$$R_F \sim (wl_p)^{1/5} L^{3/5} \quad (1.4)$$

While ds-DNA behaves as a model polyelectrolyte under a variety of experimental conditions, single-stranded DNA (ss-DNA) has the bases exposed to solution and given their hydrophobic character, the molecules tend to form secondary structures. To minimize these structures, many experiments on ss-DNA are performed using denaturing buffers at elevated temperature, giving a persistence length of 1-5 nm.²³ This presents a considerable challenge in using ss-DNA to probe the effects of confinement in nanoscale structures, as will become apparent in future chapters. The experiments described in this thesis and the corresponding discussion all pertain to ds-DNA.

1.2 Basic Electrokinetics

Nanofluidics is the study of fluids in structures with one or more dimensions below 100 nm.³² Because the hydraulic resistances are very high in nanofluidic conduits, fluidic transport is primarily manipulated using electrokinetic techniques.³² As a result of the reduced dimensions and increased surface-to-volume ratio, electrokinetic phenomena that are not significant in micron scale channels become important in nanoscale channels.³² It is thus very important to have a basic understanding of electrokinetic phenomena in order to understand behavior in nanofluidic systems.

1.2.1 Electrostatics

Many concepts in electrostatics involves the interplay between the Coulomb energy and the thermal energy, which determines the charge distribution.³³ The charge distribution near a point charge, a linear polymer, and a charged surface will be discussed, followed by the important concepts of the electrical double layer (EDL) and the zeta potential.

1.2.1.1 Ion Pairs and the Bjerrum Length

In an ideal electrolyte solution, the interactions between ions are ignored. This is not realistic, however, particularly in high ionic strength solutions where the interaction between ions can be strong enough that two oppositely charged ions can associate as an ion pair.³⁴

The electrostatic energy, U , of two point charges is described by Coulomb's law,

$$U = \frac{q_1 q_2}{4\pi\epsilon_0\epsilon_r} \times \frac{1}{x} \quad (1.5)$$

where q_1 and q_2 are the charges of points 1 and 2, respectively, and x is the distance between charges. When this energy for two elementary charges is comparable to the thermal energy, $k_B T$, a characteristic length scale known as the Bjerrum length, l_B , (after chemist Niels Bjerrum) is described:³⁴

$$l_B = \frac{e^2}{4\pi\epsilon_0\epsilon_r k_B T} \quad (1.6)$$

In aqueous solutions at room temperature,

$$l_B \approx 0.7 \text{ nm} \quad (1.7)$$

1.2.1.2 Charge Distribution near a Polyion

While the electric potential near a small ion increases inversely with decreasing distance (Equation 1.5), it is a logarithmic function of x upon approach to a line charge:³⁵

$$U = \frac{e^2 \Gamma}{4\pi\epsilon_0\epsilon_r} \times -\ln(x) \quad (1.8)$$

The charge distribution near a linear charged polymer can be treated by Manning's condensation theory, assuming an infinitely long line charge with linear density, Γ .²⁷ When Γ is sufficiently high, counterions can condense onto the polymer, reducing the density to a saturated value, Γ_0 .²⁷ This saturated linear density can be estimated by balancing the

electrostatic energy between the linear charge and counterion point charges (Equation 1.8) and the entropy of the counterions:³⁵

$$k_B T \times \ln(x) \quad (1.9)$$

which, together with Equation 1.6, yields the relationship

$$\Gamma_0 = \frac{1}{l_B} \quad (1.10)$$

Considering the 0.7 nm value of the Bjerrum length given above (Equation 1.7), Γ_0 is calculated to be 1.4 nm^{-1} or $0.49 e^-$ per base pair, indicating a significant decrease from the nominal value for ds-DNA of $2 e^-$ per base pair.

1.2.1.3 Charge Distribution near a Surface

The electric potential experienced by a point charge approaching a charged surface increases linearly as a function of x .³⁵ The charge distribution near a surface can be described by the Gouy-Chapman theory,³⁶ and a simplified derivation to the main conclusions is presented below.³⁷

When the solution is in equilibrium, the electrochemical potential of ion i must be the same everywhere. In balancing the gradient of the electric energy and the entropic energy, the ions exhibit a Boltzmann distribution:³⁸

$$n_i = n_{i,bulk} \exp\left(\frac{-z_i e \phi}{k_B T}\right) \quad (1.11)$$

where n_i is volumetric ion density, $n_{i,bulk}$ is the volumetric ion density in the bulk, z_i is the charge of ion i , and ϕ the electric potential. The volumetric charge density of all ions near the surface is:

$$\rho = e \sum_i n_i z_i \quad (1.12)$$

The net charge density at distance x from the surface follows the Poisson equation:

$$\nabla^2 \varphi = \frac{d^2 \varphi}{dx^2} = -\frac{\rho}{\epsilon_0 \epsilon_r} \quad (1.13)$$

Combining Equations 1.11 –1.13 leads to the Poisson-Boltzmann equation:

$$\frac{d^2 \varphi_i}{dx^2} = -\frac{e}{\epsilon_0 \epsilon_r} \sum_i n_{i,bulk} z_i \exp \left[-\frac{z_i e \varphi_i(x)}{k_B T} \right] \quad (1.14)$$

For small surface potentials, $\frac{z_i e \varphi_i(x)}{k_B T} \ll 1$, the Debye-Hückel approximation can be applied

and Equation 1.14 becomes (using $\exp(-\alpha) = 1 - \alpha$ for small α):

$$\frac{d^2 \varphi}{dx^2} = \kappa^2 \varphi(x) \quad (1.15)$$

where

$$\kappa = \left(\frac{e^2 \sum_i n_{i,bulk} z_i^2}{\epsilon_0 \epsilon_r k_B T} \right)^{\frac{1}{2}} \quad (1.16)$$

The inverse of κ is also known as the Debye length (λ_D), which describes the characteristic length over which surface charges are screened by counterions in solution. At 25 °C, Equation 1.16 can be simplified to give λ_D (in nm),³⁷

$$\lambda_D = \frac{9.61}{\sqrt{I_s}} \quad (1.17)$$

where the ionic strength, I_s , expressed in mM is given by

$$I_s = \frac{1}{2} \sum_i c_i z_i^2 \quad (1.18)$$

where c_i is the concentration of the i th ion and z_i its charge. For 1 mM KCl, $\lambda_D \approx 10$ nm, for 100 mM KCl, $\lambda_D \approx 1$ nm.

Equation 1.15 is appropriate for small surface potentials ($z_i \varphi_i \ll 25.7$ mV). Assuming a flat surface and symmetric electrolyte, a more general solution of Equation 1.14 is known as the Gouy-Chapman equation:

$$\frac{d^2\varphi}{dx^2} = \frac{2ez}{\varepsilon_0\varepsilon_r} n_{bulk} \sinh(ez\varphi/k_B T) \quad (1.19)$$

1.2.1.4 The Electric Double Layer and the Zeta Potential

The Gouy-Chapman model treats ions in solution as point charges and the solvent as a structureless dielectric with constant permittivity. To describe the system in finer detail, Stern introduced the idea of a compact layer of immobile surface ions and solvent molecules, later referred to as the Stern layer.³⁷ Outside this compact layer exists a diffuse layer of mobile ions and solvent molecules, which can be described by the Gouy-Chapman model. The shear surface separating the immobile ions and the mobile ions is called the slip plane and the potential difference between this boundary and the bulk solution is the zeta-potential, ζ . Using this boundary condition, Equation 1.15 can be solved:³⁹

$$\varphi(x) = \zeta \exp(-\kappa x) \quad (1.20)$$

and Equation 1.19 is solved:³⁹

$$\varphi^* = 2 \ln \left(\frac{1 + \exp(-\kappa x) \tanh(0.25\zeta^*)}{1 - \exp(-\kappa x) \tanh(0.25\zeta^*)} \right) \quad (1.21)$$

where $\varphi^* = ez\varphi/k_B T$ and $\zeta^* = ez\zeta/k_B T$.

Even for a fixed surface charge density, the zeta potential will change as a function of ionic strength. For a surface with fixed charge density σ , assuming the total charge in the diffuse layer has the same magnitude but opposite sign compared to the total charge on the surface,

$$\sigma = - \int_0^\infty \rho dx = - \varepsilon_0 \varepsilon_r \left. \frac{d\varphi}{dx} \right|_{wall} \quad (1.22)$$

where the right hand side of the equation is from the Poisson equation (1.13). Substituting Equation 1.20 into Equation 1.22 gives:⁴⁰

$$\zeta = \frac{\lambda_D \sigma}{\varepsilon_0 \varepsilon_r} \quad (1.23)$$

More generally, substituting Equation 1.21 into Equation 1.22 gives:⁴⁰

$$\sinh\left(\frac{-e\zeta}{2k_B T}\right) = \frac{\lambda_D \sigma e}{2\varepsilon_0 \varepsilon_r k_B T} \quad (1.24)$$

At 25 °C, $2k_B T/e = 51.2$ mV. When $\zeta \ll 2k_B T/e$, using $\sinh x \approx x$, Equation 1.24 is reduced to Equation 1.23. When $\zeta \gg 2k_B T/e$, using $\sinh x \approx \exp(x)/2$, Equation 1.24 becomes

$$\zeta = -\frac{2k_B T}{e} \ln(\lambda_D) - \frac{2k_B T}{e} \ln\left(\frac{\sigma e}{\varepsilon_0 \varepsilon_r k_B T}\right) = a_0 \ln(\lambda_D) + a_1 \quad (1.25)$$

Equations 1.23 and 1.24 are used to calculate the zeta potential under different conditions. The simpler Equation 1.23 generally works for silica at low pH or high ionic strength. At higher pH or low ionic strength, however, Equation 1.25 should be used.

1.2.2 Electrophoresis and Electroosmosis

When subjected to an electric field, the motion of a fluid due to the force on the diffuse charges is described by the Navier-Stokes equation:⁴⁰

$$\rho E + \eta \nabla^2 v = 0 \quad (1.26)$$

where v is the fluid velocity, η is the viscosity, and E is the electric field.

Combining with Poisson's equation (1.13), the velocity can be solved by applying the boundary conditions at the surface (non-slip) and far away in the bulk :⁴⁰

$$u = -\frac{\varepsilon_0 \varepsilon_r \zeta}{\eta} E \left(1 - \frac{\varphi}{\zeta}\right) \quad (1.27)$$

Equations 1.20 and 1.21 can be substituted into Equation 1.27 to calculate the velocity profile. Since $\varphi = 0$ far from the surface,

$$u = -\frac{\varepsilon_0 \varepsilon_r \zeta}{\eta} E = \mu_{eo} E \quad (1.28)$$

where the term μ_{eo} is known as the electroosmotic mobility, which was first described by Smoluchowski.³⁷

When a charged particle in an electrolyte solution is influenced by an electric field, the particle will move in one direction while the counterions will migrate in the opposite direction. Two simple solutions describing this motion can be obtained. In the case of a thick double layer, the drag force and the electric force described by Stokes' law and Coulomb's law, respectively, can be balanced:

$$\frac{u_{particle}}{6\pi\eta R_{particle}} = QE \quad (1.29)$$

where $u_{particle}$ is the electrophoretic velocity of the particle, $R_{particle}$ is its hydrodynamic radius and Q is the charge of the particle. For a thin double layer, the fluid flow around the particle as it migrates through the electrolyte resembles electroosmotic flow and:

$$u_{particle} = \frac{\varepsilon_0 \varepsilon_r \zeta}{\eta} E \quad (1.30)$$

Here, the velocity is independent of the particle size and shape. This equation describes the relative motion of the particle and the counterions, with the bulk fluid assumed to be at rest and the shear forces restricted to the Debye layer. This has profound implications for DNA free electrophoresis. In the thin double layer limit, the electric force and the drag are balanced for each segment of the DNA and the fluid outside the Debye length is considered at rest. The mobilities of DNA molecules are therefore independent of DNA size, and the solvent is effectively transparent to the DNA molecules (i.e., the DNA molecules are free draining).⁴¹ The electrophoretic separation of DNA molecules of various sizes requires migration through a gel or sieving medium in which a reptation motion enables

separation.^{42,43} The local force picture of the DNA free electrophoresis is widely accepted, but extension of its use requires caution, especially when additional external forces are applied.²³

1.3 DNA Analysis Using Nanopores and Nanochannels

1.3.1 Nanopores

The idea of using pores to sense analytes can be traced back to the 1940's, when Wallace Coulter patented his invention for counting cells using an orifice.⁴⁴ Cells in an electrolyte are passed through the orifice using pressure driven flow, while a voltage is simultaneously applied to monitor the ionic current through the orifice. Because the conductance of a cell and the saline solution are different, a resistance pulse is detected when a cell passes through the orifice. From the frequency and the amplitude of the pulses, information about the cell concentration and size are obtained. The basic principle of nanopore-based sensing technologies is the same, except that the pore sizes are a few nanometers and the analytes are single biomolecules.

This leap was taken by Kasianowicz et al. in 1996,⁴⁵ when they detected the translocation of ss-DNA and RNA through a 1.5-nm protein pore, which is large enough for ss-DNA but not for ds-DNA (Figure 1.1).⁴⁶ In their experiments, an α -hemolysin protein pore complex was inserted into a lipid bilayer that was supported within a several micron Teflon orifice. ss-DNA or RNA molecules were added to one side of the pore, and a voltage was applied across it to electrophoretically drive the charged molecules. Stochastic current blockades were detected, each indicating interaction of a single molecule with the pore. Because the pore was only slightly larger than the width of the molecule, the molecules were forced to pass through the pore in a linear fashion. The amplitudes of the current blockades

should therefore be comparable for all events and their durations proportional to the length of the molecules. However, as shown in Figure 1.1 c, there were three distinctive groups in the histogram of event durations, despite a monodisperse RNA sample. The authors attributed the fastest events (peak 1 in the histogram) to collisions of RNA molecules with the nanopore, while the longer events (peaks 2 and 3) were due to successful translocations in which the molecules entered the pore with different orientations.

This hypothesis was confirmed by Math éet al. in 2005 using designed DNA hairpins with either 3' or 5' oriented ss-DNA overhangs.⁴⁷ After the ss-DNA overhang was threaded into the α -hemolysin nanopore, the duplex region of the molecule prevented DNA passage through the pore. When the voltage was switched off, the time required for the molecule to diffuse out of the pore was detected and found to depend strongly on its orientation. All-atom molecular dynamics showed that the bases of the ss-DNA are tilted, resulting in a difference in the effective friction for the two orientations.⁴⁷

When a molecule is in the α -hemolysin pore, the electric force applied can be easily tuned by adjusting the voltage. The hairpin which usually stops the DNA translation thus can be unzipped given a high enough voltage. Sauer-Budge et al. constructed two molecules of DNA, both having a 50 base pair duplex region and a 50 base ss-DNA overhang. These two samples differed, however, in that one exhibited perfect complementarity in the duplex region while the other contained a four consecutive base-pair mismatches. The authors found that the time required to unzip the duplex was shorter for the molecule containing the mismatched bases (Figure 1.2 a).⁴⁸ Using a linear voltage ramp (Figure 1.2 b), Math éet al. measured the critical voltage for the unzipping of various hairpins in an α -hemolysin nanopore and found that the kinetics depended not only on the hairpin length but also on the

ramp rate and temperature.⁴⁹ A similar unzipping experiment was conducted by McNally et al. using a 2 nm solid-state nanopore.⁵⁰

While biological nanopores provide highly reproducible pore structures, the size of a given pore cannot be easily tuned.⁵¹ Pores fabricated in solid-state membranes, on the other hand, offer the possibility of greater geometric and compositional variety.⁵² Using a 3-nm pore fabricated in a silicon nitride membrane, Li et al. were the first to demonstrate the detection of DNA translocations (of ds-DNA) through an artificial nanopore.⁵³ In this initial experiment and in subsequent studies it was found that DNA molecules can pass through these larger nanopores (relative to α -hemolysin) in a folded conformation, resulting in current blockades having twice the amplitude and half the duration of events observed for fully linearized molecules (Figure 1.3). This effect is also seen in nanopores fabricated in single layer graphene sheets, a material that has attracted interest for nanopore applications due to its thinness.^{54,55}

From these experiments, it is clear that the differences in molecular width can result in different responses in the current attenuation. One potential application is the mapping of DNA by hybridization or association of sequence specific tags, followed by the nanopore-based detection of these probe locations along a DNA molecule.²¹ Several proof-of-principle experiments have been demonstrated using this strategy.⁵⁶ One potential challenge with this approach is that the velocity of DNA translocation through a nanopore is not constant throughout the process.⁵⁷

Since the first demonstrations by Kasianowicz et al., a motivation behind nanopore-based sensing was to enable the direct, single-molecule sequencing of nucleic acids by distinguishing bases based on the current blockade levels.²¹ To test this hypothesis, early

experiments by Akeson et al. studied the current signals from different homopolymers including poly A and poly C.⁵⁸ The current blockades are indeed distinguishable, with Poly C showing larger amplitude blockades, but this difference in response is due to the different secondary structures of the two homopolymers.

In 2009 Clarke et al. reported that a cyclodextrin adapter could be inserted into the interior of an α -hemolysin pore.⁵⁹ This complex is sensitive enough to distinguish the four nucleoside monophosphates (Figure 1.4). The authors then conducted the experiment with a sample of ss-DNA and exonuclease in the solution. The nucleoside monophosphates released by the exonuclease were subsequently identified by the modified pore.⁵⁹ A sequencing method was proposed in which an exonuclease would be attached near the pore entrance such that nucleoside monophosphates excised from a DNA molecule would migrate through the pore complex and be identified.

An alternative strategy, using a polymerase enzyme to assist nanopore-based sequencing, has also been proposed and demonstrated.^{60,61} The target ss-DNA is hybridized to a primer strand and a “blocking oligomer” and then bound to a polymerase (Figure 1.5). Native nucleoside triphosphates and enzyme cofactors are also added to the solution and the blocking oligomer prevents the premature extension of the complementary strand. The single-stranded portion of the template DNA is pulled into the nanopore (α -hemolysin or MspA). The force on the DNA/polymerase complex induces the unzipping and removal of the blocking oligomer. The polymerase then starts extending the complementary strand, ratcheting the single-stranded portion of the template DNA through the nanopore, counter to the electric field. The procession of DNA through the pore is thus significantly slower than in the case of free migration and the characteristic signal of nucleotides can be resolved.

1.3.2 Nanochannels

There are two significant differences between DNA behavior and analysis in nanopores and nanochannels. First, nanochannels are by definition longer than nanopores and they consequently confine a macromolecule along a considerable portion of its length. In many applications, it is desirable to introduce DNA molecules into channels that are longer than the DNA's contour length.^{26,62} This is in contrast to nanopores in thin membranes (<100 nm thick), where a relatively small segment of a DNA molecule is directly constrained. Second, an optical signal (instead of electric signal) is often used as the detection method in nanochannel experiments. The length of nanochannels can render them relatively insensitive to DNA induced perturbations in the axial ionic conductance. At the same time, the co-planar integration of nanochannels with ancillary device components discussed in Chapter 2 is conducive to optical microscopy. Due to these differences, single molecule analyses in nanochannels are quite different than those conducted using nanopores.

A natural application of nanochannels is to study the extension of confined DNA. This extension increases as the size of the channel decreases.³¹ Two confinement regimes, defined by different molecular conformations are observed, requiring distinct theories (Figure 1.6).²⁶ When the size of the channel is much larger than the persistence length, l_p , the de Gennes blob theory is appropriate.⁶³ For this theory, the polymer conformation is treated as a series of blobs, each following the unconfined self-avoiding random walk configuration (Figure 1.6 a). The blob size is constrained to the diameter of the channel, D . From Equation 1.4, the contour length of each blob is:

$$L_{de\ Gennes} \sim \frac{D^3}{(l_p w)^{1/3}} \quad (1.31)$$

So the extension length of the entire confined polymer simply is

$$R_{de\ Gennes} \sim \frac{L}{L_{de\ Gennes}} D \sim L \frac{(wl_p)^{1/3}}{D^{2/3}} \quad (1.32)$$

When the nanochannel diameter is much less than the persistence length, however, the energy cost for bending increases rapidly, so the polymer assumes a deflecting rod conformation, as modeled by Odijk (Figure 1.6 b).⁶⁴ The contour length of each Odijk segment is,

$$L_{Odijk} = (l_p D^2)^{1/3} \quad (1.33)$$

and the overall extension length of the confined polymer is:

$$R_{Odijk} = L \left[1 - B \left(\frac{D}{l_p} \right)^{2/3} \right] \quad (1.34)$$

B is a constant depending on channel cross-section geometry, which is 0.17 for circular channels and 0.18 for square channels.⁶⁵

Several studies have investigated the scaling of chain size as a function of the channel diameter experimentally or through simulations. The compiled experimental results are compared to simulation results by Wang et al. in Figure 1.7.⁶⁶ Most of the experimental results in Figure 1.7 were generated by Reisner et al. in experiments conducted in rectilinear nanochannels in fused-silica using λ -phage DNA.⁶² The Odijk regime is underrepresented in this data set, given the challenges of nanochannel fabrication at these smaller dimensions. For the larger channels (>50 nm), the experimental results qualitatively compare favorably with the simulation results, showing a power law dependence. The exponent of a the power law fit, however, was found to be -0.85 instead of the -2/3 predicted by de Gennes.⁶² Similar results were obtained by Persson et al. in a fused silica nanofunnel device, which had a fixed depth of 60 nm but a varying width ranging from 100 nm to 1000 nm over a distance of 450

microns.⁶⁷ Because of the changing aspect ratio of the channel, a geometric average is used to characterize the mean channel diameter. An exponent of -0.85 is found to agree with Reisner's results. Interestingly, when the extension length of circular DNA is measured in the same device, the power law relationship between extension length and channel diameter has an exponent of -0.65, close to de Gennes' theory. Wang et al. performed simulations showing that there are two transitional regimes between the Odijk and de Gennes confinement models. The fact that the data obtained from the previous experiments were fit over a wide range of nanochannel sizes might contribute to the disagreement between the experimental data and the theoretical prediction. Utko et al. performed an experiment in thermoplastic channels having geometric means ranging from 200 to 300 nm and obtained an exponent of -0.76, closer to the predicted value of -2/3.⁶⁸

In order to introduce DNA molecules into a nanochannel, a force is needed to overcome the entropic barrier.⁶⁹ The reverse process (ejection of a DNA molecule from a nanochannel) is initiated once a portion of the molecule escapes the nanochannel. Intensity profiles of DNA molecules in Figure 1.8 show several processes during which the conformational entropy of a DNA molecule changes.⁷⁰ The molecule was first electrophoretically driven into the nanochannel. The opposing electric and entropic forces stretch the molecule, such that when it is fully contained in the channel and the voltage is turned off, the molecule relaxes to its equilibrium extension length. This process occurs over 50 s. After 77 s, the molecule is electrophoretically migrated back to the entrance of the channel and begins to recoil once one end exits the nanochannel. The entropic force in this process is estimated to be about 220 fN. At 115 s, the molecule is driven into the channel again. This time the voltage is turned off before the molecule is completely threaded into the

channel. The molecule starts to recoil while shrinking, and a different intensity trace profile is observed. In this case, the elastic recoil from a stretched conformation contributes to the primarily entropically driven escape from the nanochannel.

The dynamics of nanostructure driven changes in entropy can be used to affect separations of macromolecules based on their size. Figure 1.9 shows a nanofluidic device that was used for DNA separations.⁷¹ The device consists of an array of periodic deep and shallow nanoslits, which resulted in mobility differences between DNA molecules with different sizes. Larger molecules were found to migrate faster in these devices, and a theory was presented to explain this result.⁷² When the molecule passes through the shallow regions of the nanoslits, the entropic barrier is indifferent to the sizes. Larger molecules, however, have a larger probability to have several monomers placed close enough to the region, where the electric field is large enough to initiate translocation. The device is able to efficiently separate long molecules, and the use of a multi-channel device to run samples in parallel was also demonstrated, showing the potential for practical applications.⁷¹

Like nanopores, nanochannel-based devices also have potential utility for DNA genomic analysis, though the approaches are quite different. Several methods were proposed,²⁶ but the nick-labeling method of genomic mapping is discussed here.²² In this approach, specific sequences occurring in a strand of DNA are fluorescently labeled with one color. This is accomplished by cutting one strand of the ds-DNA using a nicking restriction enzyme. A short segment of DNA containing fluorescently labeled nucleotides is then extended from the nick site using polymerase. The entire molecule is also nonspecifically labeled with a different color. The molecules are then driven into a nanochannel array, resulting in molecules that are uniformly stretched. The molecules are imaged and the

locations of the target sequence are identified (Figure 1.10 a). The use of a high density array enables the imaging of multiple copies of genomic DNA, providing a more accurate consensus result. After the images were taken from each individual DNA segment, consensus maps with overlapping patterns were constructed (Figure 1.10 b).

1.4 Research Objectives

The first challenge in developing nanopore or nanochannel-based applications is to fabricate these features and integrate them within microfluidic devices. The development of various fabrication techniques is first discussed in Chapter 2. In order to introduce macromolecules into the nanostructures, a significant energy barrier must be overcome. Chapter 3 discusses how a nanofunnel can facilitate this process. Chapter 4 describes the statics and dynamics of a molecule trapped in one of the funnels introduced in Chapter 3. Finally, while much of the research described in this Thesis is focused on the application of nanofluidics to DNA and biomolecule analysis, fluid transport behavior in the nanochannels relevant to a variety of applications was also observed. This nanofluidic behavior (specifically, concentration polarization) is discussed in Chapter 5.

1.5 REFERENCES

1. Dahm, R. Discovering DNA: Friedrich Miescher and the early years of nucleic acid research. *Hum. Genet.* **122**, 565 (2008).
2. Wolf, G. Friedrich Miescher, the man who discovered DNA. **2**, http://www.bizgraphic.ch/miescheriana/html/the_man (2003).
3. Avery, O. T., MacLeod, C. M. & McCarty, M. Studies on the Chemical Nature of the Substance Inducing Transformation of Pneumococcal Types: Induction of Transformation by a Desoxyribonucleic Acid Fraction Isolated from Pneumococcus Type III. *J. Exp. Med.* **79**, 137 (1944).
4. Hershey, A. & Chase, M. Independent functions of viral protein and nucleic acid in growth of bacteriophage. *J. Gen. Physiol.* **36**, 39 (1952).
5. Watson, J. D. & Crick, F. H. C. A structure for deoxyribose nucleic acid. *Nature* **171**, 737 (1953).
6. Venter, J. C. *et al.* The sequence of the human genome. *Science* **291**, 1304 (2001).
7. Sanger, F., Nicklen, S. & Coulson, A. R. DNA sequencing with chain-terminating inhibitors. *Proc. Natl. Acad. Sci. USA* **24**, 5463 (1977).
8. Metzker, M. L. Sequencing technologies — the next generation. *Nat. Rev. Genet.* **11**, 31 (2010).
9. Staden, R. A strategy of DNA sequencing employing computer programs. *Nucleic Acids. Res.* **6**, 2601 (1979).
10. Noble, I. Human genome finally complete. *BBC news* <http://news.bbc.co.uk/2/hi/science/nature/2940601>. (2003).
11. Service, R. F. The race for the \$1000 genome. *Science* **311**, 1544 (2006).
12. Mardis, E. R. Next-generation DNA sequencing methods. *Annu. Rev. Genom. Hum. G.* **9**, 387 (2008).
13. Fuller, C. W. *et al.* The challenges of sequencing by synthesis. *Nat. Nanotechnol.* **27**, 1013 (2009).
14. Bentley, D. R. *et al.* Accurate whole human genome sequencing using reversible terminator chemistry. *Nature* **456**, 53 (2008).

15. Eid, J. *et al.* Real-time DNA sequencing from single polymerase molecules. *Science* **323**, 133 (2009).
16. Foquet, M. *et al.* Improved fabrication of zero-mode waveguides for single-molecule detection. *J. Appl. Phys.* **103**, 034301 (2008).
17. Liu, L. *et al.* Comparison of next-generation sequencing systems. *J. Biomed. Biotechnol.* **2012**, 251364 (2012).
18. Pennisi, E. Semiconductors inspire new sequencing technologies. *Science* **327**, 1190 (2010).
19. Bell, D. C. *et al.* DNA base identification by electron microscopy. *Microsc. Microanal.* **18**, 1049 (2012).
20. Edwards, J. R., Ruparel, H. & Ju, J. Mass-spectrometry DNA sequencing. *Mutat. Res.* **573**, 3 (2005).
21. Branton, D. *et al.* The potential and challenges of nanopore sequencing. *Nat. Biotechnol.* **26**, 1146 (2008).
22. Lam, E. T. *et al.* Genome mapping on nanochannel arrays for structural variation analysis and sequence assembly. *Nat. Nanotechnol.* **30**, 771 (2012).
23. Viovy, J.-L. Electrophoresis of DNA and other polyelectrolytes : Physical mechanisms. *Rev. Mod. Phys.* **72**, 813 (2000).
24. Glazer, A. N. & Rye, H. S. Stable dye-DNA intercalation complexes as reagents for high-sensitivity fluorescence detection. *Nature* **359**, 859 (1992).
25. Bates, A. D. & Maxwell, A. *DNA Topology*. (OXFORD university press, 2005).
26. Reisner, W., Pedersen, J. N. & Austin, R. H. DNA confinement in nanochannels: physics and biological applications. *Rep. Prog. Phys.* **75**, 106601 (2012).
27. Manning, G. S. Limiting Laws and Counterion Condensation in Polyelectrolyte Solutions I. Colligative Properties. *J. Chem. Phys.* **51**, 924 (1969).
28. Dobrynin, A. Effect of counterion condensation on rigidity of semiflexible polyelectrolytes. *Macromolecules* **39**, 9519 (2006).
29. Murade, C. U., Subramaniam, V., Otto, C. & Bennink, M. L. Force spectroscopy and fluorescence microscopy of dsDNA-YOYO-1 complexes: implications for the structure of dsDNA in the overstretching region. *Nucleic. Acids. Res.* **38**, 3423 (2010).

30. Stigter, D. Interactions of highly charged colloidal cylinders with applications to double-stranded DNA. *Biopolymers* **16**, 1435 (1977).
31. Rubinstein, M. & Colby, R. H. *Polymer Physics*. (OXFORD university press, 2003).
32. Sparreboom, W., van den Berg, A. & Eijkel, J. C. T. Principles and applications of nanofluidic transport. *Nat. Nanotechnol.* **4**, 713 (2009).
33. Dobrynin, a & Rubinstein, M. Theory of polyelectrolytes in solutions and at surfaces. *Prog. Polym. Sci.* **30**, 1049 (2005).
34. Wright, M. R. *An Introduction to Aqueous Electrolyte Solutions*. (John Wiley & Sons Ltd, 2007).
35. Rubinstein, M. Lecture notes of Polymer Physics. (2010).
36. Hunter, R. J. *Foundations of Colloid Science*. (OXFORD university press, 1987).
37. Schoch, R., Han, J. & Renaud, P. Transport phenomena in nanofluidics. *Rev. Mod. Phys.* **80**, 839 (2008).
38. Israelachvili, J. *Intermolecular and Surface Forces*. (Elsevier Ltd, 1991).
39. Russel, W. B., Saville, D. A. & Schowalter, W. R. *Colloidal Dispersions*. (Cambridge University Press, 1989).
40. Kirby, B. J. & Hasselbrink, E. F. Zeta potential of microfluidic substrates: 1. Theory, experimental techniques, and effects on separations. *Electrophoresis* **25**, 187 (2004).
41. Slater, G. W., Hubert, S. J., Boileau, J. & Pøpin, M. P. Review Theory of DNA electrophoresis : A look at some current challenges Nucleic acids. *Electrophoresis* (2000).
42. Lerman, L. S. & Frisch, H. L. Why does the electrophoretic mobility of DNA in gels vary with the length of the molecule? *Biopolymers* **21**, 995 (1982).
43. Lumpkin, O. J. & Zimm, B. H. Mobility of DNA in gel electrophoresis. *Biopolymers* **21**, 2315 (1982).
44. Coulter, W. H. US Patent #2,656,508. (2005).
45. Kasianowicz, J. J., Brandin, E., Branton, D. & Deamer, D. W. Characterization of individual polynucleotide molecules using a membrane channel. *Proc. Natl. Acad. Sci. USA* **93**, 13770 (1996).

46. Song, L. *et al.* Structure of staphylococcal alpha-hemolysin, a heptameric transmembrane pore. *Science* **274**, 1859 (1996).
47. Math   J., Aksimentiev, A., Nelson, D. R., Schulten, K. & Meller, A. Orientation discrimination of single-stranded DNA inside the alpha-hemolysin membrane channel. *Proc. Natl. Acad. Sci. USA* **102**, 12377 (2005).
48. Sauer-Budge, A., Nyamwanda, J., Lubensky, D. & Branton, D. Unzipping Kinetics of Double-Stranded DNA in a Nanopore. *Phys. Rev. Lett.* **90**, 1 (2003).
49. Math   J., Arinstein, A., Rabin, Y. & Meller, A. Equilibrium and irreversible unzipping of DNA in a nanopore. *Europhys. Lett.* **73**, 128 (2006).
50. McNally, B., Wanunu, M. & Meller, A. Electromechanical unzipping of individual DNA molecules using synthetic sub-2 nm pores. *Nano Lett.* **8**, 3418 (2008).
51. Healy, K. Nanopore-based single-molecule DNA analysis. *NANOMEDICINE-UK* **2**, 459 (2007).
52. Healy, K., Schiedt, B. & Morrison, A. P. Solid-state nanopore technologies for nanopore-based DNA analysis. *NANOMEDICINE-UK* **2**, 875 (2007).
53. Li, J., Gershow, M., Stein, D. M., Brandin, E. & Golovchenko, J. a. DNA molecules and configurations in a solid-state nanopore microscope. *Nat. Mater.* **2**, 611 (2003).
54. Garaj, S. *et al.* Graphene as a subnanometre trans-electrode membrane. *Nature* **467**, 190–193 (2010).
55. Geim, a K. & Novoselov, K. S. The rise of graphene. *Nat. Mater.* **6**, 183 (2007).
56. Singer, A. *et al.* Nanopore based sequence specific detection of duplex DNA for genomic profiling. *Nano Lett.* **10**, 738 (2010).
57. Lu, B., Albertorio, F., Hoogerheide, D. P. & Golovchenko, J. a. Origins and Consequences of Velocity Fluctuations during DNA Passage through a Nanopore. *Biophys. J.* **101**, 70–9 (2011).
58. Akeson, M., Branton, D., Kasianowicz, J. J., Brandin, E. & Deamer, D. W. Microsecond time-scale discrimination among polycytidylic acid, polyadenylic acid, and polyuridylic acid as homopolymers or as segments within single RNA molecules. *Biophys. J.* **77**, 3227 (1999).
59. Clarke, J. *et al.* Continuous base identification for single-molecule nanopore DNA sequencing. *Nat. Nanotechnol.* **4**, 265–270 (2009).

60. Cherf, G. M. *et al.* Automated forward and reverse ratcheting of DNA in a nanopore at 5-Å precision. *Nat. Nanotechnol.* **30**, 344 (2012).
61. Manrao, E. A. *et al.* Reading DNA at single-nucleotide resolution with a mutant MspA nanopore and phi29 DNA polymerase. *Nat. Biotechnol.* **30**, 349 (2012).
62. Reisner, W. W. *et al.* Statics and Dynamics of Single DNA Molecules Confined in Nanochannels. *Phys. Rev. Lett.* **94**, 196101 (2005).
63. De Gennes, P.-G. *Scaling Concepts in Polymer Physics*. (Cornell University Press, 1979).
64. Odijk, T. On the statistics and dynamics of confined or entangled stiff polymers. *Macromolecules* **16**, 1340 (1983).
65. Yang, Y., Burkhardt, T. & Gompper, G. Free energy and extension of a semiflexible polymer in cylindrical confining geometries. *Phys. Rev. E* **76**, 011804 (2007).
66. Wang, Y., Tree, D. R. & Dorfman, K. D. Simulation of DNA Extension in Nanochannels. *Macromolecules* **44**, 6594 (2011).
67. Persson, F., Utko, P., Reisner, W. W., Larsen, N. B. & Kristensen, A. Confinement spectroscopy: probing single DNA molecules with tapered nanochannels. *Nano Lett.* **9**, 1382 (2009).
68. Utko, P., Persson, F., Kristensen, A. & Larsen, N. B. Injection molded nanofluidic chips: fabrication method and functional tests using single-molecule DNA experiments. *Lab Chip* **11**, 303 (2011).
69. Levy, S. L. & Craighead, H. G. DNA manipulation, sorting, and mapping in nanofluidic systems. *Chem. Soc. Rev.* **39**, 1133 (2010).
70. Mannion, J. T., Reccius, C. H., Cross, J. D. & Craighead, H. G. Conformational analysis of single DNA molecules undergoing entropically induced motion in nanochannels. *Biophys. J.* **90**, 4538 (2006).
71. Han, J. & Craighead, H. G. Separation of Long DNA Molecules in a Microfabricated Entropic Trap Array. *Science* **288**, 1026 (2000).
72. Han, J., Turner, S. W. P. & Craighead, H. G. Entropic Trapping and Escape of Long DNA Molecules at Submicron Size Constriction. *Phys. Rev. Lett.* **83**, 1688 (1999).
73. Margulies, M. *et al.* Genome sequencing in microfabricated high-density picolitre reactors. *Nature* **437**, 376–80 (2005).

74. Thompson, J. F. & Steinmann, K. E. Single molecule sequencing with a HeliScope genetic analysis system. *Current protocols in molecular biology / edited by Frederick M. Ausubel ... [et al.]* **Chapter 7**, Unit7.10 (2010).

1.6 Figures

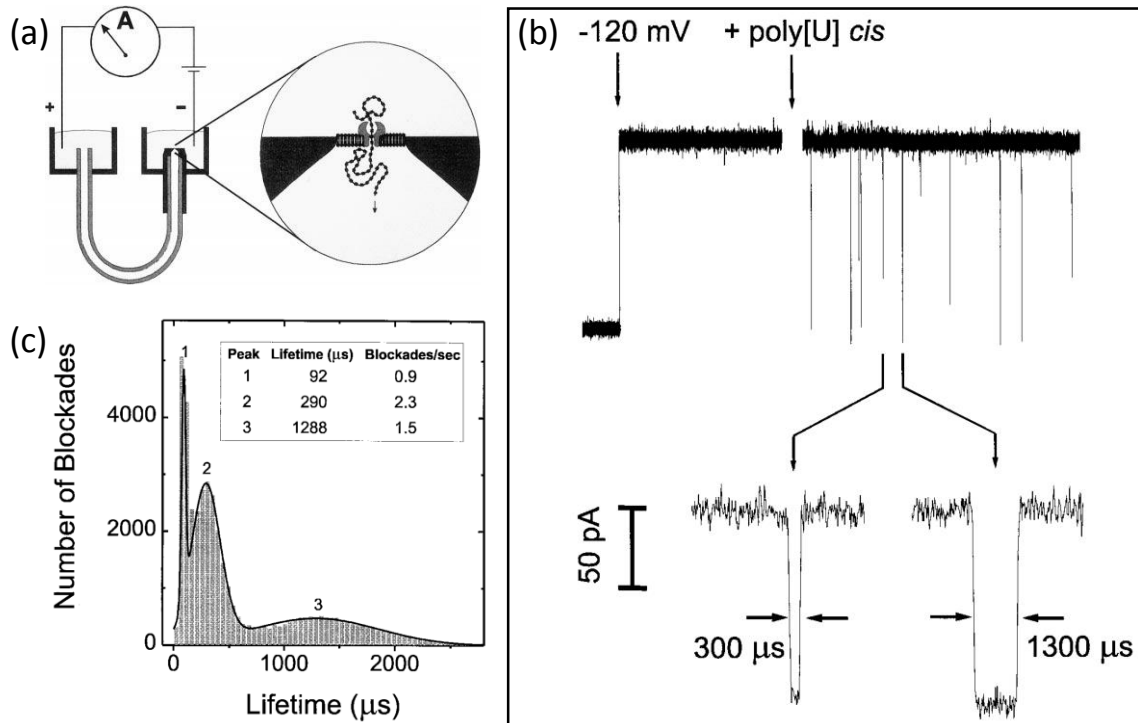


Figure 1.1 Translocation of ss-DNA or RNA through an α -hemolysin nanopore. **a)** Schematic representation of the experimental setup. **b)** Sample current traces observed during the translocation of polyU RNA. **c)** Distribution of the event duration observed for polyU showing three isolated event populations. Reprinted from reference 45, © 1996 National Academies of Science.

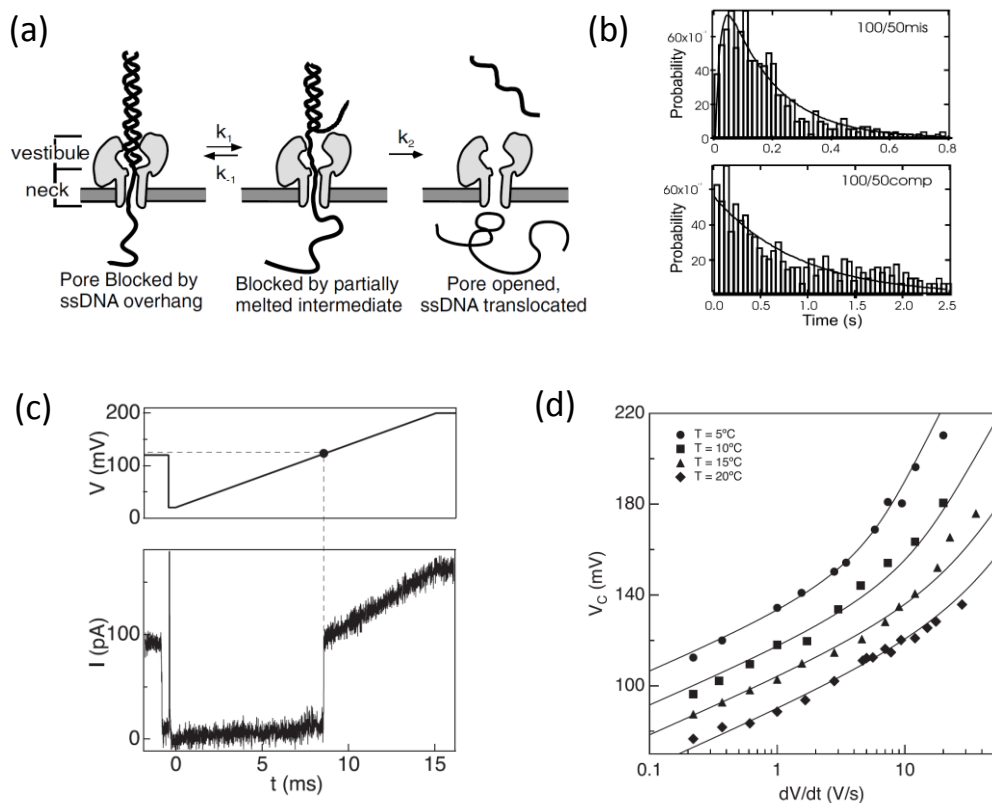


Figure 1.2 DNA unzipping experiments. **a)** Schematic representation of the DNA unzipping experiments **b)** The event durations for two synthetic DNA constructs. Both samples consist of a 50-bp duplex region and 50 base single strand overhang. The 100/50mis sample has mismatches in the duplex region while the 100/50com does not. **c)** Unzipping DNA with a voltage ramp measures the critical voltage. **d)** The critical voltage was found to depend on the temperature and the ramp rate.

(a) and (b) are reprinted from reference 48, © 2003 American Physical Society. (c) and (d) are reprinted from reference 49, © 2006 EDP Sciences, IOP Publishing, Italian Physical Society.

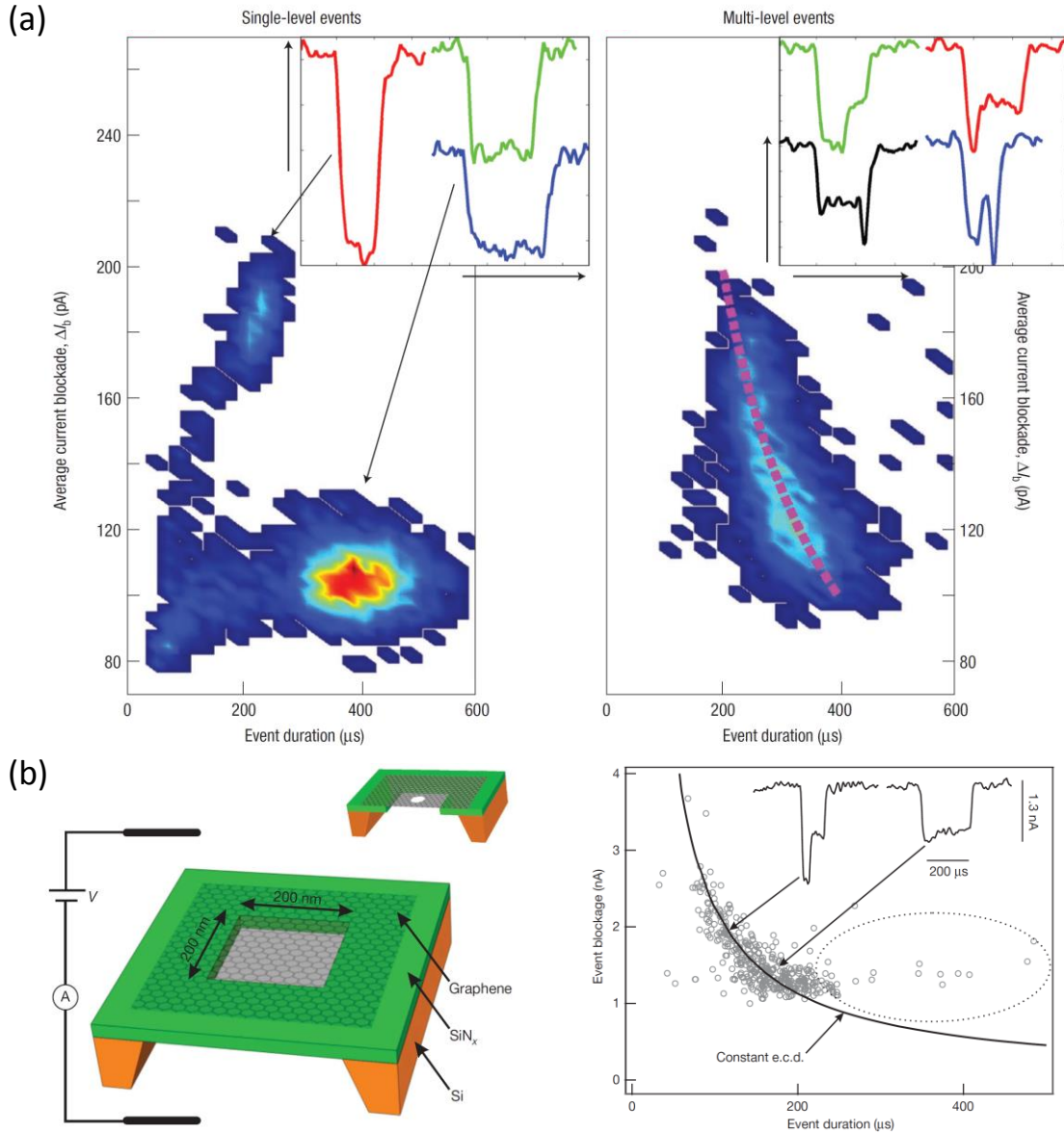


Figure 1.3 DNA translocation through solid-state nanopores in various folded configurations. **a)** DNA translocation through a 3 nm SiN_x nanopore. The distribution of the single-level events and the multi-level events are separated. The single-level events distribution show two clusters which can be attributed to translocation in an unfolded and folded from the middle configuration (left). The multi-level events show a relation between the increasing duration and the decreasing amplitude (right). **b)** DNA translocation through a 5 nm graphene nanopore. The distribution of the translocation events is similar to the experiment with the SiN_x pore.

(a) is reprinted from reference 53, © 2003 Nature Publishing Group. (b) is reprinted from reference 54, © 2010 Nature Publishing Group.

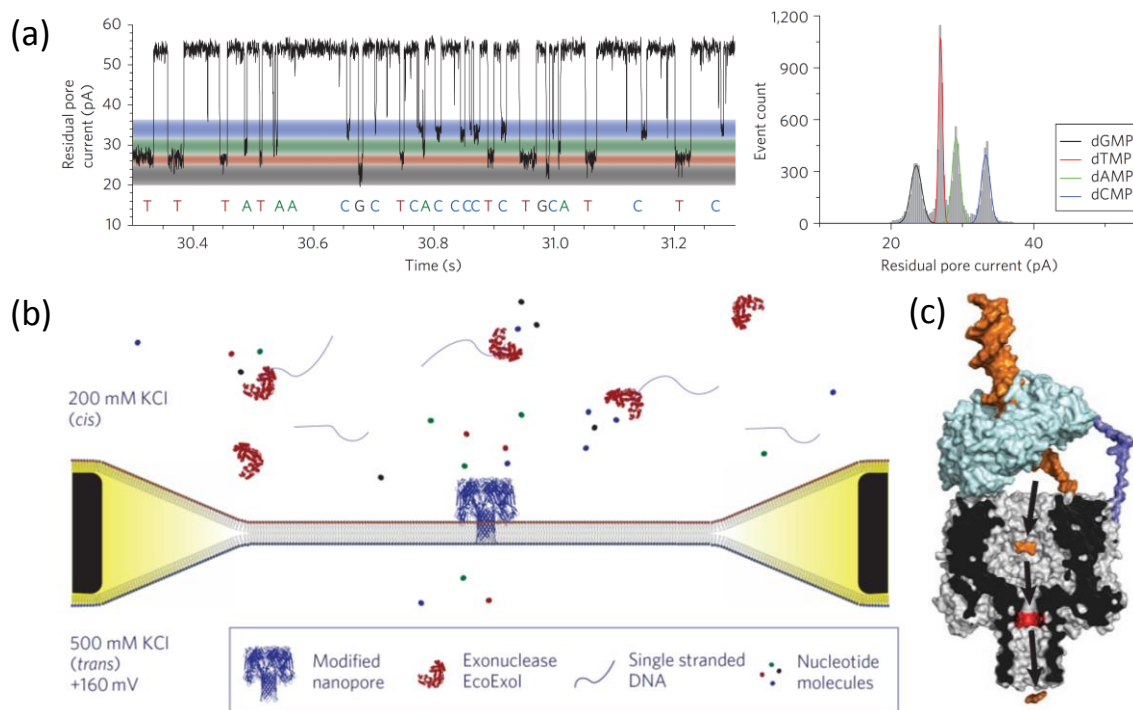


Figure 1.4 Discrimination between unlabeled nucleoside monophosphate molecules using a modified protein nanopore. a) Current trace and distributions show characteristic current blockade levels for each of the four nucleoside monophosphates. **b)** The setup can be used to detect nucleoside monophosphates released by exonuclease from ss-DNA. **c)** The concept is proposed for DNA sequencing using an exonuclease attached to the nanopore.

Reprinted from reference 59, © 2009 Nature Publishing Group.

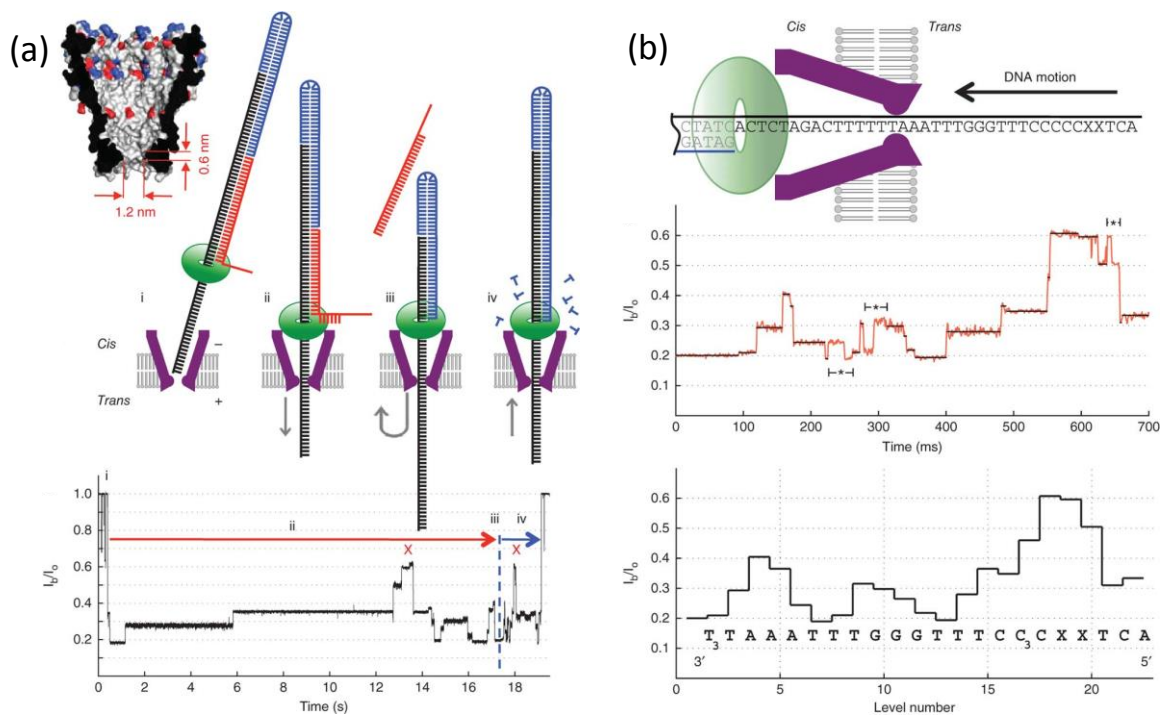


Figure 1.5 Reading DNA sequence using a nanopore and polymerase. a) Structure of the mutant MspA nanopore and a schematic of the experiment. b) A representative current trace of the synthesis step. The DNA sequence can be directly read from the trace.

Reprinted from reference 61, © 2012 Nature Publishing Group.

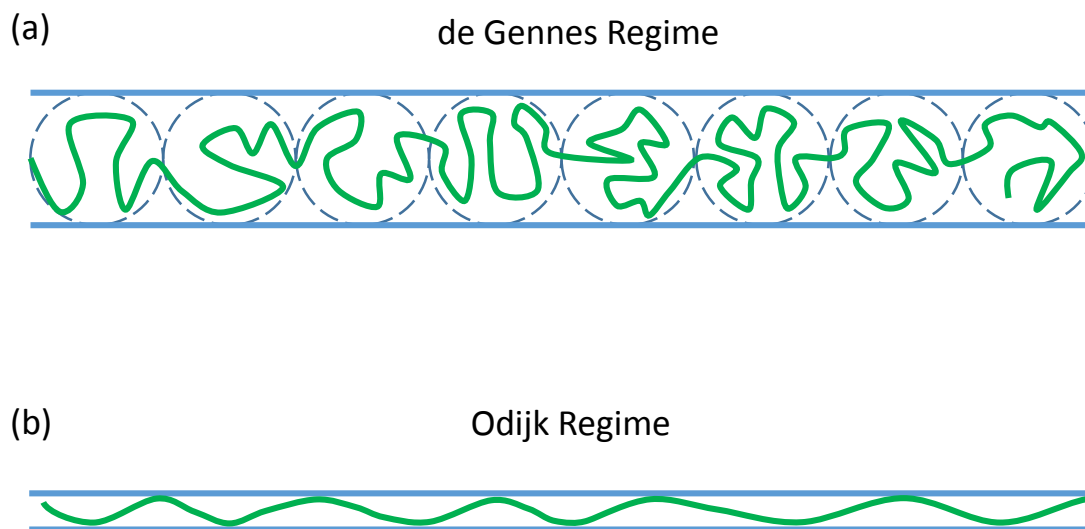


Figure 1.6 Schematic of nanochannel DNA confinement in different regimes. a) In the de Gennes regime, DNA consists of a series of blobs. **b)** In the Odijk regime, DNA consists of a series of deflected segments.

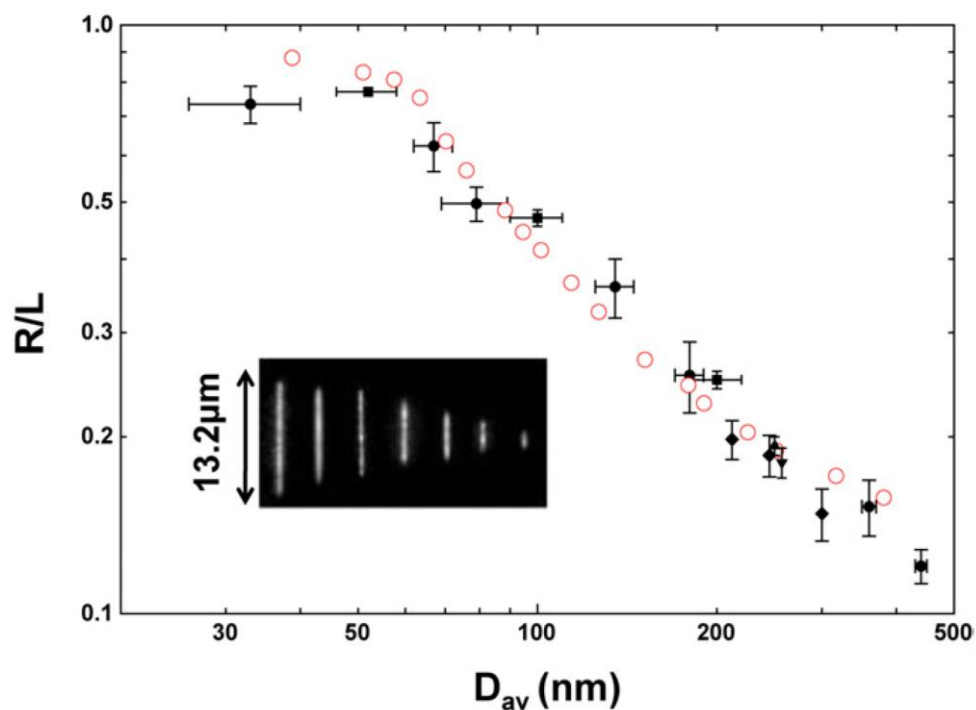


Figure 1.7 Summary of experimental results (black symbols) and simulation results (red circles) showing the scaling of the confined DNA extension length with channel dimensions. The inset shows profiles of λ -phage DNA molecules confined in nanochannels with diameters ranging from 30 to 440 nm.

Reprinted from reference 26, © 2012 IOP Publishing Ltd. Adapted from an original figure in reference 66, © 2011 American Chemical Society.

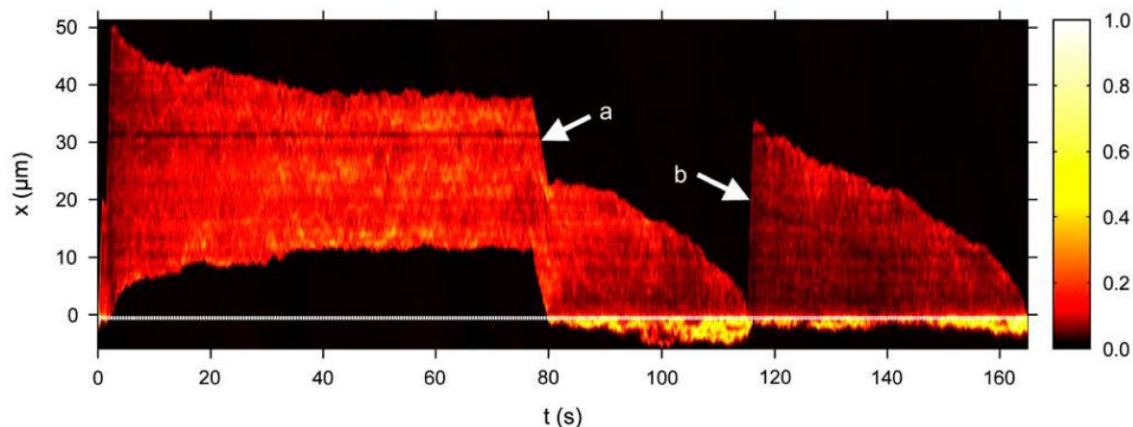


Figure 1.8 Various dynamic processes observed for a DNA molecule within a nanochannel. Intensity profiles of the DNA molecule are concatenated with time progressing along the horizontal axis. Brighter colors (yellow) indicate higher local DNA density. From 0 - 77 s, The DNA is first electrophoretically driven into the channel, and then the voltage is turned off. The DNA is elongated during the threading, and then relaxed freely to equilibrium size. From 77 - 80 s, the DNA is delivered to the entrance of the channel, then the voltage is turned off and the entropic force results in recoil (80 - 113 s). Starting from 113 s, the molecule is pulled into the channel and the voltage is turned off immediately when a small portion of the molecule is still outside of the nanochannel entrance. The molecule elastically relaxes while recoiling at the same time.

Reprinted from reference 70, © 2006 Cell Press.

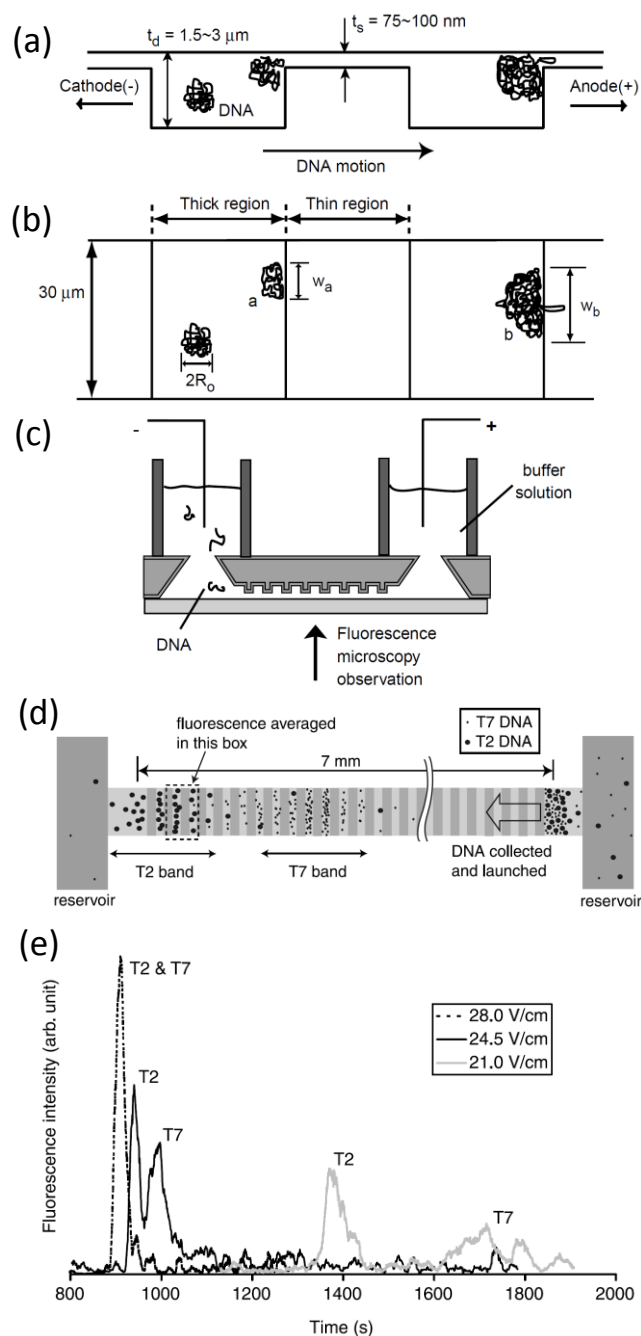


Figure 1.9 An entropic trap array for DNA separation. **a)** Schematic representation of the trap array (side view). **b)** Top view of the trap array. **c)** Overview of the device operation. **d)** Schematic showing how two types of long DNA molecules are separated in a 7 mm long channel. **e)** Experimental data showing the separation at different electric fields.

Reprinted from reference 71, © 2000 American Association for the Advancement of Science.

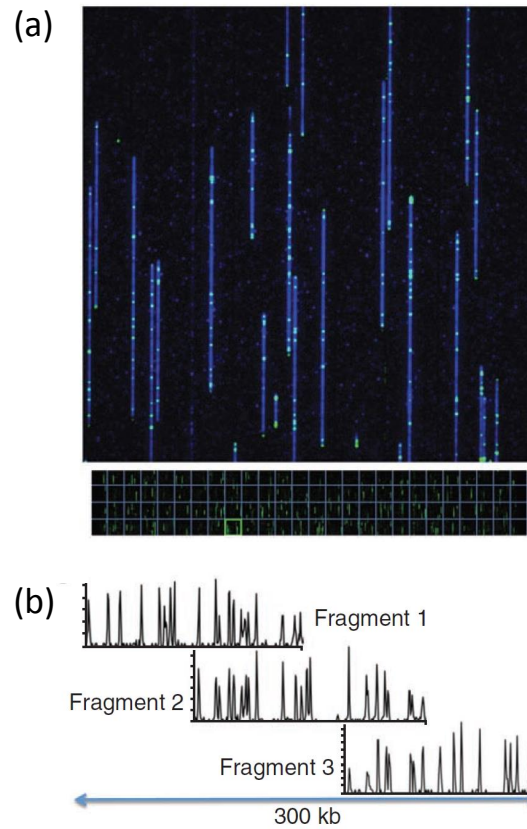


Figure 1.10 DNA mapping using nanochannels. **a)** Representative image showing the data collection. DNA is uniformly stretched and the location of the labels are clearly visible. **b)** Overlapping patterns are used to construct the map.
Reprinted from reference 22, © 2012 Nature Publishing Group.

Chapter 2: Fabrication of Nanofluidic ElementsIntroduction

The nanopores and nanochannels described in the previous chapter represent most of the nanofluidic platforms that have been used to interrogate individual macromolecules. These two classes of nanofluidic conduits differ both in their geometry and in their methods of fabrication. In this chapter, the available top-down methods of fabrication for the two platform classes are reviewed. This general discussion is then expanded with details of the protocols used to fabricate devices enabling the research described in later chapters of this Thesis.

2.1.1 Thin Membrane Nanopores

Much of the theory of confined macromolecules was developed decades before the ability to fabricate isolated nanopores and nanochannels. This was motivated by the need to understand the behavior of macromolecules constrained within tortuous networks of nanopores such as those found in polymer melts, gels, and high-surface-area filtration media.^{1,2} More facile comparisons between theory and experiment are expected as the nanoporous network becomes less complex and nanopore size distributions become narrower.³ Platforms with these characteristics include membranes of aligned, non-intersecting nanofluidic conduits such as those prepared in anodized aluminum oxide or track-etched polyethylene terephthalate films.⁴⁻⁶ Measuring transport through such porous membranes still requires sampling a population of molecules through a number of pores with some size variation. To better understand the transport phenomena of macromolecules through nanopores and nanochannels, measuring transport through a single pore would

therefore be preferred. This is precisely the approach taken by Kasiannowicz et al. in 1996 when they measured the transport of single-stranded DNA molecules through a single α -hemolysin pore traversing a lipid bilayer, initiating an interest in nanopore-based genomic sequencing.^{7,8}

Although protein pore complexes have precise self-assembled geometries and reproducible surface properties,⁸ these parameters cannot be easily varied over a wide range. The robustness of the pore-membrane system is limited by the sensitivity of the lipid bilayer to environmental conditions such as pressure, pH, and temperature.⁹ In contrast, nanopores traversing robust solid-state membranes can be fabricated with controlled size, geometry, and surface properties. Additionally, such platforms are more amenable to integration with additional external components.⁹⁻¹²

The first controlled fabrication of solid-state nanopores having dimensions comparable to those of transmembrane protein pore complexes was developed by Li et al. in 2001 using an ion beam sculpting method.¹³ The fabrication was conducted in a SiN_x membrane suspended on a silicon wafer. First, a bowl-shaped cavity was milled into the membrane from the back side using a Ga^+ ion beam. Then a diffuse beam of 3-kV Ar^+ ions was used to slowly remove additional material from the top side of the thinned membrane (Figure 2.1 a and b). The authors discovered that after pore formation, additional Ar^+ irradiation could produce either pore opening or closing, depending on whether the substrate temperature was below or above 5 °C, respectively. By counting the flux of ions passing through the pore, its size could be monitored in real time and precisely controlled.

Another method of pore fabrication was reported two years later by Storm et al.¹⁴ A 20 nm nanopore was first fabricated on a 340 nm thick silicon membrane using electron

beam lithography and anisotropic etching. After thermally oxidizing to SiO₂, the pore was either enlarged or shrunk using a 200-kV transmission electron microscope (TEM), depending on the beam current density. This technique enabled nanopore fabrication with single-nanometer precision. The focused high energy electron beam produced by TEM also directly milled nanopores through thin membranes with the pore size adjusted in situ using an enlarged beam spot (Figure 2.1 c - h).^{14,15} Later work by Howitt et al. determined that pores were milled using 150-keV electrons but that 120-keV electrons were insufficiently energetic to affect milling.¹⁶ However, even lower energy focused electron beam (FEB, 0.2 – 20 keV) were used to fabricate nanopores, but with a gas assisted mechanism.¹⁷

The availability of 200-kV TEMs and the precision of the FEB method have made this the preferred protocol for nanopore fabrication. Figure 2.2 shows representative nanostructures fabricated using this method. The JEOL 2010F-FasTEM was operated at 200 kV to mill these features into a 60-nm thick SiN_x membrane. The nanopore (Figure 2.2 a) was milled by focusing the electron beam to a caustic spot and exposing the membrane for ~ 1 min. The “UNC” (Figure 2.2 b) was milled by connecting a series of nanopores.

The analogous use of a focused He⁺ ion beam to mill nanopores through thin solid-state membranes has also been demonstrated.¹⁸ The ability to load wafer-scale samples into a helium ion microscope (HIM) and the faster milling rate of He⁺ ions results in much higher throughput in the preparation of pore-containing membranes. HIM instruments have not been widely adopted, however, and access is limited.

Other methods for making and modifying nanopores have also been explored.^{9,19–27} The track-etching method produces high aspect ratio conical single pore or pore arrays by etching a polymer membrane along paths previously irradiated by ions.^{20,27,28} If the size

requirements are relaxed, a number of other techniques can be used to fabricate nanopores having diameters that are tens of nanometers, including focused ion beam (FIB) milling using a standard Ga^+ ion source and electron beam lithography followed by reactive ion etching.^{14,25} Pore sizes can be reduced by subsequently depositing an insulating film on the membrane and within the nanopore. Atomic layer deposition (ALD) creates conformal coatings on the nanopore and membrane surfaces with single angstrom precision, reducing feature sizes. Such coatings have been shown to change the surface charge and reduce the $1/f$ noise.²⁹

2.1.2 Planar Nanochannels

Nanofluidic conduits can also be patterned laterally across the top surface of substrates having arbitrary thicknesses. In the top down approach, this is accomplished by directly removing material from the substrate. Methods for removing material include direct write techniques such as FIB milling or patterning the features into a resist layer and subsequently transferring the pattern into the underlying substrate using an etching technique. After patterning these “trenches” in the substrate surface, a coverplate is bonded to the substrate to complete the channels and generate the fluidic network.³⁰ In principal, channels ranging in length from nanometers to centimeters can be patterned. The most common example of this general method is the use of conventional optical lithography for fabricating a nanoslit, where the fluidic element is typically microns in width and nanoscale in depth.^{31,32} The channels are patterned on a silicon or glass substrate, followed by a reactive ion or wet etching process. Channel depth is controlled by the etching parameters and $< 20\text{-nm}$ deep channels have been successfully fabricated and their use demonstrated for various analytical

applications.^{31,33,34} In most cases, this method generates nanochannels with a uniform depth profile, but modification at the exposure step could lead to a gradient depth profile.³⁵

The smallest feature size that can be exposed in a resist layer using contact photolithography is limited by the exposure wavelength.³² The feature size that can be achieved using electron beam lithography (EBL), on the other hand, is determined by the size of the electron probe (~1 nm) and the scattering volume of electrons in resist materials. Features with critical dimensions below 10 nm have been demonstrated³⁶

Another low cost and high throughput technique is nanoimprint lithography.^{37,38} Nanoscale features are first hot-embossed into a thin conformable resist layer using a rigid mold. After the mold is removed, anisotropic reactive ion etching (RIE) is used to reproduce the features on the substrate. This technique can simultaneously transfer patterns having a range of sizes over large substrates. It should be noted that the preparation of the mold requires another nanofabrication technique such as electron beam lithography to produce the nanosize features.

An alternative to lithographic methods is to pattern the nanochannels directly into the substrate. This has been realized using FIB milling, where 30 keV Ga^+ ions were used to mill features into a conductive substrate.³⁹ These massive ions are focused to spot that is typically 10-50 nm in diameter and impact the substrate at speeds of several hundred km s^{-1} .⁴⁰ The kinetic energy of the incident ions is transferred to atoms in the substrate and the series of collisional cascades results in mechanical sputtering of substrate atoms and particles away from the surface. Insulating substrates such as fused quartz can also be patterned by first depositing a conductive film onto the substrate surface to be milled.^{41,42} This film dissipates the charge induced by ions impacting the surface. It also prevents redeposition and adhesion

of sputtered material on the substrate surface. Material that is redeposited on top of the conductive film will be lifted off when the film is removed using an etching solution. Finally, the sacrificial conductive film can act as a masking layer, effectively further focusing the ion beam that impacts the underlying substrate and enabling the patterning of features smaller than 5 nm.⁴³ The fabrication using FIB milling discussed in this Chapter is based on this technique and all of the substrates are fused quartz coated with a 120-nm thick Cr film unless otherwise noted.

2.2 Milling Three-Dimensional Features using a Focused Ion Beam

2.2.1 Instrumentation

Nanoscale features were fabricated using a FEI Helios 600 NanoLab™ DualBeam™ instrument (Figure 2.3). It is equipped with a high-resolution electron beam and a gallium ion beam. The accelerating voltage range of the electron beam is 0.5-30 kV. The ultimate imaging resolution is 0.9 nm at 15 kV. Ions can be extracted from a liquid metal ion source (LMIS) and accelerated at a voltage of 1-30 kV, with aperture defined ion beam currents ranging from 1.5 pA to 20 nA. The imaging resolution using the minimal beam current is 5 nm at 30 kV. Additionally, the instrument is equipped with gas-injection systems for enhanced etching (XeF₂) and material deposition (Pt, W, and SiO₂). All milling and ion beam imaging described in this Thesis were conducted using a 30 kV accelerating voltage.

Patterning with the ion beam is fully software controlled with a number of adjustable parameters. The accelerating voltage determines the beam energy while a user selectable beam-limiting aperture defines the probe size and incident ion current. These parameters determine the smallest feature one can fabricate and the sputtering yield. In addition to the beam profile, the speed with which the beam is scanned over the substrate and the number of

passes over the patterned region also affect the quality of the patterned features. The sputtering behavior is complex, depending on the incident angle and any redeposition.⁴⁴ Both effects are affected by the sample topography so the details of beam rastering have an influence on the milling results.

There are several basic pre-configured patterns such as lines, circles, rectangles, and polygons. To make a desired feature the beam is normally scanned over the same pattern many times, making multiple passes. This produces a cleaner feature than patterning with a single pass because small amounts of redeposited material are repeatedly cleared.⁴⁵ Users can set the dwell time and the number of passes and the program reports an estimated depth of the feature based on these parameters, the beam current density, and the sputtering yield of the substrate material. The actual depth may vary significantly from this expected value based on the details of the pattern geometry and must be empirically determined. In addition to the simple geometric patterns, the user can raster the beam in a more elaborate pattern defined by a bitmap image. Each pixel has a size equivalent to the radius of the focused ion beam spot and defines the positions where the beam dwells on the substrate. The grayscale intensity for each pixel defines the dwell time. For example, if a dwell time of 10 μs is set by the user for a pattern then the beam will dwell for 10 μs on white pixels, 0 μs on black pixels, and intermediate dwell times for gray pixels. The dwell time scales linearly with the pixel intensity on a scale between 0-255 such that a gray pixel with an intensity value of 127 would indicate a dwell time of 5 μs in the above example. Patterning features into a substrate using a bitmap image provides precise control over all dimensions, with a minimum pixel size of 5 nm and depth gradations consisting of 256 levels.

As described in Chapter 1, the behavior of confined DNA molecules is sensitive to size of the nanochannel in which they are contained. The description above details how nanochannel size can be precisely controlled in all three dimensions using FIB milling, assuming the correct parameters are defined by the instrument operator. These parameters are validated by the in situ metrology of test features that are milled prior to the operational nanochannel. The width and length of features are readily determined by nondestructive imaging using the electron beam in the instrument. To determine the feature depth, however, it is necessary to first FIB mill a cross-section of the test feature and then image the exposed profile. Profile imaging is facilitated by the tilted orientation of the substrate relative to the electron beam (52 °). Once the user determines that the test feature is the desired depth, he uses those instrument settings to mill the actual nanochannel. The final metrology of the operational nanochannel is performed after removal of the Cr film using scanning electron microscope (SEM) imaging and Atomic force microscopy (AFM) profiling.

2.2.2 Relationship between Ion Dose and Feature Depth

Before using the bitmap patterning mode to fabricate three-dimensional features, the relationship between the ion beam dose and feature depth was quantitatively characterized. A series of six $1\text{ }\mu\text{m} \times 1\text{ }\mu\text{m}$ squares was milled using a 28 pA (17 nm diameter) probe that was rastered an identical number of times (1701) over each square. Each square in the series was milled using a different beam dwell time (1, 2, 3, 4, 5, or 6 μs). After the patterns were milled, they were cross sectioned and imaged using the electron beam in the DualBeamTM instrument to determine their depths (Figure 2.4). A depth of zero was defined as the interface between the quartz substrate and the protecting Cr film. In the case of the 1- μs dwell time conditions, the feature did not penetrate into the quartz substrate and its “depth” is

therefore reported as a negative value. As expected, the measured depth showed a linear dependence on the dwell time. This is an important prerequisite for the controlled patterning of complex three-dimensional features using the bitmap patterning mode in which depths are controlled by the per pixel dwell times.

2.2.3 Milling Nanochannels with Integrated Three-Dimensional Nanofunnels

The control of DNA transport through nanofluidic channels is the central problem discussed in the following chapters. One strategy for increasing the level of control over the introduction of DNA molecules into a nanofluidic channel is to engineer the gradual transition of the DNA molecule from its bulk conformation to the fully confined state. By using a three-dimensional nanofunnel to guide the DNA into the nanochannel, a gradual variation in the degree of confinement is introduced by the nanofunnel's depth and width. FIB milling is an ideal nanofabrication technique for milling the nanofunnel because it simultaneously controls the feature width and depth using a grayscale bitmap. The linear relationship between the dwell time and the milling depth described above is observed as long as the pattern is wide enough. As the pattern becomes narrower than several hundred nanometers, however, material redeposition becomes more important, and the depth becomes significantly shallower. To compensate for this, the dwell time is increased for these narrow regions. A drawback to simply correcting the dwell time for the narrow nanochannel features is that the intersection of the nanochannel and the nanofunnel is milled deeper than desired. To compensate for this, the pixels at the interface were optimized empirically. Figure 2.5 shows the bitmap images used to mill the accompanying triangular and hyperbolic funnels. The SEM images show a tilted (52°) view of the features in order to better show the gradually changing depth of the funnels.

2.3 Milling Nanofluidic Structures using Multiple Ion Beam Currents

2.3.1 Motivation and Challenges

The nanofunnel and nanochannel patterns described above were milled using a single bitmap to ensure maximum precision in the integration of these features. Multiple regions (bitmaps, lines, rectangles, etc.) can also be drawn, arranged, and milled in a single patterning series with nanometer precision. This requires selecting a single ion beam current that is appropriate for all features in the desired pattern, however. If features of widely different sizes (corresponding to different volumes of material that must be sputtered) are desired, then a single ion beam current may not be appropriate for this task. A low ion beam current will enable milling of features with small critical dimensions but the milling time for the larger features could be prohibitively long. Conversely, a high ion beam current will mill the larger features in a reasonable time frame but the probe diameter could be too large to mill fine features with the desired dimensions. Table 2.1 summarizes the beam diameters and the milling time for a $1\text{ }\mu\text{m}^3$ volume at different beam current conditions. The cost of a long patterning time is diminished throughput but, more importantly, the fact that over time sample drift can degrade milling precision. Milling times < 10 minutes are typically targeted.

The act of changing the beam current consists of changing a beam-limiting aperture. This is a mechanical process that requires the user to align the various column components (aperture position, stigmation coils, etc.). Pattern elements milled using different beam currents must therefore be milled sequentially. The quality of their integration is controlled by the precision of aligning a second pattern to the location of an existing feature in a scanning ion image. This is inherently less precise than defining multiple pattern elements that are arranged in a patterning file and then milled in a single run.

The development of a multiple beam current approach was motivated by the desire to integrate a narrow (~20 nm wide) nanochannel with a nanofunnel that gradually decreased in diameter from 1.5 μm to 100 nm. Such a narrow nanochannel produces a DNA sensitive axial ionic current (similar to a nanopore through a thin membrane) while allowing the simultaneous fluorescence imaging of DNA molecules. The incorporation of the nanofunnel reduces the magnitude of the electric field required to induce DNA translocation and provides greater control over transport dynamics. Milling such a narrow nanochannel requires the use of the smallest beam current (1.5 pA) and takes ~2 min (for a 3- μm long nanochannel). The incorporated nanofunnel is milled in 3 min using a beam current of 0.46 nA. To remove this volume of material using the 1.5 pA beam would take an estimated 15 hours.

2.3.2 Milling 20-nm Nanochannels with Integrated Nanofunnels

The nanofunnel is initially milled into the substrate using an ion beam current of 0.46 nA. The substrate is removed from the FIB, the Cr film is chemically etched, and a new 120-nm thick Cr film is then deposited. This film prevents charging but also protects the existing nanofunnel from unintentional ion beam damage. The nanochannel is then milled using a 1.5 pA ion beam current, intersecting the narrow end of the nanofunnel. As a final step, large vias are milled into the substrate, connecting the termini of the nanochannel/nanofunnel duplex with the microfluidic channels. Figure 2.6 shows SEM images taken at different steps during the process of fabricating a 20-nm channel with an integrated three-dimensional funnel. Figure 2.6a shows the smooth surface between two microchannels before milling. A series of identical funnels were milled using a 0.46-nA beam current (Figure 2.6b). Following this step, the Cr layer was removed using an etching solution (Transene Company,

Inc.), and a new 120-nm thick Cr layer was deposited using an ion beam sputtering system (Model IBS/e, South Bay Technologies, Inc.).

Patterning a small nanochannel with precise depths is more difficult than with larger features, as the tolerance is much smaller. A 10 nm error for a 100 nm channel is acceptable, but not for a 20 nm channel. To make the shallowest channel possible, several channels bracketing a range of depth settings were milled. Figure 2.6c shows the SEM image recorded immediately after milling. Because of the protecting Cr film, the depths of these channels look identical. After removal of the Cr film, a new 10 nm Cr film was deposited and SEM images were taken again (Figure 2.6d). High magnification SEM images (not shown) indicated that only the rightmost channel was milled into the substrate. Next, the substrate was removed from the instrument and an additional 80 nm of Cr was deposited to protect the nanochannels. The designated nanochannel was connected to the microchannels by milling relatively large vias (Figure 2.6e). Figure 2.6f shows a higher magnification view of the nanofunnel and nanochannel, along with the milled features that connect the nanochannel to the microchannel. It should be noted that the nanochannel is slightly deeper at the intersection with the nanofunnel, despite the efforts made to protect the substrate and feature surfaces using 100-nm thick Cr films throughout the fabrication protocol.

2.4 Fabrication of Nanochannels using a Focused Electron Beam

2.4.1 Introduction

The fabrication of features as small as 3 nm has been demonstrated using FIB milling. This was accomplished by using a thick (300 nm) Cr film as a charge conducting and masking layer on a fused quartz substrate.⁴¹ The milling of such features is not routine, however, and the significant milling time, imprecision in the user-defined feature depth, and

relative variance in channel dimensions are significant challenges. On the other hand, focused electron beam (FEB) milling has been used routinely to create nanopores in solid-state membranes as small as 1 nm with sub-nanometer precision. The milling of nanochannels on thick (electron opaque) substrates, however, has not been reported.

The discovery of FEB milling as a viable tool for fabricating nanopores in solid-state membranes has motivated recent research on the mechanism of the process. This work expands on decades of research into the mechanisms of damage induced by high-energy electron beams,^{46–48} ironically a phenomenon avoided at all costs by electron microscopists. Wu et al. reported that use of a focused electron beam to mill a ~10 nm nanopore in a 60 nm thick membrane resulted in the concurrent thinning of the adjacent area. This depletion area is ~40 nm in diameter for a SiN_x membrane and ~70 nm in diameter for a SiO₂ membrane. The authors speculated that under the high intensity beam the material is liquidus and atom diffusion created this depletion area. They also speculated that the sputtering of material occurs from both the top and bottom sides of the irradiated area.^{49,50}

Howitt et al. characterized the material loss rate for silicon and nitrogen from a SiN_x membrane. They concluded, in contrast to Wu et al., that the mechanism of pore milling is direct atom displacement from the exit side of the membrane (i.e., in the direction of electron transmission).¹⁶ Given these conflicting models of the electron beam induced sputtering, it remains unclear whether FEB milling of features in a thick substrate is a viable fabrication technique.

2.4.2 Trials using a High Energy (200 kV) Electron Beam

An obstacle to studying the FEB milling of a thick substrate is the rarity of microscopes capable of the necessary experiments. A typical transmission electron microscope capable of milling a nanopore requires an electron transparent membrane in order to monitor the formation of the pore in real-time. In order to demonstrate milling in an electron opaque substrate, experiments were attempted on a Hitachi HD-2000 STEM installed at Oak Ridge National Laboratory. This instrument has a high intensity cold field emission gun source, can be operated using extraction voltages up to 200 kV, and is unusual in that it is equipped with a secondary electron detector. It is therefore capable of producing an electron beam with sufficient intensity and energy to induce damage while allowing real time monitoring of the process in thick substrates. Unfortunately, it was not possible to characterize FEB milling in this experiment, as any milling was inhibited by beam-induced deposition of carbon on the substrate. The fact that rigorous plasma cleaning of the substrate did not ameliorate the situation indicated that the source of the contamination was the microscope column. Figure 2.7 shows carbonaceous spots and lines that were deposited on the substrate by parking the beam in spot mode or rastering over a line, respectively.

2.4.3 Material Damage on Quartz Substrates using a Low Energy (10 kV) Beam

While attempts using a high-energy electron beam to directly mill features on a thick substrate were not successful, the lower energy beam in a SEM instrument was found to induce damage on a fused quartz substrate. Figure 2.8 shows two examples of such effects. In both cases, damage was induced on fused quartz substrates coated with a 10-nm Cr film. The AFM images showing the damage (Figures 2.8b, c) were scanned after this Cr film was removed, indicating that the damage was indeed on the quartz surface. Figures 2.8a, b show

that scanning the SEM electron beam over small regions of the substrate for extended periods can cause material removal, observed as depressed regions in the AFM profiles.

A more controlled attempt at patterning features is shown in Figures 2.8c, d. The 10-kV electron beam was rastered in a linear fashion over the surface. While the focused electron probe had a diameter of ~1 nm, the milled channel was about 700 nm wide and 8 nm deep. Such a wide region of damage induced by a low energy electron beam is unlikely caused by direct atom displacement.¹⁶ It is more likely caused by the residual water assisted etching mechanism reported by Spinney et al.¹⁷

2.5 Conclusion and Future Directions

Various methods for fabricating nanofluidic elements were discussed along with a discussion of the development of FIB milling for patterning complex nanostructures. In the next few chapters, the use of these nanostructures in nanofluidic applications, primarily for analyzing individual DNA molecules, is discussed. The development of milling using a focused electron beam proved less successful, however, and was not pursued further. Nonetheless, the results and discussion above suggest some future possibilities for nanofabrication using focused electron and ion beams.

2.6 REFERENCES

1. Viovy, J.-L. Electrophoresis of DNA and other polyelectrolytes : Physical mechanisms. *Rev. Mod. Phys.* **72**, 813 (2000).
2. Salieb-Beugelaar, G. B., Dorfman, K. D., van den Berg, A. & Eijkel, J. C. T. Electrophoretic separation of DNA in gels and nanostructures. *Lab Chip* **9**, 2508 (2009).
3. Volkmuth, W. D. & Austin, R. H. DNA electrophoresis in microlithographic arrays. *Nature* **358**, 600 (1992).
4. Chik, H. & Xu, J. M. Nanometric superlattices: non-lithographic fabrication, materials, and prospects. *Mater. Sci. Eng.* **43**, 103 (2004).
5. Jiang, J., Li, Y., Liu, J. & Huang, X. Building one-dimensional oxide nanostructure arrays on conductive metal substrates for lithium-ion battery anodes. *Nanoscale* **3**, 45 (2011).
6. Apel, P. Track etching technique in membrane technology. *Radiat. Meas.* **34**, 559 (2001).
7. Kasianowicz, J. J., Brandin, E., Branton, D. & Deamer, D. W. Characterization of individual polynucleotide molecules using a membrane channel. *Proc. Natl. Acad. Sci. USA* **93**, 13770 (1996).
8. Kasianowicz, J. J., Robertson, J. W. F., Chan, E. R., Reiner, J. E. & Stanford, V. M. Nanoscopic porous sensors. *Annu. Rev. Anal. Chem.* **1**, 737 (2008).
9. Healy, K., Schiedt, B. & Morrison, A. P. Solid-state nanopore technologies for nanopore-based DNA analysis. *NANOMEDICINE-UK* **2**, 875 (2007).
10. Murray, R. W. Nanoelectrochemistry: metal nanoparticles, nanoelectrodes, and nanopores. *Chem. Rev.* **108**, 2688 (2008).
11. Branton, D. *et al.* The potential and challenges of nanopore sequencing. *Nat. Biotechnol.* **26**, 1146 (2008).
12. Wanunu, M. Nanopores: A journey towards DNA sequencing. *Phys. Life. Rev.* **9**, 125 (2012).
13. Li, J. *et al.* Ion-beam sculpting at nanometre length scales. *Nature* **412**, 166 (2001).
14. Storm, A. J., Chen, J. H., Ling, X. S., Zandbergen, H. W. & Dekker, C. Fabrication of solid-state nanopores with single-nanometre precision. *Nat. Mater.* **2**, 537 (2003).

15. Ho, C. *et al.* Electrolytic transport through a synthetic nanometer-diameter pore. *Proc. Natl. Acad. Sci. USA* **102**, 10445 (2005).
16. Howitt, D. G., Chen, S. J., Gierhart, B. C., Smith, R. L. & Collins, S. D. The electron beam hole drilling of silicon nitride thin films. *J. Appl. Phys.* **103**, 024310 (2008).
17. Spinney, P. S., Howitt, D. G., Smith, R. L. & Collins, S. D. Nanopore formation by low-energy focused electron beam machining. *Nanotechnology* **21**, 375301 (2010).
18. Yang, J. *et al.* Rapid and precise scanning helium ion microscope milling of solid-state nanopores for biomolecule detection. *Nanotechnology* **22**, 285310 (2011).
19. Siwy, Z., Dobrev, D., Neumann, R., Trautmann, C. & Voss, K. Electro-responsive asymmetric nanopores in polyimide with stable ion-current signal. *Appl. Phys. A* **76**, 781 (2003).
20. Harrell, C. C. *et al.* Resistive-pulse DNA detection with a conical nanopore sensor. *Langmuir* **22**, 10837 (2006).
21. Karhanek, M., Kemp, J. T., Pourmand, N., Davis, R. W. & Webb, C. D. Single DNA molecule detection using nanopipettes and nanoparticles. *Nano Lett.* **5**, 403 (2005).
22. Wang, G., Zhang, B., Wayment, J. R., Harris, J. M. & White, H. S. Electrostatic-gated transport in chemically modified glass nanopore electrodes. *J. Am. Chem. Soc.* **128**, 7679 (2006).
23. Zhang, B. *et al.* Bench-top method for fabricating glass-sealed nanodisk electrodes, glass nanopore electrodes, and glass nanopore membranes of controlled size. *Anal. Chem.* **79**, 4778 (2007).
24. Park, S. R., Peng, H. & Ling, X. S. Fabrication of nanopores in silicon chips using feedback chemical etching. *Small* **3**, 116 (2007).
25. Gierak, J. *et al.* Sub-5nm FIB direct patterning of nanodevices. *Microelectron. Eng.* **84**, 779 (2007).
26. Wei, C., Bard, A. J. & Feldberg, S. W. Current Rectification at Quartz Nanopipet Electrodes. *Anal. Chem.* **69**, 4627 (1997).
27. Apel, P. Y., Korchev, Y. ., Siwy, Z., Spohr, R. & Yoshida, M. Diode-like single-ion track membrane prepared by electro-stopping. *Nucl. Instrum. Meth. B* **184**, 337 (2001).
28. Siwy, Z., Dobrev, D., Neumann, R., Trautmann, C. & Voss, K. Electro-responsive asymmetric nanopores in polyimide with stable ion-current signal. *Appl. Phys. A* **76**, 781 (2003).

29. Chen, P. *et al.* Atomic Layer Deposition to Fine-Tune the Surface Properties and Diameters of Fabricated Nanopores. *Nano Lett.* **4**, 1333 (2004).
30. Mijatovic, D., Eijkel, J. C. T. & van den Berg, A. Technologies for nanofluidic systems: top-down vs. bottom-up--a review. *Lab Chip* **5**, 492 (2005).
31. Mao, P. & Han, J. Fabrication and characterization of 20 nm planar nanofluidic channels by glass-glass and glass-silicon bonding. *Lab Chip* **5**, 837 (2005).
32. Okazaki, S. Resolution limits of optical lithography. *J. Vac. Sci. Technol. B* **9**, 2829 (1991).
33. Zeze, D. a. *et al.* Reactive ion etching of quartz and Pyrex for microelectronic applications. *J. Appl. Phys.* **92**, 3624 (2002).
34. Haneveld, J., Jansen, H., Berenschot, E., Tas, N. & Elwenspoek, M. Wet anisotropic etching for fluidic 1D nanochannels. *J. Micromech. Microeng.* **13**, S62 (2003).
35. Cao, H., Tegenfeldt, J. O., Austin, R. H. & Chou, S. Y. Gradient nanostructures for interfacing microfluidics and nanofluidics. *Appl. Phys. Lett.* **81**, 3058 (2002).
36. Madou, M. J. *Fundamentals of Microfabrication: The Science of Miniaturization*. (CRC press LLC, 2002).
37. Chou, S. Y., Krauss, P. R. & Renstrom, P. J. Imprint Lithography with 25-Nanometer Resolution. *Science* **272**, 85 (1996).
38. Guo, L. J. Nanoimprint Lithography: Methods and Material Requirements. *Adv. Mater.* **19**, 495 (2007).
39. Campbell, L. C., Wilkinson, M. J., Manz, A., Camilleri, P. & Humphreys, C. J. Electrophoretic manipulation of single DNA molecules in nanofabricated capillaries. *Lab Chip* **4**, 225 (2004).
40. Gierak, J. Focused ion beam technology and ultimate applications. *Semicond. Sci. Tech.* **24**, 043001 (2009).
41. Menard, L. D. & Ramsey, J. M. Fabrication of sub-5 nm nanochannels in insulating substrates using focused ion beam milling. *Nano Lett.* **11**, 512 (2011).
42. Riehn, R. *et al.* Restriction mapping in nanofluidic devices. *Proc. Natl. Acad. Sci. USA* **102**, 10012 (2005).
43. Menard, L. D. & Ramsey, J. M. Fabrication of sub-5 nm nanochannels in insulating substrates using focused ion beam milling. *Nano Lett.* **11**, 512 (2011).

44. Han, J., Lee, H., Min, B.-K. & Lee, S. J. Prediction of nanopattern topography using two-dimensional focused ion beam milling with beam irradiation intervals. *Microelectron. Eng.* **87**, 1 (2010).
45. Volkert, C. A., Minor, A. M. & Editors, G. Focused Ion Beam Micromachining. *MES Bull.* **32**, 389 (2007).
46. Bullough, T. J. Sputtering and the formation of nanometre voids and holes in aluminium in a scanning transmission electron microscope. *Philos. Mag. A* **75**, 69 (1997).
47. Salisbury, I. G., Timsit, R. S., Berger, S. D. & Humphreys, C. J. Nanometer scale electron beam lithography in inorganic materials. *Appl. Phys. Lett.* **45**, 1289 (1984).
48. Mochel, M. E. Electron beam writing on a 20-Å scale in metal β -aluminas. *Appl. Phys. Lett.* **42**, 392 (1983).
49. Wu, M.-Y., Krapf, D., Zandbergen, M., Zandbergen, H. W. & Batson, P. E. Formation of nanopores in a SiN/SiO₂ membrane with an electron beam. *Appl. Phys. Lett.* **87**, 113106 (2005).
50. Wu, M.-Y. *et al.* Control of shape and material composition of solid-state nanopores. *Nano Lett.* **9**, 479 (2009).

2.7 Tables and Figures

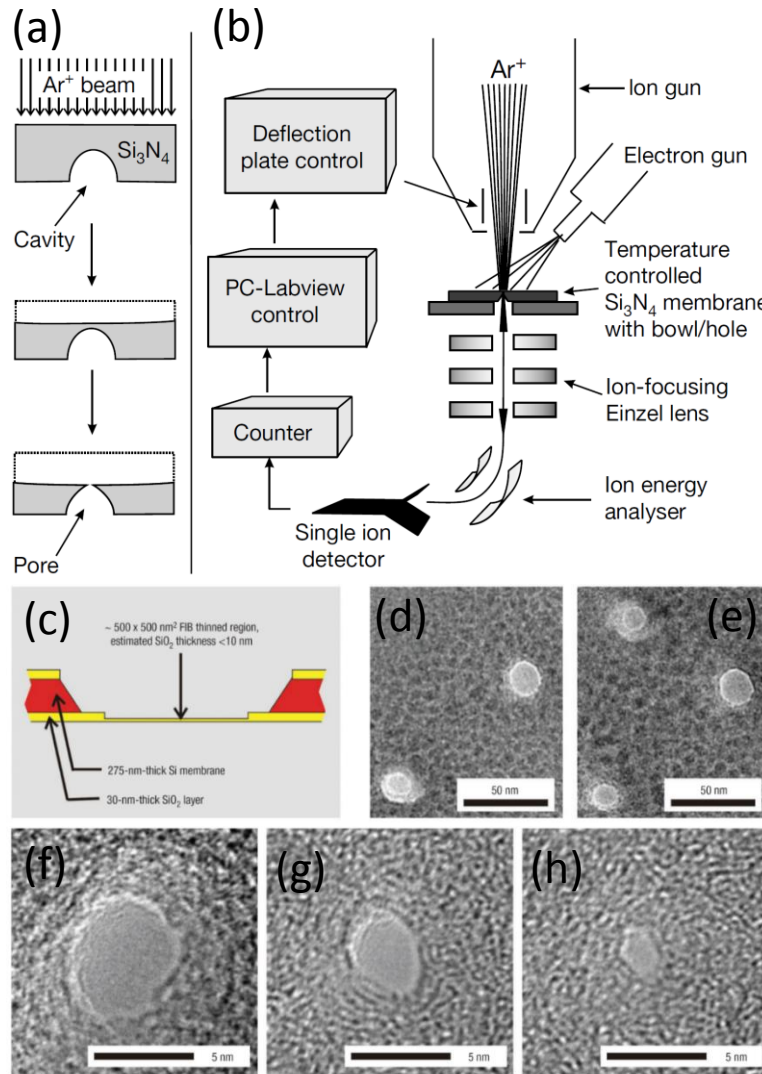


Figure 2.1 Nanopores fabricated using different types of high energy beams. **a)** Schematics of the nanopore formation using ion-beam sculpting method. **b)** Feedback controlled ion-beam sculpting apparatus. **c)** Schematic showing a thin membrane used for TEM milling. **d, e)** TEM images showing milled nanopores. **f-h)** A 6 nm pore is shrunk to 2 nm.

(a) and (b) are reprinted from reference 13, © 2001 Nature Publishing Group. (c) - (h) are reprinted from reference 14, © 2003 Nature Publishing Group.

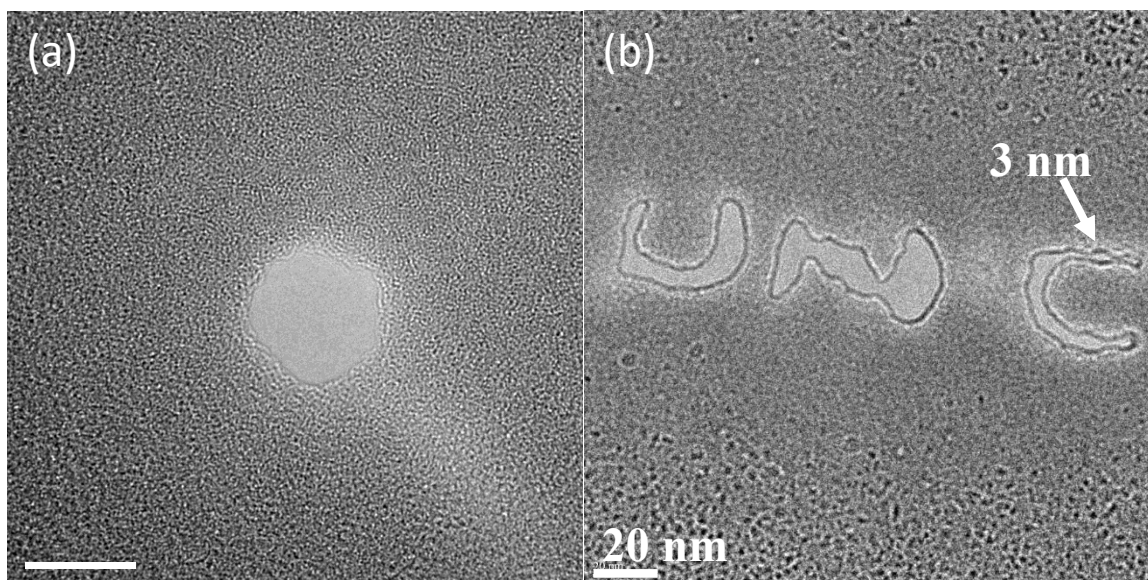


Figure 2.2 Nanostructures milled using a focused electron beam. The JEOL 2010F-FasTEM was operated at 200 keV to mill these features. a) A 12 nm nanopore. b) “UNC” pattern where the smallest dimension is ~3nm.

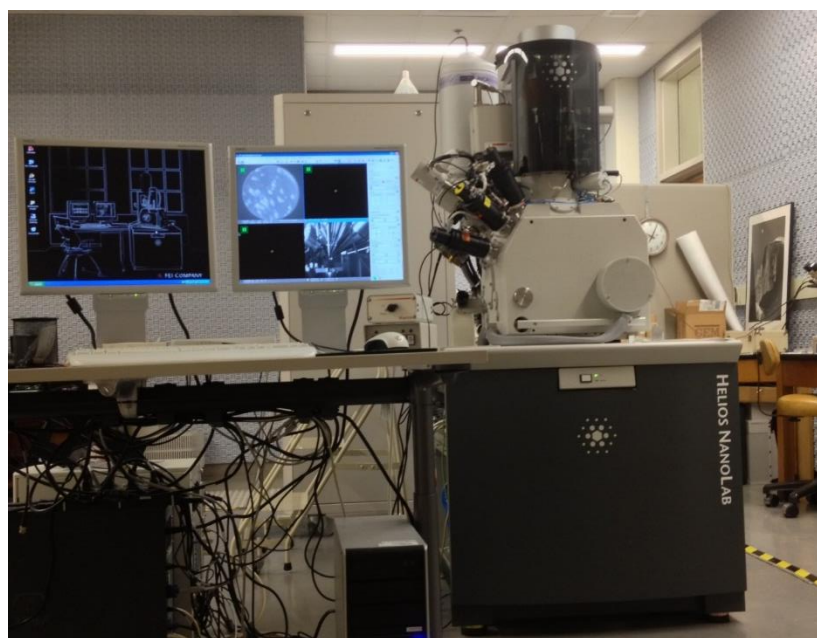


Figure 2.3 A photo of the FEI Helios 600 Nanolab™ DualBeam™ instrument. It is equipped with a high resolution SEM and a FIB.

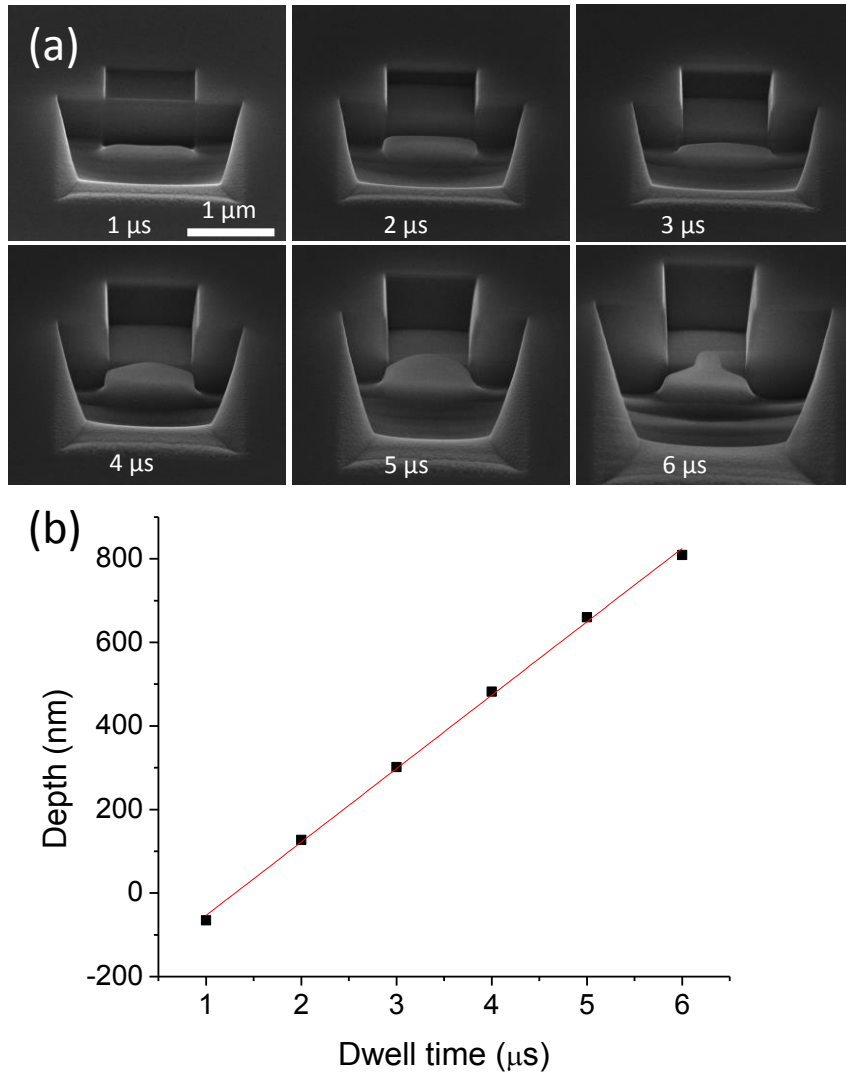


Figure 2.4 Linear relationship between the dwell time and the milled depth. **a)** SEM images of the cross sectioned squares milled with different parameters. **b)** The milled depth as a function of the dwell time. Zero is defined as the interface between the Cr layer and the quartz substrate.

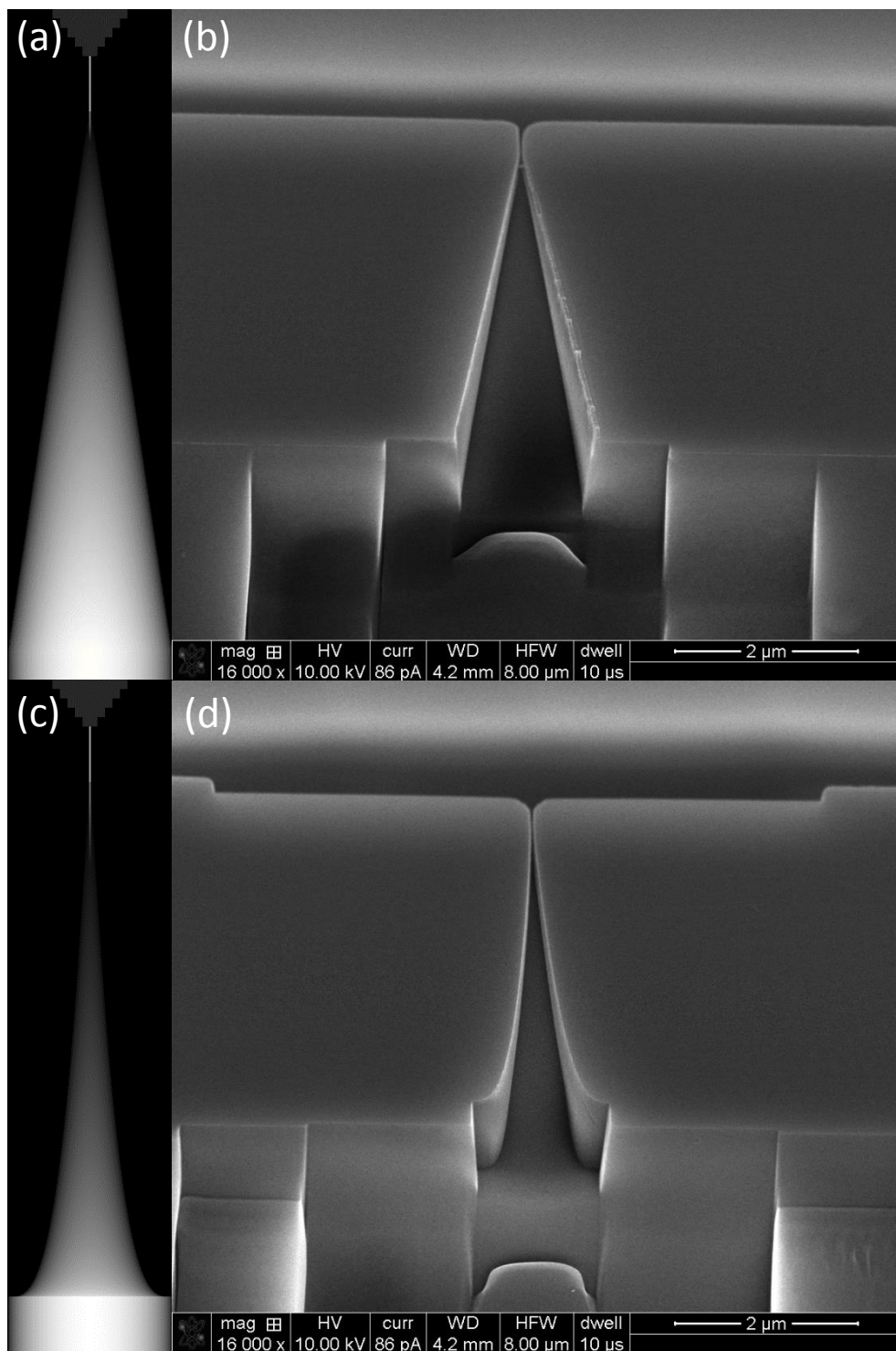


Figure 2.5 Bitmap images and the patterns milled according to these images. **a)** Bitmap image for a triangular funnel with a 500 nm channel. **b)** SEM image of the milled triangular funnel. **c)** Bitmap image for the hyperbolic funnel with a 500 nm channel. **d)** SEM image of the milled hyperbolic funnel.

Table 2.1 Probe size and the milling time required for sputtering a $1\mu\text{m}\times 1\mu\text{m}\times 1\mu\text{m}$ cubic volume at different ion beam currents.

Beam Current	Diameter (nm)	Average Current Density (pA/nm ²)	Milling Time (s)	Passes
1.5 pA	7.0	0.04	4460	53956
9.7 pA	13.0	0.07	691	28756
28 pA	17.0	0.12	369	17564
48 pA	19.0	0.17	144	12843
93 pA	24.0	0.21	84	10489
0.28 nA	31.0	0.37	25	5959
0.46 nA	35.0	0.48	15	4528
0.92 nA	44.0	0.61	8	3617
2.8 nA	66.0	0.82	3	2698
4.7 nA	85.0	0.83	2	2741
6.5 nA	102.0	0.80	1	2869
21 nA	274.0	0.36	0.4	6565

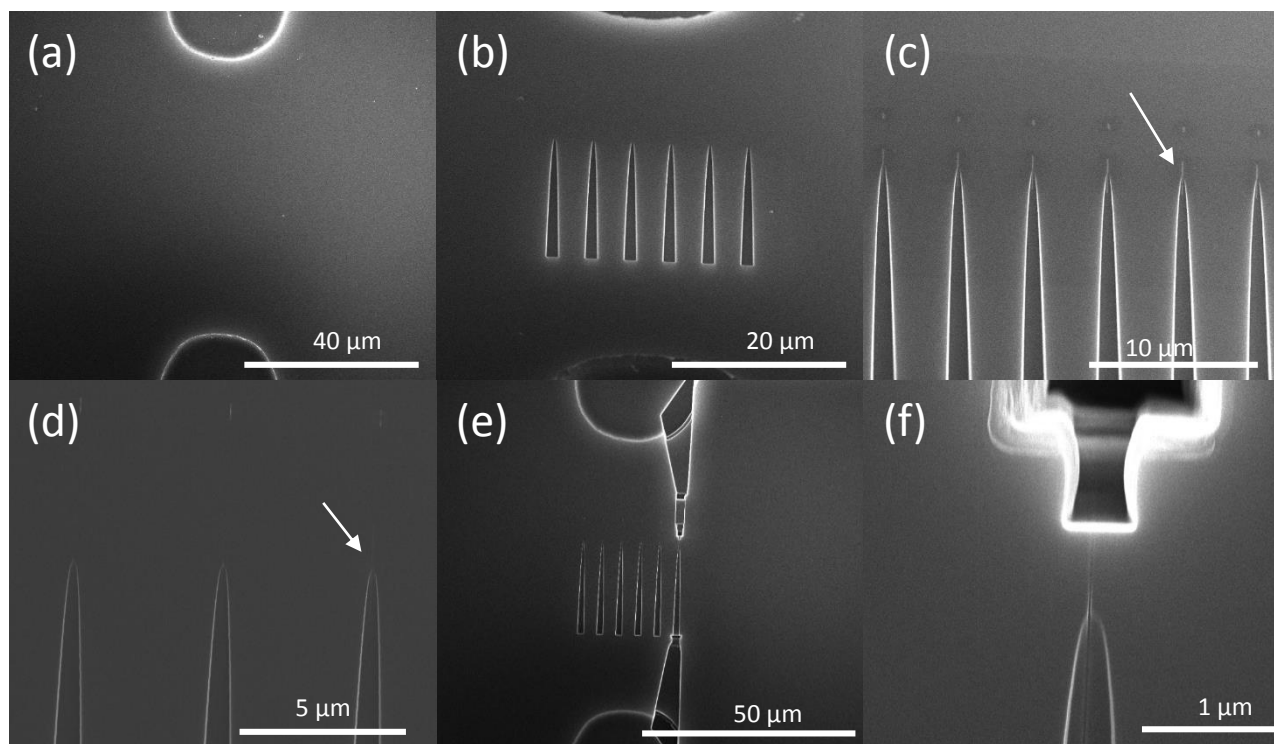


Figure 2.6 SEM images showing the steps of milling a 20 nm wide nanochannel with a three-dimensional nanofunnel. **a)** The gap between the microchannels before milling. **b)** Step 1: mill nanofunnels. **c)** Step 2: mill nanochannels. **d)** SEM images of the nanochannels after removing the Cr layer. Only the rightmost channel was found to be milled into the quartz substrate. **e)** Mill the access to the microchannels. **f)** Higher magnification view of the finished structure.

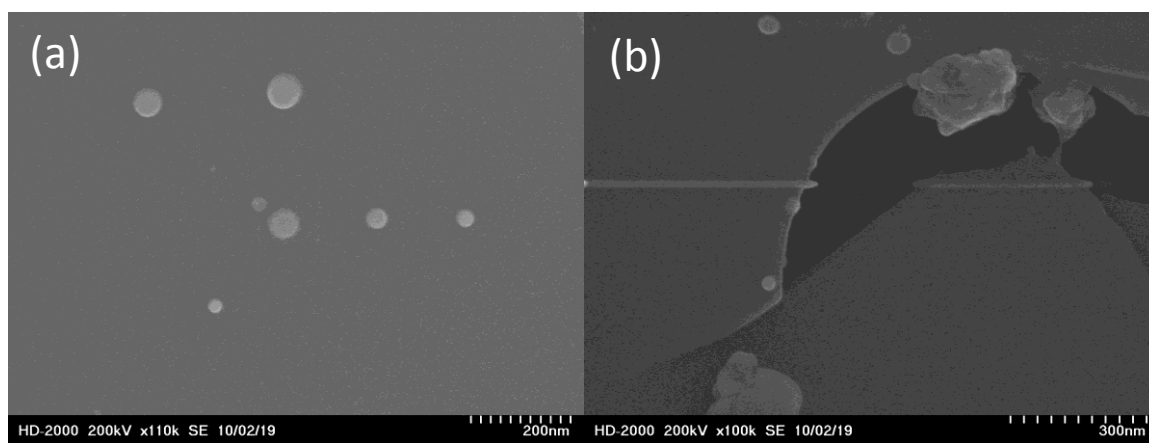


Figure 2.7 Secondary electron images showing the contamination in the STEM. a) Spots created by dwelling the beam on the SiN_x membrane. **b)** Lines created by scanning the electron beam over a fracture in a SiN_x membrane.

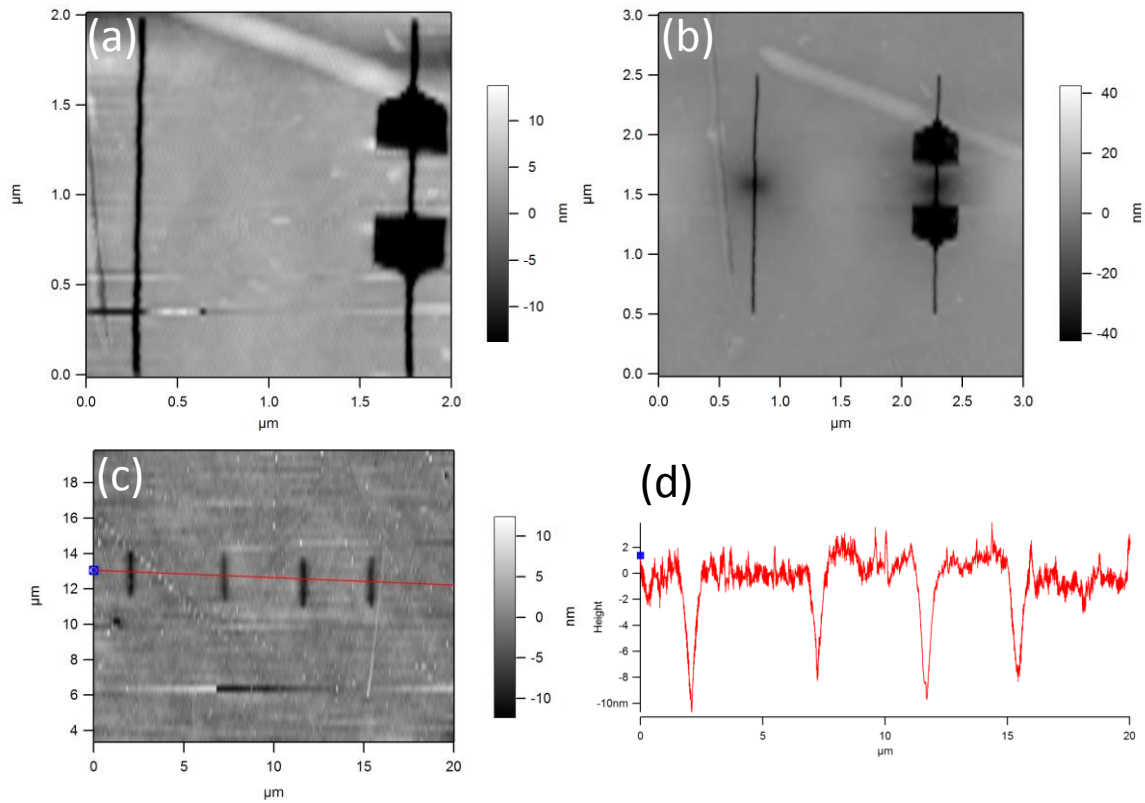


Figure 2.8 Damage induced by a 10 kV electron beam. **a)** AFM image of features milled using FIB. The left one is a nanochannel. The right one is a nanochannel with two cross sectioning cuts. **b)** AFM image of the same area as in (a) after the following processes: 1. Several SEM images were taken at the center of the two features. 2. The Cr film was removed. 3. A new 10 nm Cr film was deposited. **c)** AFM image showing the electron beam induced damage achieved by rastering the beam along a series of lines. The red line shows the path of the depth profile in (d). **d)** Depth profile of the channels in (c).

Chapter 3: Capture of DNA Molecules Using Three-Dimensional Nanofunnel-Nanochannel Devices

Introduction

3.1.1 Background

As discussed in the introductory chapters of this Thesis, nanofluidic devices have been demonstrated as powerful tools for the analysis of single DNA molecules.¹ The nanopores and nanochannels used in these analyses often have diameters that are smaller than the hydrodynamic radius and even the persistence length of analyte macromolecules. As a consequence, insertion of polynucleic acids into the conduits not only localizes the macromolecules, but also linearizes them by threading them through nanopores or extending them within nanochannels.²⁻⁴ Such confinement reduces a polymer's conformational entropy and must therefore be initiated by applying an external force (e.g., hydraulic or electrostatic).^{5,6} The hydraulic resistance of the nanochannels are normally very large. As a result, most of the experiments use electrostatic forces to control molecular transport.⁷

The free energy associated with the capture and subsequent threading of a macromolecule has primarily been studied in the case of voltage-driven translocation of biological macromolecules through nanopores.⁸⁻¹⁵ In these experiments, the translocation of the molecule perturbs the quiescent current, and the event duration, amplitude, and frequency reveal analyte characteristics such as macromolecule length, secondary structure, and concentration.¹⁶ The often abrupt boundary between a nanopore and the reservoirs to which it is interfaced results in steep gradients in the electric field strength, fluid flow velocity, and degree of confinement.^{17,18} As a result, the electric, hydrodynamic, and entropic forces that

the molecule experiences are changing rapidly as the molecule threads into the pore. A detailed understanding of the threading process requires knowledge of the nanopore geometry, the resulting shape and magnitude of the force fields, the dynamics of tension propagation within the polynucleotide, and any interactions between the polynucleotide and the nanopore surfaces.^{15,19,20} Given these parameters, theoretical studies can be correlated to experiments that measure the capture frequency of ss-DNA, ds-DNA, and proteins.⁸⁻¹⁵ When the driving voltage is large or the nanochannels are large, the capture rate of the macromolecules is a linear function of the voltage, indicating the process is mass-transfer, not barrier, limited.¹⁴ At lower voltages, an exponential dependence of the capture rate on voltage is observed, indicating the presence of an entropic barrier controlling the threading process.^{11,12} The existence of such a barrier affects the throughput of a nanofluidic device⁸ and the transport velocity of analytes through nanopores and nanochannels,²¹ which imposes minimum requirements on detector bandwidth.

The accurate metrology of individual nanopores is an important prerequisite to study polymer behavior. Nanopores fabricated using top-down methods in insulating membranes are subject to significant pore-to-pore variability. While precise characterizations are possible using, for example, transmission electron tomography,²² these techniques are not routinely applied. More often the nanopore geometry is inferred from some measured dimensions (e.g., membrane thickness, diameter at maximal constriction) and models based on prior, more rigorous characterizations of nanopores of the same class. Pores fabricated using the track-etch method have a conical shape;²³ ion-beam sculpted pores have a concave shape;²² electron beam milled pores typically have a bi-conical shape.²² Engineered divergence from these method specific geometries is limited. It should be noted that

biological nanopores consisting of self-assembled pore protein complexes that traverse lipid bilayers have precise and reproducible geometries.²⁴ While this is a highly desirable trait for many applications, investigating the role of the engineered geometry of a biological pore is even more limited than in the case of top-down fabricated nanopores.^{25,26}

In contrast to nanopores perforating thin membranes, nanochannels fabricated in the top surface of substrates can be readily imaged using scanning electron microscopy (SEM) and profiled using atomic force microscopy (AFM) to accurately determine their dimensions along their entire lengths.²⁷ Additionally, the fact that the nanochannels are co-planar with the microfluidic channels that access them enables the incorporation of structures, such as post arrays or gradually narrowing channel dimensions,⁶ that mediate macromolecule capture. Polynucleic acids stained with intercalating dyes can be readily imaged using fluorescence microscopy, providing direct tracking of molecular motion and assessment of nanoscale confinement effects.^{28,29}

In this Chapter a study of the capture process with three-dimensional nanofunnels fabricated using FIB milling is described. Precisely defined nanofunnels were seamlessly integrated with long nanochannels, generating nanochannel entrances with any desired geometry. Figure 3.1 a shows the schematic representation of the fluidic device, and Figure 3.1 b shows the schematic of the three-dimensional funnel. The SEM image in Figure 3.1 c shows a nanofunnel-nanochannel structure connecting microfluidic channels at both ends. A set of nanofunnels was investigated and the transport of fluorescently-stained DNA molecules driven electrostatically. By tuning the nanofunnel geometry, it was possible to drive DNA translocations through the nanochannel at voltages lower than those required in

the absence of a nanofunnel. Additionally, direct measurements of the threshold electric field enabled a comparison of the effects of different nanofunnel geometries.

3.1.2 Three-Dimensional Nanofunnel Design

The flexibility afforded by FIB milling means that an almost infinite variety of nanofunnel geometries and sizes can be fabricated. In this Chapter, experiments are described that were conducted on a set of nanofunnels defined by the general equation

$$D(x) = (D_m - D_n) \left(\frac{x}{L_{funnel}} \right)^\alpha + D_n \quad (3.1)$$

where $D(x)$ is the geometric mean of the nanofunnel width, $y(x)$, and depth, $z(x)$, at the coordinate, x , along the funnel's longitudinal axis and L_{funnel} is the length of the nanofunnel.

D_n and D_m are likewise geometric means describing the nanofunnel width and depth at its narrowest point (where it is interfaced to the nanochannel) and widest point (where it is interfaced to the microchannel), respectively. In this work, funnels having approximately square cross-sectional profiles along their entire lengths were fabricated, such that

$D(x) \approx y(x) \approx z(x)$. This differs from previous studies of gradient structures in micro- and nanofluidic devices, where confinement in one dimension is gradually increased.^{6,30} The values for D_n , D_m , and L_{funnel} were kept constant, while comparisons were made between nanofunnels with various values of α ($\alpha=0, 0.5, 1$). These investigations thus placed an emphasis on nanofunnel shape over size variations. D_n was ~ 100 nm, comparable to the Kuhn length of dsDNA. D_m was $1.5 \mu\text{m}$, close to the radius of gyration of λ -phage or T4-phage DNA ($\sim 1.4 \mu\text{m}$ and $\sim 2.9 \mu\text{m}$, respectively). A length of $22 \mu\text{m}$ ensured that a) the funnel was longer than the expected DNA extension length, and b) there was sufficient time to adjust the applied voltage as the molecule was captured by the funnel. Longer funnels may

facilitate the studies described here and in Chapter 4. Funnel length was limited by the fabrication protocol, however, in that the milling time was kept below 10 min to avoid a loss of pattern fidelity associated with sample drift.^{27,31} The parameter α determines how quickly a molecule is constrained in moving from the microchannel into the nanochannel (Figure 3.1 d). A smaller value of α indicates a more dramatic change in diameter at the nanoend, while a larger value of α implies a faster change at the microend. When $\alpha = 0$, the funnel becomes a vestibule with diameter D_m . When $\alpha = \infty$, the funnel is eliminated and the nanochannel (with diameter D_n) interfaces directly with the microchannel.

Figure 3.1 d shows various nanofunnel shapes that were studied. Funnel widths were measured using both SEM and AFM, while depths were profiled using AFM. Because the aim of these studies was to better understand the role of nanofunnel geometry on polymer behavior, dimensions were selected that were conducive to accurate metrology. While smaller features ($D_n < 10$ nm) can be fabricated using FIB milling, a minimum dimension of 100 nm ensured complete access of the AFM probe to the bottom of the nanofunnels and nanochannels.^{27,32} Representative depth and width profiles are shown in Figure 3.1 e to illustrate the three-dimensional nature of the FIB milled nanofunnels. Other fabrication techniques relying on lithography followed by substrate etching can produce nanofunnels with varying width and a constant depth (equivalent to the nanochannel depth if a single lithography and etching cycle is implemented).^{33,34} While polymer dynamics will be affected by these structures, the introduction of DNA molecules to the nanochannel will be dominated by partitioning from the microfluidic channel to the nanofunnel. Gradually increasing the confinement of DNA molecules in both width and depth, in contrast, enables more precise control of the process.

3.2 Materials and Methods

3.2.1 Device fabrication

A focused ion beam was used to mill the nanochannel and the funnel, a process discussed in Chapter 2. A schematic representation of the nanofluidic devices fabrication process is shown in Figure 3.2. Microfluidic channels were patterned in fused silica substrates (Telic Co.) using standard photolithography and wet etching in a 5:1 buffered oxide etch solution (a solution of ammonium fluoride and hydrofluoric acid, Transene Company, Inc.) for about 30 minutes at room temperature. Typical dimensions were 20 μm wide and 3 μm deep, with an 80 – 90 μm gap between independent microchannels. Vias accessing the microfluidic channels were drilled from the substrate backside using abrasive powder blasting (MicroBlaster, COMCO, Inc). The substrate as received from the supplier was coated with a 130-nm thick chromium film, through which the nanofunnel and nanochannel were milled into the underlying substrate using a FIB instrument operated at 30 keV with a 0.46 nA beam current (Helios NanoLab DualBeam, FEI Company).

Following FIB milling, the 130-nm thick chromium film was removed using a chemical etchant (Transene Company, Inc.) and a new 10-nm chromium film was deposited using ion beam sputtering (Model IBS/e, South Bay Technologies, Inc.). The purpose of this second film was to dissipate charge and protect the surface during subsequent SEM and AFM imaging. The nanofunnel and nanochannel were imaged using SEM and AFM with a high aspect ratio probe (ACCESS-NC probe, Applied NanoStructures, Inc.). After imaging, the chromium film was chemically etched, the substrate cleaned by immersion in Nanostrip 2X (Cyantek Corporation), and the top surface bonded to a clean fused silica coverslip.

Permanent fusion bonding was achieved by heating the bonded substrate in a furnace to 1000 °C for 50 hours.

After bonding, reservoirs were affixed over the powder blasted vias with a UV-curable epoxy to facilitate the introduction of solutions to the fluidic network. The channels were filled with 2X TBE (Tris-borate-EDTA) buffer prepared from a 10X TBE stock solution (Fisher Scientific) and the ionic conductance was measured using an Axopatch 200B patch clamp amplifier (Molecular Devices) between all possible reservoir pairs. The measured values were compared to those expected from the microchannel, nanochannel, and nanofunnel geometries and dimensions in order to confirm that all channels were wetted and clear of obstructions.

3.2.2 Measurement of Translocation Event Frequency

A schematic representation of the event frequency experiment is shown in Figure 3.3. Lambda-phage DNA (48.5 kbp, Promega Corporation) in 2X TBE was stained with the intercalating dye YOYO-1 (Invitrogen) at a base-pair:dye ratio of 5:1.²⁸ Solutions containing 5 ng/μL of λ-phage DNA also contained 4% (by volume) β-mercaptoethanol (Fisher Scientific) to limit photoinduced fragmentation and 2% (by mass) polyvinylpyrrolidone (PVP, 10 kDa, Sigma-Aldrich) to suppress electro-osmotic flow (EOF) within the channels.^{35,36} The device was mounted on an inverted fluorescence microscope (Eclipse TE2000-U, Nikon) and imaged through a 100x/1.4 NA oil immersion objective (Nikon) while λ-phage DNA molecules were being electrophoretically driven through the nanochannel. Fluorescence was excited using a 100-W mercury arc lamp filtered through a GFP-3035 filter set (excitation at 472 nm, emission at 520 nm, Semrock) and images were recorded using a Cascade II EM-CCD camera (Photometrics) at 10 frames per second.

These images were analyzed using an automated image analysis program written in Matlab to count the number of translocated DNA molecules and determine the interval between events.

The applied voltage ranged from 0.3 to 5 V, corresponding to an electric field strength within the nanochannel of 45 – 750 V/cm. In order to compare the event frequency in the presence or absence of a nanofunnel, experiments were conducted in which the DNA molecules were introduced from either the funnel side or the channel side (Figure 3.3). More than 100 molecules were typically analyzed for each voltage. Fewer molecules were analyzed from experiments driving transport from the channel side using voltages below 1 V (150 V/cm). Because the translocation frequency at these voltages was reduced by the entropic barrier, long-term operation resulted in the accumulation of DNA near the nanochannel entrance, which will be discussed in more detail later. To reduce effects from DNA concentration or molecular crowding, data were collected for 10 minutes, followed by 2 minutes during which the voltage was raised to 2 V to clear the accumulated DNA through the nanochannel. The voltage was then returned to the lower voltage and additional data collected until the transport of at least 20 molecules was recorded.

3.2.3 Determining the Threshold Voltage

The schematic representation of the threshold voltage experiment is shown in Figure 3.4. Experiments were conducted to characterize the minimum voltage required to initiate DNA transport through the nanochannel on devices with various nanofunnel geometries. Dilute (0.25 ng/ μ L) solutions of λ -phage or T4-phage (165.6 kbp, Nippon Gene Co.) DNA in 2X TBE buffer were used in order to reduce the possibility of two molecules simultaneously occupying the nanofunnel. The effect of the dynamic coating, PVP, was investigated by

conducting experiments with 2X TBE that contained no PVP or 2% PVP by mass. A small voltage was applied to introduce a DNA molecule to the nanofunnel and hold it near the nanochannel entrance. Because the molecule was effectively trapped at the nanochannel entrance, it could make multiple attempts at translocation. If after 5 minutes the molecule did not translocate through the nanochannel, the voltage was increased by increments of 10 mV ($\alpha=0.5$, 1) or 100 mV ($\alpha=0$). This process was repeated until the molecule successfully translocated through the nanochannel. The threshold voltage was verified by measuring multiple molecules or interrogating the same molecule multiple times.

3.3 Results and Discussion

In moving from a microchannel to a nanochannel, the molecule experiences the same amount of entropy change regardless of whether a funnel is present.⁶ However, the funnel affects the path of the entropy change, as well as the electric field along the path, which is capable of overcoming the entropy change. A qualitative picture of the free energy landscape near the threshold voltage with or without a funnel is shown in Figure 3.5. When the same voltages are applied, the presence of the funnel decreases the energy barrier for the molecule to enter the nanochannel.

Similar to studies performed using biological or solid-state nanopores, this entropic barrier was characterized by measuring the frequency of translocations through the nanochannel as a function of voltage.⁸⁻¹⁵ To assess the effect of a nanofunnel, translocations were measured using a nanochannel (width = 96 nm, depth = 141 nm) having one end that interfaced directly with a microchannel while its opposite end was interfaced to a nanofunnel ($\alpha=0.5$). Translocation frequencies were then measured for DNA molecules that were electrophoretically driven from each of the nanochannel's ends. For a given applied voltage,

the magnitude of the electric field in the nanochannel was therefore identical, irrespective of the voltage polarity. It should be noted that throughout this chapter, comparisons of voltage dependent polymer behavior are made on the basis of the electric field strength in the nanochannel, E , accounting for variation in nanochannel length across devices.

The results of these experiments are shown in Figure 3.6. In the case of DNA translocations driven from the end lacking a nanofunnel, an exponential increase in event frequency was observed with an increase in electric field strength at low voltages. At higher voltages, the event frequency increased linearly with the electric field strength. Not surprisingly, this behavior is identical to that observed for translocations through nanopores.¹¹ At low voltages the translocation frequency is dominated by the kinetics of barrier crossing, while at high voltages the electrostatic force exceeds the entropic barrier and event frequency is limited by the rate at which DNA molecules approach the nanochannel entrance.⁸ In the region of exponential response ($E < 225$ V/cm) the data can be analyzed using a van't Hoff-Arrhenius formulism.^{10,11} The translocation frequency, f , is fit to the equation

$$f = f_0 \exp\left(\frac{E}{E_0}\right) \quad (3.2)$$

where E_0 is the threshold field strength required to drive translocation, $f_0 = (1.1 \pm 0.7) \times 10^{-3}$ min⁻¹, $E_0 = 41 \pm 6$ V/cm.

When DNA molecules are driven in the opposite direction (i.e., from the funnel side), no exponential dependence of event frequency on voltage is observed. Although the total entropy change is the same, the nanofunnel can lower the threshold field strength required for translocation by optimally balancing the voltage reduction to the entropic barrier as the

molecule deforms from its bulk to extended conformation. Gradient structures have previously been shown to facilitate DNA introduction into nanochannels.⁶ These devices consist of pillar arrays and/or microchannels with gradually decreasing depths that feed into nanochannel arrays. While practical and easily fabricated, such architectures do not lend themselves to a precise characterization of the electrostatic, hydrodynamic, and entropic forces. Furthermore, a population of DNA molecules may be influenced by a broad distribution of force profiles given the various paths that molecules can traverse in a pillar array. In contrast, the three-dimensional nanofunnels described here provide a platform in which these forces are well defined and are acting on equilibrated DNA molecules.

While event frequency measurements appear effective for probing the barrier to translocation in the absence of a nanofunnel, there are some considerations that warrant an alternative approach in characterizing the effects of nanofunnels. In the presence of a nanofunnel, the low frequency of translocation events at low electric field strengths precludes the acquisition of enough events to precisely determine the threshold electric field. While event frequency can be increased by a commensurate increase in the DNA concentration, it should be noted that a concentration of 5 ng/ μL (170 pM) corresponds to approximately one λ -phage DNA molecule in 10 μm^3 , a volume comparable to that of the nanofunnels. The presence of multiple DNA molecules in a nanofunnel is therefore possible and is likely to affect the observed translocation frequencies. Such effects are exacerbated when the translocation rate is attenuated by the entropic barrier (i.e., at sufficiently low field strengths). In contrast to nanopores, where the electric field is negligible far from the pore and DNA molecules approach the pore diffusively, in the fluidic devices described here a fraction of the applied voltage is dropped across the microfluidic channels and DNA molecules migrate

toward the nanochannel. This results in the concentration of DNA over time when the rate of migration to the nanochannel exceeds that of translocation through the nanochannel. In the case of translocation in the absence of a funnel, this concentration enhancement in the source microchannel was directly monitored. Figure 3.7 a shows the intensity change in the microchannels over about 2 hours at a nanochannel field strength of 125 V/cm. A 10 μm long microchannel region at the nanochannel entrance was selected to monitor the intensity change, and it was compared with the intensity in the selected microchannel as the background (red dashed rectangles in Figure 3.7 a). The intensity as a function of time is plotted in Figure 3.7 b, and the ratio of the two is plotted in Figure 3.7 c. A roughly linear concentration increase was observed over the first hour as shown in the plot. Because time dependent concentration effects will skew the results of near threshold measurements, an alternative method was utilized to determine the threshold electric fields for various nanofunnel shapes.

Directly measuring the electric field sufficient to drive translocation was enabled by the ability to visualize DNA molecules in the planar nanofluidic devices. Low concentration DNA solutions were used and a single molecule was electrophoretically driven into the nanofunnel. The voltage was lowered to a value below the threshold for translocation that was nevertheless sufficient to prevent diffusion out of the nanofunnel. In this configuration, a single molecule made repeated attempts at translocation as it was electrostatically held near the nanochannel entrance. If the molecule was unable to translocate after approximately 5 minutes then the voltage was increased and sampling continued in a stepwise fashion until translocation was observed. The field strength in the nanochannel at which translocation occurred was taken as the threshold value and the results for a variety of funnels, DNA

lengths, and buffer conditions are presented in Figure 3.8. This method slightly overestimates the threshold electric field because barrier crossing is a probabilistic event and the result of such a binary experiment is dependent on the sampling time. This error is expected to be small, however, because of the rapid and repeated collisions of the molecule with the nanochannel entrance. This was verified by comparing the result obtained using the direct measurement for the nanochannel with an $\alpha=0$ nanofunnel to that derived from a van't Hoff-Arrhenius fit to the data collected from the nanochannel without a funnel (Figure 3.6). In both cases, the DNA molecule abruptly transitions from its bulk to confined conformation. Pulling λ -phage DNA into a nanochannel through an $\alpha=0$ nanofunnel in a 2X TBE (2% PVP) solution required a threshold electric field of 64 ± 7 V/cm. This is close to the result obtained from fitting the data in Figure 3.6 (41 ± 6 V/cm) when a correction is made for the slight difference in nanochannel diameters: $D_n (\alpha=0) = 99$ nm, D_n (no funnel) = 115 nm. Using a correction factor derived from the de Gennes theory of confinement, $\left(\frac{115 \text{ nm}}{99 \text{ nm}}\right)^{5/3}$, the adjusted threshold electric field from the nanochannel without a funnel is 53 ± 7 V/cm.³³ Figure 3.8 shows a trend of decreasing threshold electric field with increasing values of α over the range investigated, as expected from theory and simulations.³⁷ This funnel-mediated threshold lowering results from the application of a larger electrostatic force on the DNA molecule, an increased frequency of collisions with the nanochannel entrance, and an increased percentage of such collisions that occur with a DNA conformation that is readily pulled into the nanochannel.

3.4 Conclusion

A free energy barrier exists when a large DNA molecule is driven toward a nanochannel in a low strength electric field. The presence of a three-dimensional nanofunnel

decreases this barrier by changing the profile of the opposing entropic and the electrostatic forces. Two classes of experiments were performed to demonstrate the function of a nanofunnel. The event frequency experiment qualitatively shows the energy barrier is decreased by the funnel. A more quantitative threshold experiment takes advantage of the ability to stably trap a molecule within the funnel. The results of this experiment differentiate the effects of various funnel shapes. Overall, the design of the three-dimensional funnel enables DNA translocation through a nanochannel at lower electric field strengths.

3.5 REFERENCES

1. Abgrall, P. & Nguyen, N. T. Nanofluidic devices and their applications. *Anal. Chem.* **80**, 2326 (2008).
2. Muthukumar, M. Mechanism of DNA Transport Through Pores. *Transport* (2007). doi:10.1146/annurev.biophys.36.040306.132622
3. Levy, S. L. & Craighead, H. G. DNA manipulation, sorting, and mapping in nanofluidic systems. *Chem. Soc. Rev.* **39**, 1133 (2010).
4. Reisner, W., Pedersen, J. N. & Austin, R. H. DNA confinement in nanochannels: physics and biological applications. *Rep. Prog. Phys.* **75**, 106601 (2012).
5. Larson, J. W. *et al.* Single DNA molecule stretching in sudden mixed shear and elongational microflows. *Lab Chip* **6**, 1187–99 (2006).
6. Cao, H., Tegenfeldt, J. O., Austin, R. H. & Chou, S. Y. Gradient nanostructures for interfacing microfluidics and nanofluidics. *Appl. Phys. Lett.* **81**, 3058 (2002).
7. Sparreboom, W., van den Berg, A. & Eijkel, J. C. T. Principles and applications of nanofluidic transport. *Nat. Nanotechnol.* **4**, 713 (2009).
8. Wanunu, M., Morrison, W., Rabin, Y., Grosberg, A. Y. & Meller, A. Electrostatic focusing of unlabelled DNA into nanoscale pores using a salt gradient. *Nat. Nanotechnol.* **5**, 160–5 (2010).
9. Gershow, M. & Golovchenko, J. a. Recapturing and trapping single molecules with a solid-state nanopore. *Nat. Nanotechnol.* **2**, 775 (2007).
10. Cressiot, B. *et al.* Protein transport through a narrow solid-state nanopore at high voltage: experiments and theory. *ACS nano* **6**, 6236–43 (2012).
11. Henrickson, S. E., Misakian, M., Robertson, B. & Kasianowicz, J. J. Driven DNA transport into an asymmetric nanometer-scale pore. *Phys. Rev. Lett.* **85**, 3057–60 (2000).
12. Meller, A. & Branton, D. Single molecule measurements of DNA transport through a nanopore. *Electrophoresis* **23**, 2583–91 (2002).
13. Meller, A. Dynamics of polynucleotide transport through nanometre-scale pores. *J. Phys.: Condens. Matter* **15**, R581–607 (2003).
14. Chen, P. *et al.* Probing Single DNA Molecule Transport Using Fabricated Nanopores. *Nano Lett.* **4**, 2293–2298 (2004).

15. Muthukumar, M. Theory of capture rate in polymer translocation. *The Journal of chemical physics* **132**, 195101 (2010).
16. Kasianowicz, J. J., Brandin, E., Branton, D. & Deamer, D. W. Characterization of individual polynucleotide molecules using a membrane channel. *Proc. Natl. Acad. Sci. USA* **93**, 13770 (1996).
17. Randall, G. C., Schultz, K. M. & Doyle, P. S. Methods to electrophoretically stretch DNA: microcontractions, gels, and hybrid gel-microcontraction devices. *Lab on a chip* **6**, 516–25 (2006).
18. Mannion, J. T., Reccius, C. H., Cross, J. D. & Craighead, H. G. Conformational analysis of single DNA molecules undergoing entropically induced motion in nanochannels. *Biophys. J.* **90**, 4538 (2006).
19. Kumar, R. & Muthukumar, M. Origin of translocation barriers for polyelectrolyte chains. *J. Chem. Phys.* **131**, 194903 (2009).
20. Wong, C. T. A. & Muthukumar, M. Polymer capture by electro-osmotic flow of oppositely charged nanopores. *J. Chem. Phys.* **126**, 164903 (2007).
21. Lu, B., Albertorio, F., Hoogerheide, D. P. & Golovchenko, J. a. Origins and Consequences of Velocity Fluctuations during DNA Passage through a Nanopore. *Biophysical journal* **101**, 70–9 (2011).
22. Kim, M. J., McNally, B., Murata, K. & Meller, A. Characteristics of solid-state nanometre pores fabricated using a transmission electron microscope. *Nanotechnology* **18**, 205302 (2007).
23. Siwy, Z. S. & Fuliński, A. Fabrication of a synthetic nanopore ion pump. *Phys. Rev. Lett.* **89**, 198103 (2002).
24. Song, L. *et al.* Structure of staphylococcal alpha-hemolysin, a heptameric transmembrane pore. *Science* **274**, 1859 (1996).
25. Healy, K. Nanopore-based single-molecule DNA analysis. *NANOMEDICINE-UK* **2**, 459 (2007).
26. Wong, C. T. A. & Muthukumar, M. Polymer translocation through alpha-hemolysin pore with tunable polymer-pore electrostatic interaction. *The Journal of chemical physics* **133**, 045101 (2010).
27. Menard, L. D. & Ramsey, J. M. Fabrication of sub-5 nm nanochannels in insulating substrates using focused ion beam milling. *Nano Lett.* **11**, 512 (2011).

28. Glazer, A. N. & Rye, H. S. Stable dye-DNA intercalation complexes as reagents for high-sensitivity fluorescence detection. *Nature* **359**, 859 (1992).
29. Murade, C. U., Subramaniam, V., Otto, C. & Bennink, M. L. Force spectroscopy and fluorescence microscopy of dsDNA-YOYO-1 complexes: implications for the structure of dsDNA in the overstretching region. *Nucleic. Acids. Res.* **38**, 3423 (2010).
30. Perry, J. M., Zhou, K., Harms, Z. D. & Jacobson, S. C. Ion transport in nanofluidic funnels. *ACS nano* **4**, 3897 (2010).
31. Gierak, J. Focused ion beam technology and ultimate applications. *Semicond. Sci. Tech.* **24**, 043001 (2009).
32. Information of ACCESS (TM) AFM probes. at
<<http://www.appnano.com/products/silicon/access/>>
33. Persson, F., Utko, P., Reisner, W. W., Larsen, N. B. & Kristensen, A. Confinement spectroscopy: probing single DNA molecules with tapered nanochannels. *Nano Lett.* **9**, 1382 (2009).
34. Perry, J. M., Harms, Z. D. & Jacobson, S. C. 3D nanofluidic channels shaped by electron-beam-induced etching. *Small* **8**, 1521 (2012).
35. Milanova, D., Chambers, R. D., Bahga, S. S. & Santiago, J. G. Effect of PVP on the electroosmotic mobility of wet-etched glass microchannels. *Electrophoresis* **33**, 3259 (2012).
36. Kaneta, T., Ueda, T., Hata, K. & Imasaka, T. Suppression of electroosmotic flow and its application to determination of electrophoretic mobilities in a poly(vinylpyrrolidone)-coated capillary. *J. Chromatogr. A* **1106**, 52 (2006).
37. Wang, Y., Panyukov, S. & Rubinstein, M. Unpublished results. (2013).

3.6 Figures

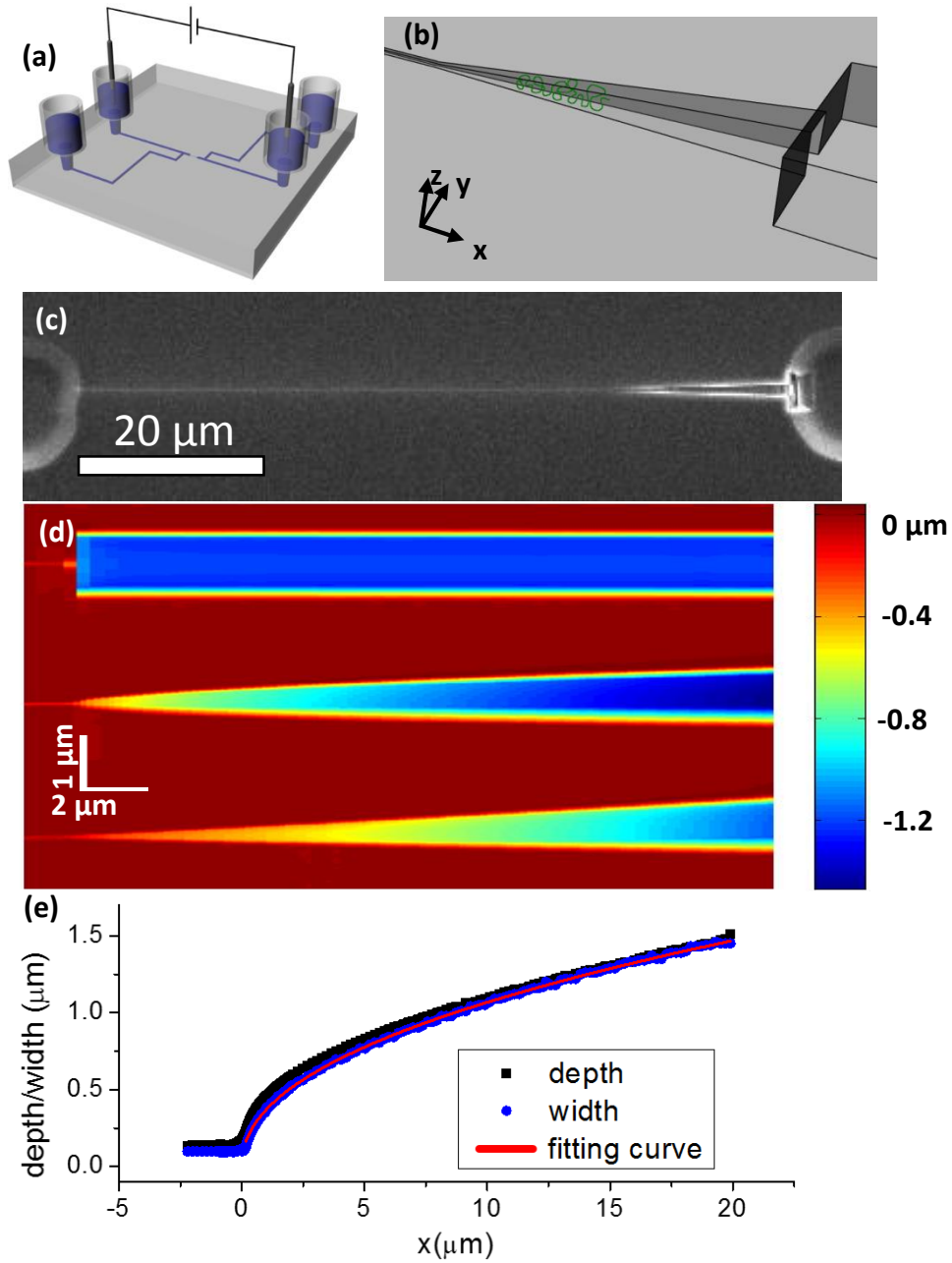


Figure 3.1 The experiment and the three dimensional nanofunnel designs. **a)** Schematic representation of the device and the microchannel patterns. **b)** Schematic representation of the funnel. **c)** SEM image of two microchannels connected by a nanochannel-nanofunnel **d)** AFM images for funnels with different α . **e)** The depth and the width profile of an $\alpha = 0.5$ funnel. The fit to the measured width profile gives a value of $\alpha = 0.46$.

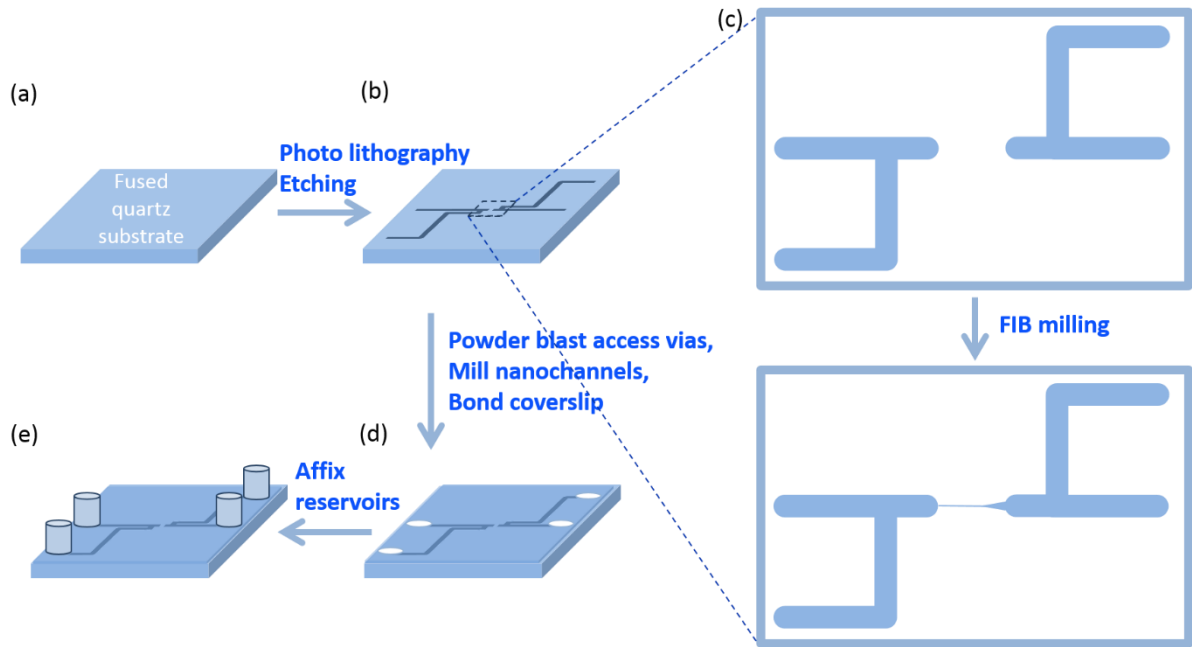


Figure 3.2 Schematic representation of the nanofluidic device fabrication. **a)** A fused quartz substrate with a Cr masking film is used. **b)** Microchannels are patterned into the substrate using photolithography and wet etching. **c)** The nanochannels are milled using FIB to connect the microchannels. **d)** After powder blasting access holes and milling the nanochannels, the substrate is bonded with a quartz coverslip to form the enclosed nanofluidic channels. **e)** After bonding, reservoirs are affixed onto the chip.

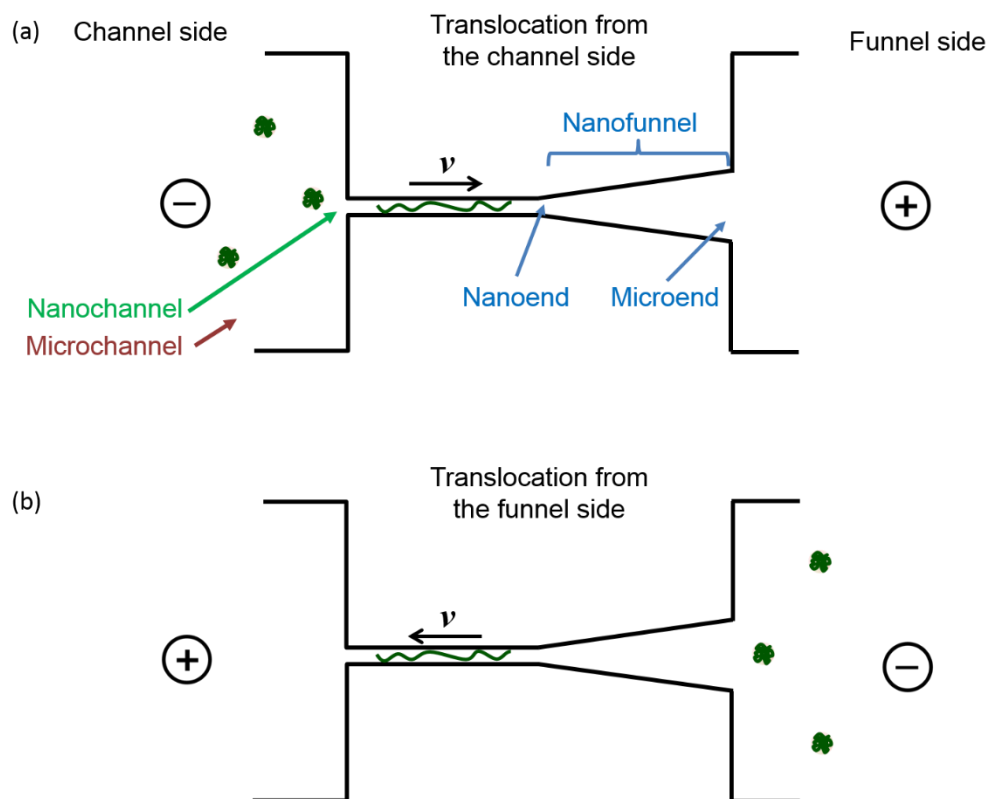


Figure 3.3 Schematic representation of the capture frequency measurements. DNA molecules are captured by the nanochannel either from the channel side or the funnel side. The function of the funnel is studied by comparing the two results **a)** DNA molecules are captured from the channel side. **b)** DNA molecules are captured from the funnel side. The voltage is reversed to serve this purpose.

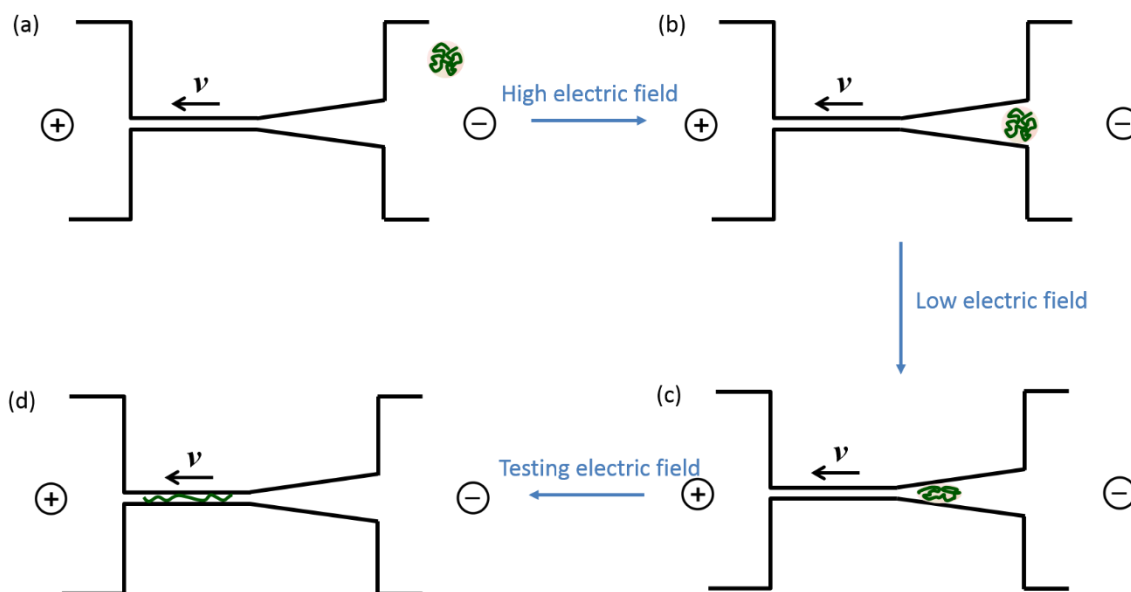


Figure 3.4 Schematic representation of the threshold electric field measurements. **a)** A lower concentration is used compared to the capture frequency measurements. **b)** A high voltage is used to drive the molecule into the funnel through the microend. **c)** After the molecule is in the funnel, the voltage is decreased to avoid translocation of the molecule. The molecule is then delivered to the nanoend of the funnel and the voltage is adjusted to the testing voltage. **d)** The voltage is kept constant to see whether the molecule can translocate within 5 minutes.

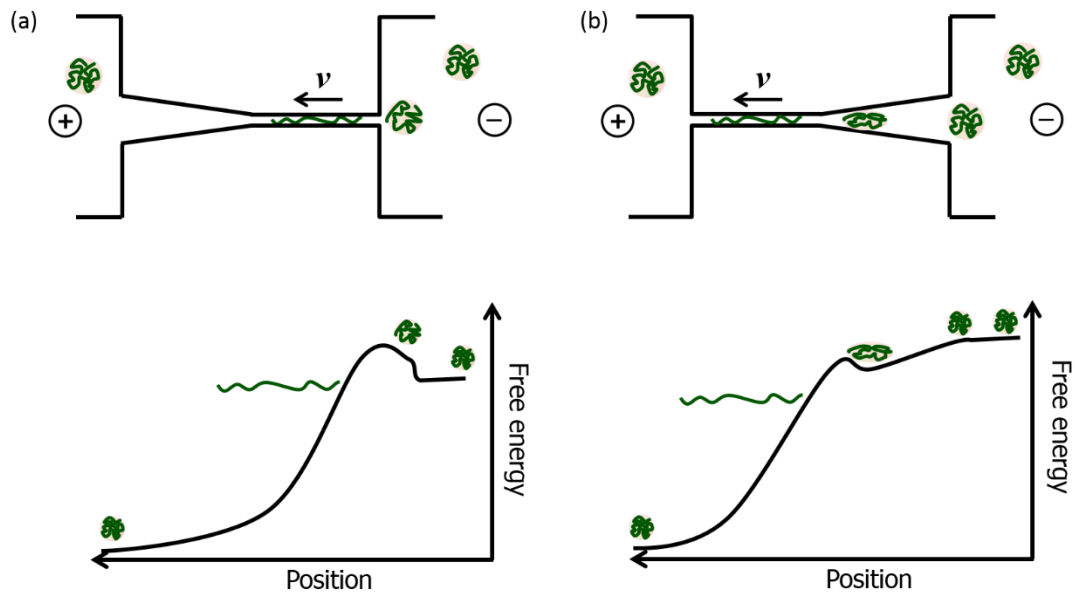


Figure 3.5 Qualitative picture of the free energy landscape of the DNA translocation without or with a funnel. The voltage is close to the threshold for both cases. **a)** without a funnel. **b)** with a funnel.

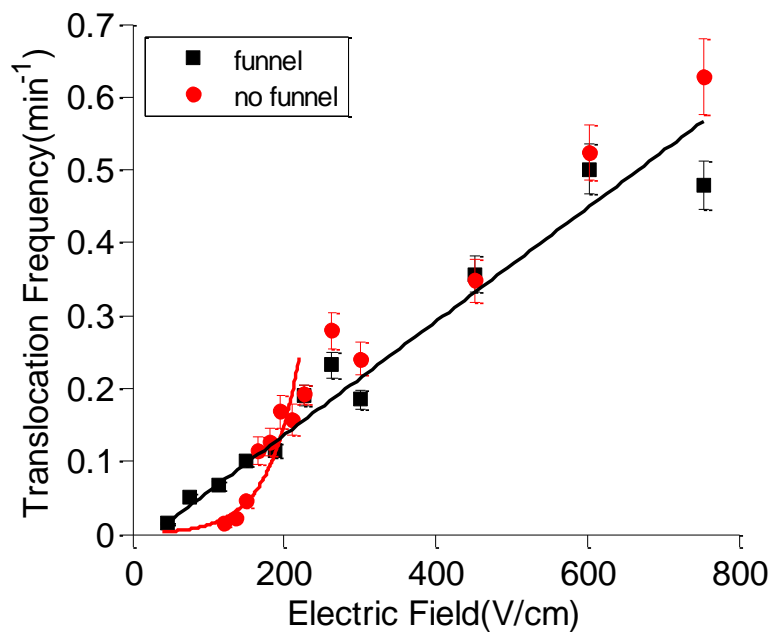


Figure 3.6 Translocation frequency results showing that a nanofunnel decreases the energy barrier for DNA threading. The black solid line is the fit to the data representing translocations from the funnel side. The red solid line is the fit to the data collected at low field strengths characterizing translocation frequency from the channel side.

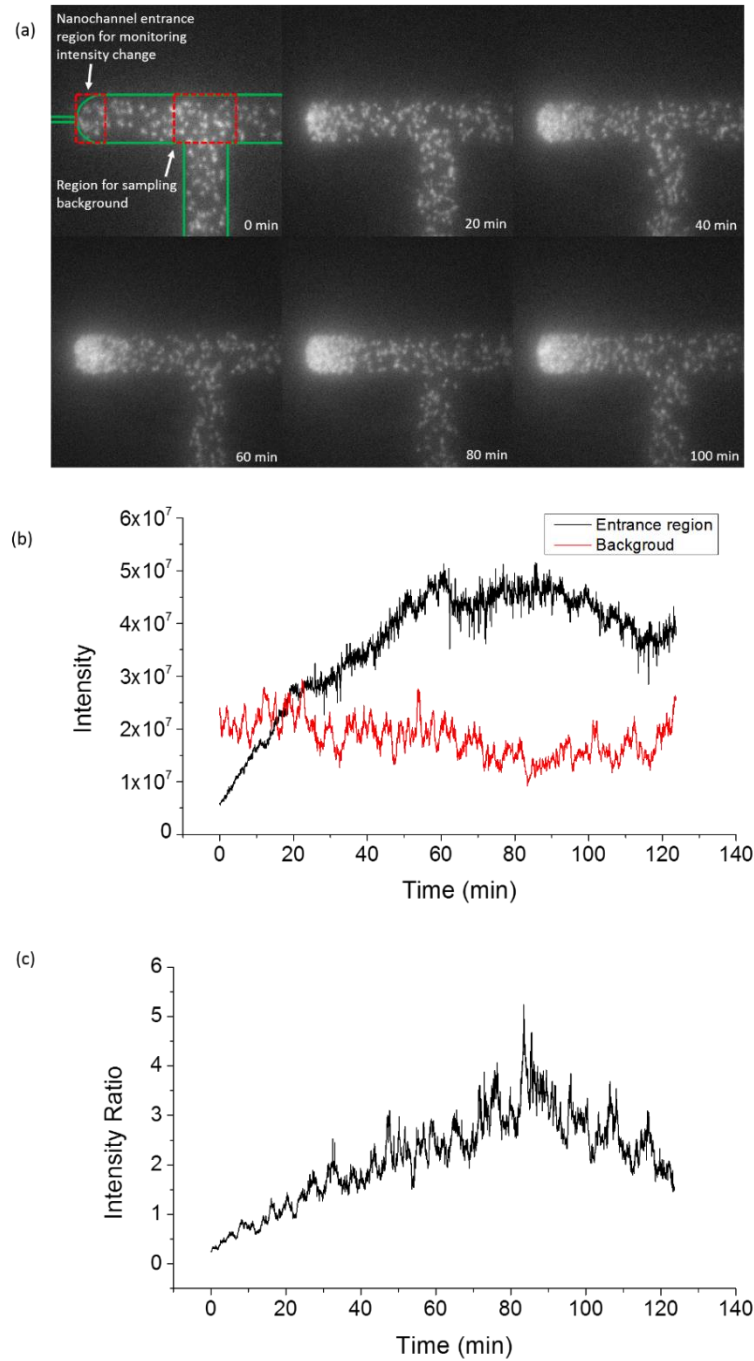


Figure 3.7 Effect of DNA accumulation when the energy barrier for translocation is significant. a) Fluorescence images showing the DNA concentration change as a function of time. **b)** Intensity change in the nanochannel entrance and background region as a function of time. **d)** The ratio of the two region as a function of time showing a roughly linear concentration increase over the first hour.

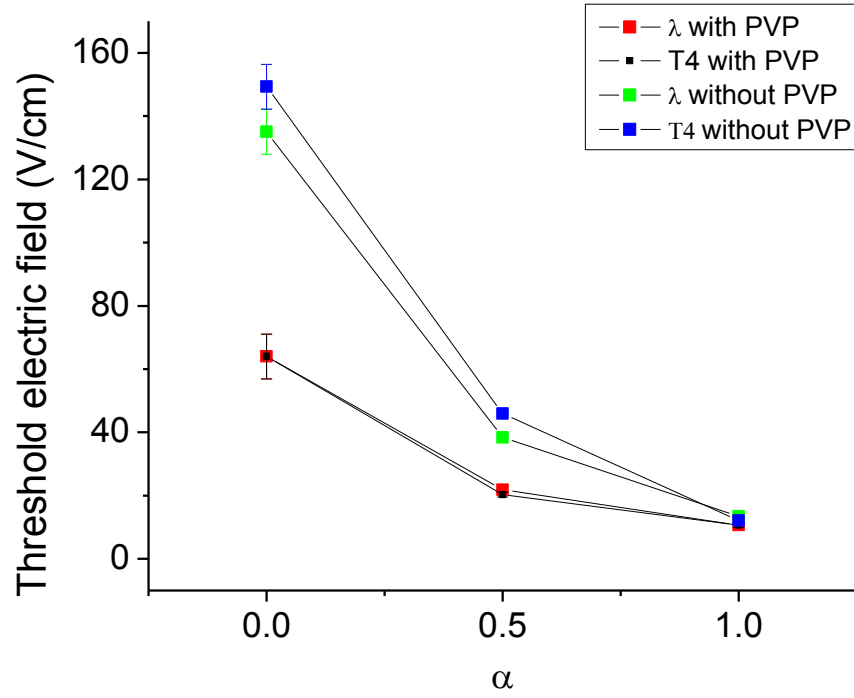


Figure 3.8 Threshold electric field as a function of α . See text for details.

Chapter 4: Trapping Single DNA Molecules in a Three-Dimensional

NanofunnelIntroduction

In the previous Chapter, a three-dimensional nanofunnel was used to facilitate the capture of DNA molecules by a nanochannel. This capability was enabled by the manipulation of molecular conformations through physical confinement and externally applied forces, the magnitude of which were controlled by the shape and dimensions of nanofluidic elements. These forces were therefore qualitatively different from those applied by other systems used for DNA single-molecule force measurements.

In the simplest case of a DNA molecule diffusing in free solution, the molecule acts as a random coil to maximize its conformational entropy. As the molecule diffuses, the solvent surrounding the polymer strands is dragged and moves along with the molecule. These hydrodynamic interactions are included in the Zimm model of chain conformational dynamics, which correctly models the Brownian motion and mean conformation of the chain.¹ When an electric field is applied to the DNA molecule in free solution, the counterions move counter to the direction of DNA migration. The shear resulting from ion motion is restricted to the Debye layer. Hydrodynamic interactions do not couple between units of the polymer outside this limited length scale and the DNA is referred to as “free draining”. One consequence of this behavior is that the electric force and the drag on the molecule both change linearly with the contour length of the molecule (See Section 1.2.2).

The above describes the behavior of a DNA molecule in its randomly coiled conformation. Its mean conformation can be perturbed, however, by the application of a

compressive or extensional force. Various techniques have been developed to manipulate individual DNA molecules in this fashion and measure the forces inherent to the process. DNA molecules can be affixed to atomic force microscopy probes² or to beads that can be manipulated using optical trapping techniques (optical tweezers).^{3,4} In this latter case, a single molecule is attached to a micron-sized dielectric bead, which is placed in an optical trap generated by focusing a laser beam. When the bead moves, the force changes linearly as a function of displacement, so the optical trap acts like a Hookean spring with the spring constant tuned to the beam intensity.

Perkins et al. used an optical trap to immobilize one end of a DNA molecule, while the free end of the molecule was extended using the flow of solution past the DNA.⁶ The equilibrium extension length is determined by a balance between the drag forces and the entropic forces that favor the molecule's recoil. By fitting the observed extension length as a function of flow velocity, the authors determined that the DNA was not free draining in this system. In other words hydrodynamic interactions between polymer segments is significant, even when the chain was stretched to 80% of its full contour length. A stretched conformation of a DNA molecule can also be realized using an electric field. In a theoretical treatment of this scenario, Long et al. determined that an immobilized DNA molecule should behave like an immobile microgel, in that counterion migration would induce fluid pumping through the molecule.⁷⁻¹⁰ The hydrodynamic forces on the monomers were therefore coupled and the authors proposed an equation describing the relation between the stall force and the electro-hydrodynamic force:

$$F_{stall} - \xi(v - \mu E) = 0 \quad (4.1)$$

where the F_{stall} is the external force holding the molecule, ζ is the friction coefficient, v is the velocity of the fluid flow, μ is the mobility of the DNA molecule in free solution, and E is the electric field. In the low force limit the flow velocity is close to zero and the molecule is not deformed:

$$F_{stall} = \eta R_g \mu E \quad (4.2)$$

where η is the viscosity, and R_g is the radius of gyration of the molecule in free solution. This is different than the free draining picture:

$$F_{stall} = E q_{eff} \quad (4.3)$$

Additionally, the authors predicted that a DNA molecule held against an electric field E would deform in the same way as one held against a uniform flow having velocity μE . These studies highlight how DNA immobilization dramatically alters the coupling of electro-hydrodynamic forces within the molecule.

It should be noted that the use of either fluid flow or an electric field to extend the molecules in the above experiments results in a tension that varies with position along the molecule's contour. A nanopore such as those described in Chapter 1 could also be used to apply an electrostatic force to the small segment of the molecule that is threaded through the nanopore. If the opposite end of the molecule is anchored to a bead then the molecule can be pulled from both ends, resulting in a uniform tension profile along its contour. In this configuration the forces acting on a single DNA molecule have been studied by several research groups.^{11–19} In these experiments, the molecules were driven into a nanopore but the counterbalancing stall force inhibited full translocation. With this approach, it was possible to determine the effective charge¹¹ and the hydrodynamic forces¹⁵ created by electroosmotic

flow (EOF). The attachment of a micrometer-sized bead, however, to macromolecules with smaller hydrodynamic radii can significantly perturb the electric fields, hydrodynamic forces, and molecular dynamics of the system.

The nanopores provided confinement on a small segment of the molecule and localized the electrostatic force acting on the molecule. Nanochannels, however, provide greater confinement, which contributes a significant entropic force in addition to the electrostatic and hydrodynamic forces investigated in the nanopore experiments. This entropic force often occurs at the microchannel-nanochannel interface, which was discussed in Section 1.3.2. In the case of a nanofunnel where the confinement changes more gradually, the magnitude of the entropic force is spatially variant and depends on the shape of the funnel.

In Chapter 3, a three-dimensional nanofunnel was described that decreased the threshold electric field, E_t , required to pull DNA molecules into a nanochannel. In this Chapter, the use of such a nanofunnel to stably trap a DNA molecule in sub-threshold electric fields is described. Similar to DNA behavior observed in the various scenarios described above, the statics and dynamics of a DNA molecule trapped in a nanofunnel are affected by entropic, electrostatic, and hydrodynamic forces. The balance of these forces is unique to the nanofunnel device. A stall force is imposed by the funnel-defined entropy gradient, not by anchoring to an immobilized bead. The magnitude of this stall force, and obviously of the electrostatic force, is varied by changing the voltage applied across the nanofunnel. This results in different conformations of the molecule as a function of electric field. The hydrodynamic forces acting on nanofunnel-trapped DNA molecules are qualitatively different than those of bead-anchored molecules. The well-defined, gradually varying

geometry makes the nanofunnel a sensitive force probe. The balance of spatially varying, field-dependent forces and the resulting DNA molecular conformations are understood through theoretical modeling developed through collaboration with Yanqian Wang, Dr. Sergey Panyukov, and Prof. Michael Rubinstein in the Department of Chemistry at UNC.

4.2 Materials and Methods

The device used for the studies in this Chapter was fabricated using the same protocols described in Chapter 3. A schematic of the experimental protocol is shown in Figure 4.1 a. In some funnel geometries, the forces exerted on DNA molecules are balanced such that a DNA molecule can be trapped indefinitely within the nanofunnel at a given voltage. This voltage is below the threshold necessary to induce translocation through the nanochannel but is sufficient to prevent diffusion of the DNA molecule out of the funnel and into the microfluidic reservoir. Similar to the threshold voltage measurements described in Section 3.2.3, solutions containing 0.25 ng/ μ L of λ -phage or T4-phage DNA in either 2X TBE or 2X TBE with 2% PVP were used to probe this trapping regime. Nanofunnels with $\alpha = 0, 0.5$ and 1 were tested (AFM images shown in Figure 4.1 b). The results described in this Chapter are reported for a nanofunnel having $\alpha = 0.5$, for reasons discussed below. A single molecule was introduced into the nanofunnel and then a sub-threshold (for translocation) voltage was applied. The molecule was imaged for at least 20 min at each voltage at a frame rate of 10 frames per second. If fragmentation was observed, the molecule was driven through the nanochannel and a new molecule was introduced to the nanofunnel. In this way, the full range of voltages over which DNA molecules were sustained within the nanofunnel was characterized using a few molecules. The series of images collected at each voltage was analyzed using an automated image analysis program written in Matlab to determine the

extension length and positions of the center-of-mass and ends of the DNA molecule in each frame.

4.3 Results and Discussion

The capture of DNA molecules within the nanofunnels that facilitated the threshold field measurements described in Chapter 3 implies a range of voltages over which DNA molecules can be stably trapped within a nanofunnel. The upper limit of this voltage range is defined by E_t , the threshold field strength, while its lower limit is E_{min} , the nanochannel field strength sufficient to prevent diffusion of the molecule out of the nanofunnel entrance. This trapping is achieved through a balance of counteracting electrostatic and entropic forces. By adjusting the geometry of the nanofunnel, the depth, width, and profile of the trap can be tuned. Figure 4.2 shows the qualitative energy landscapes of nanofunnels defined by a range of α values. The y-axis is the energy of a single Kuhn segment within a DNA molecule. Depending on whether α is larger or smaller than 0.5, the energy landscape is qualitatively different. In general, the energy well flattens as α increases, and disappears when $\alpha > 3.3$. For the purpose of lowering threshold electric field for translocation as described in Chapter 3, a flat energy well is preferred as the associated energy barrier for entering the nanochannel is smaller. For the purpose of establishing a range of voltages over which molecules can be stably trapped (the focus of this Chapter), a deeper energy well is preferred.

Experimentally, nanofunnels with $\alpha = 0, 0.5$, and 1 were characterized. The $\alpha = 1$ nanofunnel exhibits a narrow range of voltages over which DNA molecules are trapped, $E_{min} = 8.5$ V/cm and $E_t = 10.7$ V/cm for both λ -phage and T4-phage DNA in 2X TBE with 2% PVP. In contrast, DNA molecules are trapped across a wide range of voltages in the $\alpha = 0$ “funnel.” In this geometry, however, there is no shift in the position of the trap minimum

(the energy well in Figure 4.2) as the voltage is changed. As long as $qER_g > k_B T$, the molecule will drift to the entrance of the nanochannel. Imaging the molecule reveals the suppression of thermal motion and compression against the nanochannel entrance but there is no entropic force acting on the molecule. A more interesting situation is realized for the $\alpha=0.5$ nanofunnel, in which a DNA molecule can be held over a range of voltages and where the trap profile is voltage dependent. λ -phage and T4-phage DNA molecules were imaged when they were trapped within an $\alpha=0.5$ nanofunnel (connected with a nanochannel having a width of 96 nm and depth of 141 nm) in 2X TBE with and without the EOF suppressing additive PVP. Figure 4.3 shows representative data for T4-phage DNA in 2x TBE with 2% PVP when the electric field in the nanochannel was 9 V/cm. Figure 4.3 a is a bright field image showing the nanofunnel. Figure 4.3 b is a sample frame showing fluorescence from a trapped molecule. Each frame was analyzed using a Matlab program, and the intensity profile along the molecule was extracted. A representative intensity profile is shown in Figure 4.3 c. The intensity of the background (the baseline in the plot Figure 4.3 c) was offset to zero. Intensity profiles from each frame of the video were collected and stacked together to generate Figure 4.3 d. The molecule was imaged for approximately 20 minutes, but only 30 seconds of data is shown here. Thermal fluctuations are evident as changes in both the molecule's position and its extension length. The data collected for T4-phage DNA in 2X TBE without PVP are described in detail below. These are representative of similar results obtained in each of the four experiments and cover the widest range of voltages.

Figure 4.4 a shows the position of a DNA molecule's center of mass in an $\alpha = 0.5$ nanofunnel as a function of the nanochannel electric field strength. The lowest field strength in this plot is slightly greater than E_{min} while the highest field strength is slightly less than E_t .

As the field strength is increased, the molecule is pulled toward the nanochannel, reflecting the position of the trap where forces are balanced. In the $\alpha = 0.5$ nanofunnel, this is easier at low field strengths because the entropic force is lesser near the nanofunnel's wide end and greater at its nanoscale end. The error bars in Figure 4.4 a are significantly greater than the measurement uncertainty and represent the molecule's thermal fluctuations (i.e., the data are not thermally averaged). This is also illustrated in Figure 4.4 b, which shows the positional traces of the molecule at several field strengths. As the molecule moves toward the nanochannel with an increase in voltage, it experiences both greater confinement and greater compression as a result of the deepening trap. Fluctuations are therefore suppressed.

Well established polymer physics theories predict an increase in DNA extension as the molecule experiences greater confinement.²⁰ These theories, however, do not consider the effects of a counteracting electric field on the end-to-end length of DNA molecules. Figure 4.5 a shows the length of a T4-phage DNA molecule as a function of the nanochannel electric field strength. Initially, as the voltage is increased, the molecule extends as it is moved into the more confining region of the nanofunnel. At intermediate electric field strengths there is little change in the DNA's extension length, despite the fact that the molecule's center of mass moves toward the region of greater confinement as the voltage is increased. At higher electric field strengths there is a reduction in the DNA extension length. This results from the asymmetric profile of the trap (Figure 4.2 a). At higher field strengths, the leading end of the DNA molecule is pushed against a steep barrier preventing transport into the nanochannel. Little translation occurs with a further increase in the field strength, provided that the electric field strength remains below the threshold for translocation. The trailing end, on the other hand, is less constrained and can translate a greater distance upon an

increase in the electric field strength. This results in a compression of the molecule, an additional force that is resisted by molecular self-exclusion and that contributes to threshold lowering. As in the case of positional fluctuations, the end-to-end intramolecular fluctuations represented by the error bars in Figure 4.5 a are suppressed at higher field strengths.

The trap asymmetry discussed above means that the fluctuations (both center-of-mass and end-to-end) are likewise asymmetric. This is illustrated by the contour plots and distributions shown for various field strengths in Figure 4.5 b-d. The histograms of DNA length show a decrease in variance as the electric field strength increases, as manifested by the decrease in the error bars in Figure 4.5 a. They also exhibit an increase in skewness with increasing field strength, which signifies that the ease with which the molecule extends relative to the ease with which it contracts increases as the confinement and field induced compression increase.

The position of the molecule's center of mass (red traces in Figure 4.5 b-d) appears to be normally distributed, regardless of electric field. Additional information is revealed, however, by averaging DNA extension length as a function of center-of-mass position from the ~12000 images recorded at each field strength (black traces in Figure 4.5 b-d). This is equivalent to averaging over vertical slices of the contour plots. Correlation between the two parameters is indicated by a non-zero slope in these traces, which corresponds to a rotation of the contour axes relative to the contour plot coordinate axes. At low field strengths, there is little correlation between the two parameters. The molecule diffuses longitudinally but the potential energy trap is shallow and end-to-end fluctuations dominate position (and confinement) controlled extension. At high field strengths, there is a strong dependence of the extension length on positional fluctuations, one that follows the trend of the static

(averaged over all frames) measurements. This provides a complementary measure of the trap depth and asymmetry at a given field strength. This profile is further characterized by considering the positions of the molecule's ends. The positional distribution of the leading and trailing ends of the molecule are the green and blue plots in Figure 4.5 b-d, respectively. The steeper energy barrier experienced by the leading end is reflected in the narrowness of this distribution, relative to that of the trailing end. Furthermore, the fact that the distribution becomes less skewed at high electric field strengths indicates the compressed state of this end of the molecule. The asymmetric trap expected from entropic and electrostatic forces would result in more facile fluctuations away from the nanochannel entrance. At low field strengths, this skew to the right is indeed seen in the leading end positional histograms. At high field strengths, however, compression from neighboring DNA monomers constrains these fluctuations away from the nanochannel. The trailing end of the DNA molecule exhibits a broader positional distribution because this end of the molecule is less constrained. In contrast to that of the leading end, the distribution becomes more skewed as the electric field strength increases because resistance to motion towards the nanochannel increases as the molecule becomes more compressed.

To quantitatively calculate the forces on the molecule, Wang, Panyukov, and Rubinstein examined the electro-hydrodynamic flow profiles for molecules in different systems and proposed a theory to model the experimental behavior.²¹ In the case of DNA free electrophoresis (Figure 4.6 a1), the fluid very close to the molecule strands moves at the same velocity (non-slip), and the fluid outside the Debye length is at rest, the “free draining” behavior discussed earlier in this Chapter. The flow velocity profile within a Debye length is

depicted in Figure 4.6 a2. The velocity is maximal close to the strand and decays to zero over a distance on the order of the Debye length.

For an anchored DNA molecule (secured to a bead in an optical trap, for example) within an electric field (Figure 4.6 b1), the counterions are pumped by the electric field through the molecule, dragging fluid along with them. The fluid flows along the path of minimal hydraulic resistance, circulating back around the molecule over a distance comparable to R_g . Only a fraction of the momentum is transferred to this circulating flow, while the rest is transferred to the molecule, countering the stall force. The net electro-hydrodynamic force has the same magnitude as Equation 4.2. The flow profile between two adjacent segments of the molecule (with an interstrand distance, ζ_H) is depicted in Figure 4.6 b2. The flow velocity is zero close to the segments and reaches a maximum at a distance on the order of Debye length.

For the nanofunnel experiment discussed in this Chapter (Figure 4.6 c1), the DNA molecule is held still in a confined volume in an electric field. The fluid pumped by the electric field cannot circulate around the outside of the molecule as this pathway is restricted by the nanofunnel walls. If the hydraulic resistance of the system is extremely low, the fluid is constantly pumped through the molecule. In the case where the hydraulic resistance of the system is larger than that of flow through the molecule itself, the fluid circulates back through the molecule. The flow profile for this second case is depicted in Figure 4.6 c2. The flow velocity is zero close to the DNA segments, and increases to a maximum at the Debye length. The velocity decreases farther away from the molecule segments and eventually reverses direction in the volume between segments. From these arguments, an equation calculating the electro-hydrodynamic force on a Kuhn segment is proposed:

$$F_{eh} = \frac{q_{eff}E}{\ln(\xi_H/a)} \quad (4.4)$$

where q_{eff} is the effective charge and a is the diameter of the molecule. In the system where a background flow with flux J_{back} is present (EOF, for example), Equation 4.4 is modified:

$$F_{eh} = \frac{q_{eff}E - 4\pi\eta l_p J_{back}/A}{\ln(\xi_H/a)} \quad (4.5)$$

where A is cross sectional area of the nanofunnel in which the Kuhn segment is confined.

Based on the arguments above, the position of the molecule in the funnel as a function of electric field was predicted. These results are in close agreement with the experimental data as shown in Figure 4.7.

4.4 Conclusion

In this Chapter, the trapping of a single molecule originating from the balance of the entropic, electrostatic, and hydrodynamic forces is described. This unique system provides a trapping method without the need for attaching a bead or force microscope probe to a DNA molecule. The nanofunnel can significantly impact the hydrodynamic flow profile within the molecule. This effect must be considered to achieve convergence between force balancing theories and the experimental results. Such a comprehensive theory was developed through collaboration with Rubinstein et al. to better understand the experimental results.

4.5 REFERENCES

1. Rubinstein, M. & Colby, R. H. *Polymer Physics*. (OXFORD university press, 2003).
2. Hugel, T. & Seitz, M. The Study of Molecular Interactions by AFM Force Spectroscopy. *Macromol. Rapid. Comm.* **22**, 989 (2001).
3. Neuman, K. C. & Block, S. M. Optical trapping. *Rev. Sci. Instrum.* **75**, 2787 (2004).
4. Bustamante, C., Macosko, J. C. & Wuite, G. J. Grabbing the cat by the tail: manipulating molecules one by one. *Nat. Rev. Mol. Cell. Bio.* **1**, 130 (2000).
5. Neuman, K. C. & Nagy, A. Single-molecule force spectroscopy : optical tweezers , magnetic tweezers and atomic force microscopy. *Nat. Methods* **5**, 491 (2008).
6. Perkins, T. T., Smith, D. E., Larson, R. G. & Chu, S. Stretching of a single tethered polymer in a uniform flow. *Science* **268**, 83 (1995).
7. Long, D., Viovy, J. & Ajdari, A. A Zimm model for polyelectrolytes in an electric field. *J. Phys.: Condens. Matter* **8**, 9741 (1996).
8. Long, D., Viovy, J. & Ajdari, A. Stretching DNA with electric fields revisited. *Biopolymers* **39**, 755 (1996).
9. Long, D., Viovy, J. & Ajdari, a. Simultaneous action of electric fields and nonelectric forces on a polyelectrolyte: Motion and deformation. *Physical review letters* **76**, 3858–3861 (1996).
10. Viovy, J.-L. Electrophoresis of DNA and other polyelectrolytes : Physical mechanisms. *Rev. Mod. Phys.* **72**, 813 (2000).
11. Keyser, U. F. *et al.* Direct force measurements on DNA in a solid-state nanopore. *Nature Physics* **2**, 473–477 (2006).
12. Keyser, U. F., van der Does, J., Dekker, C. & Dekker, N. H. Optical tweezers for force measurements on DNA in nanopores. *Review of Scientific Instruments* **77**, 105105 (2006).
13. Trepagnier, E. H., Radenovic, A., Sivak, D., Geissler, P. & Liphardt, J. Controlling DNA capture and propagation through artificial nanopores. *Nano Lett.* **7**, 2824–30 (2007).
14. Sischka, A. *et al.* Single beam optical tweezers setup with backscattered light detection for three-dimensional measurements on DNA and nanopores. *The Review of scientific instruments* **79**, 063702 (2008).

15. Van Dorp, S., Keyser, U. F., Dekker, N. H., Dekker, C. & Lemay, S. G. Origin of the electrophoretic force on DNA in solid-state nanopores. *Nat. Phys.* **5**, 347–51 (2009).
16. Peng, H. & Ling, X. S. Reverse DNA translocation through a solid-state nanopore by magnetic tweezers. *Nanotechnology* **20**, 185101 (2009).
17. Van den Hout, M., Vilfan, I. D., Hage, S. & Dekker, N. H. Direct force measurements on double-stranded RNA in solid-state nanopores. *Nano Lett.* **10**, 701–7 (2010).
18. Steinbock, L. J. *et al.* Probing DNA with micro- and nanocapillaries and optical tweezers. *Journal of physics. Condensed matter : an Institute of Physics journal* **22**, 454113 (2010).
19. Sischka, A. *et al.* Dynamic translocation of ligand-complexed DNA through solid-state nanopores with optical tweezers. *Journal of physics. Condensed matter : an Institute of Physics journal* **22**, 454121 (2010).
20. Reisner, W., Pedersen, J. N. & Austin, R. H. DNA confinement in nanochannels: physics and biological applications. *Rep. Prog. Phys.* **75**, 106601 (2012).
21. Wang, Y., Panyukov, S. & Rubinstein, M. Unpublished results. (2013).

4.6 Figures

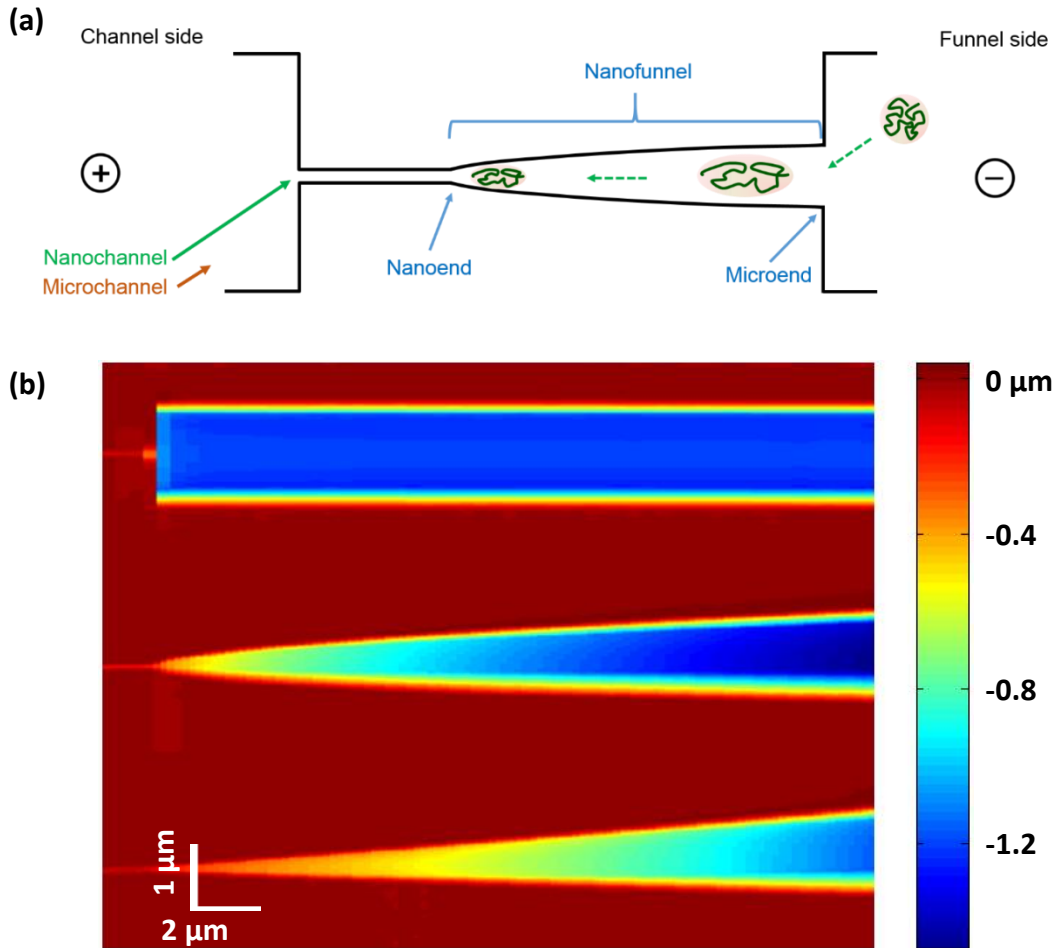


Figure 4.1 Trapping single DNA molecules in a three dimensional nanofunnel. **a)** Schematic representation of the trapping experiment. After the DNA molecule was introduced into the funnel, a constant voltage was applied to hold the molecule. **b)** AFM images showing the funnels with $\alpha = 0, 0.5$, and 1, from top to bottom.

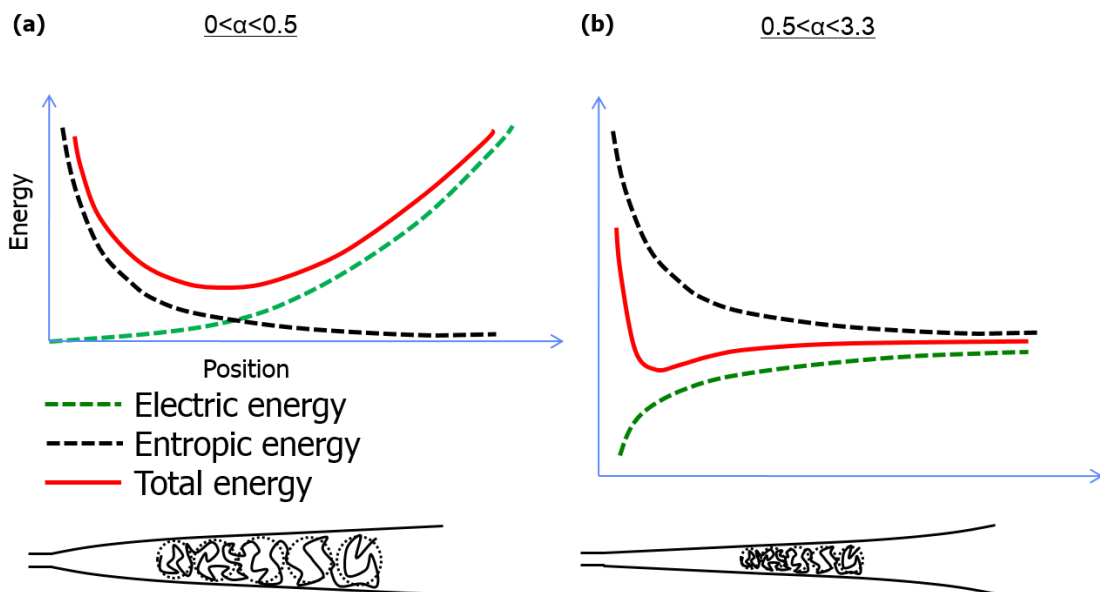


Figure 4.2 Energy landscape for a single Kuhn segment of the DNA molecule in funnels with different shapes. The green dashed line is the electric energy, the black dashed line is the entropic energy, and the red solid line is the total energy. **a)** Energy landscape for $0 < \alpha < 0.5$. **b)** Energy landscape for $0.5 < \alpha < 3.3$. This figure is kindly provided by collaborators Yanqian Wang, Dr. Sergey Panyukov, and Prof. Michael Rubinstein.

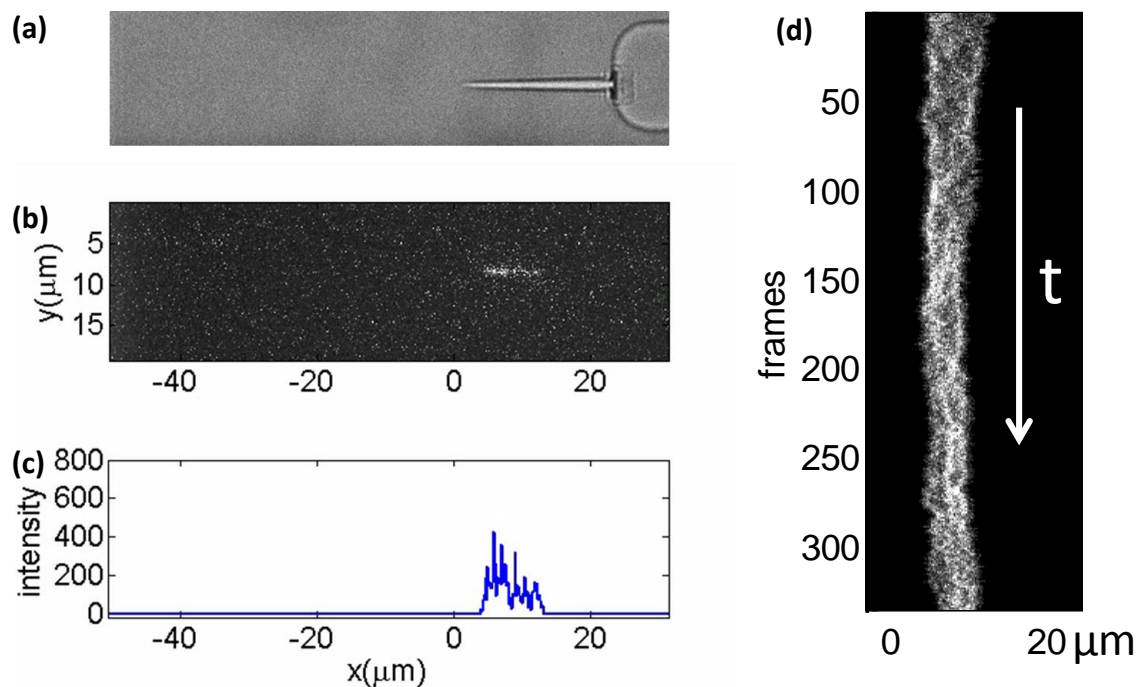


Figure 4.3 The data processing of the videos using a Matlab program. The data showed here are for T4 DNA in the solution without PVP. The voltage applied was 60 mV. **a)** A bright field image showing the location of the funnel when the video was recorded. **b)** A sample image showing one frame from the video. **c)** A line intensity profile was extracted from (b) to determine the location and the length of the molecule. **d)** Intensity profiles from a series of frames are stacked together showing the thermal fluctuations. The image contains information from 350 frames.

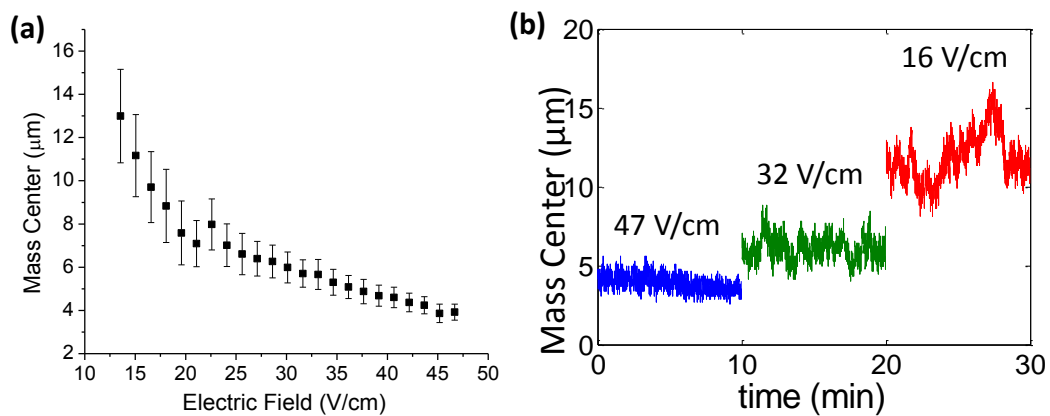


Figure 4.4 Trapping a single DNA molecule in the nanofunnel: location changes as a function of field. a) Position change as a function of electric field in the nanochannel. **b)** Representative 10 minute traces for three different electric fields.

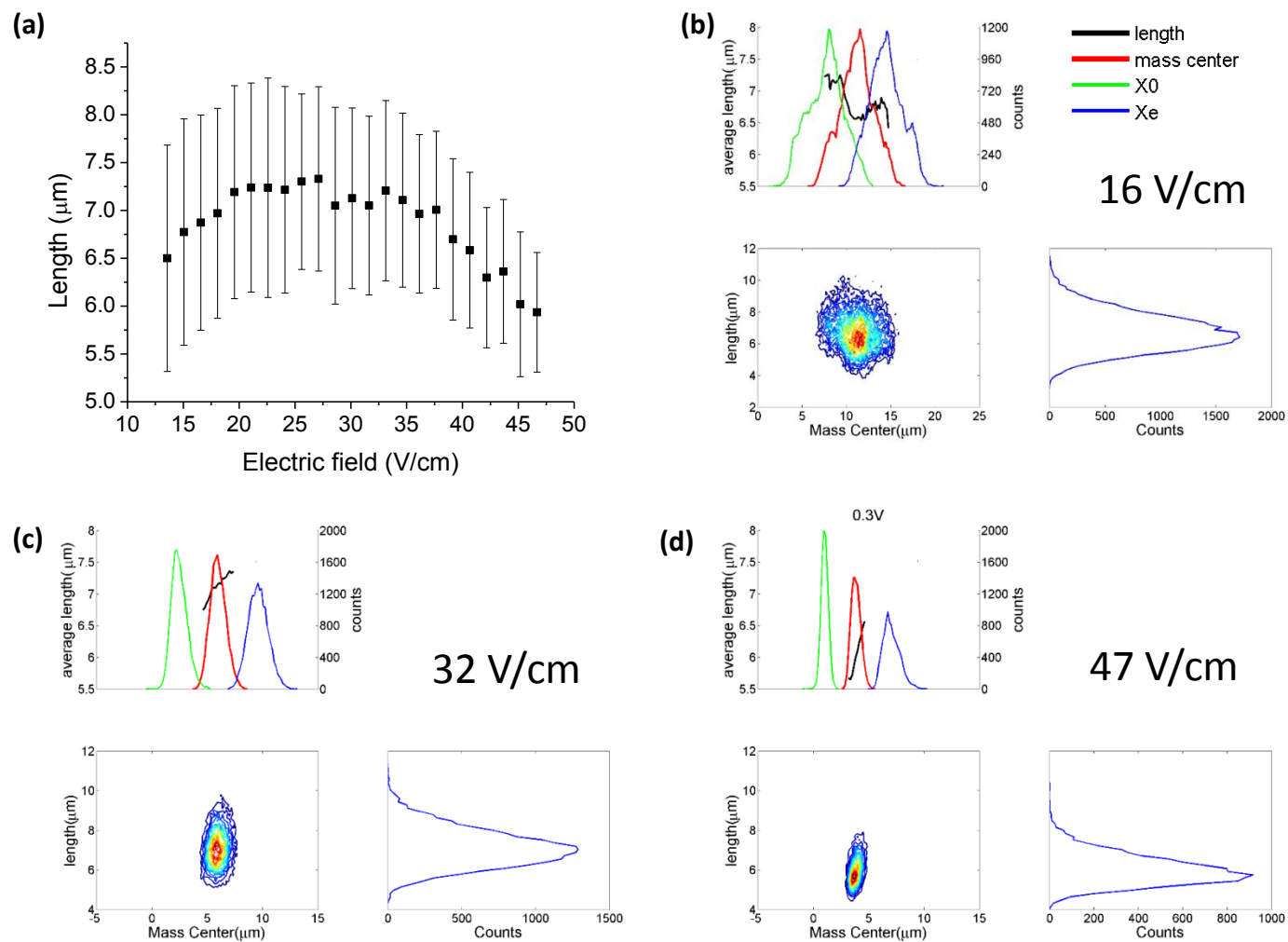


Figure 4.5 Trapping a single DNA molecule in the nanofunnel. a) Length changes as a function of field. **b-d)** Distribution of molecule location and length at various electric fields.

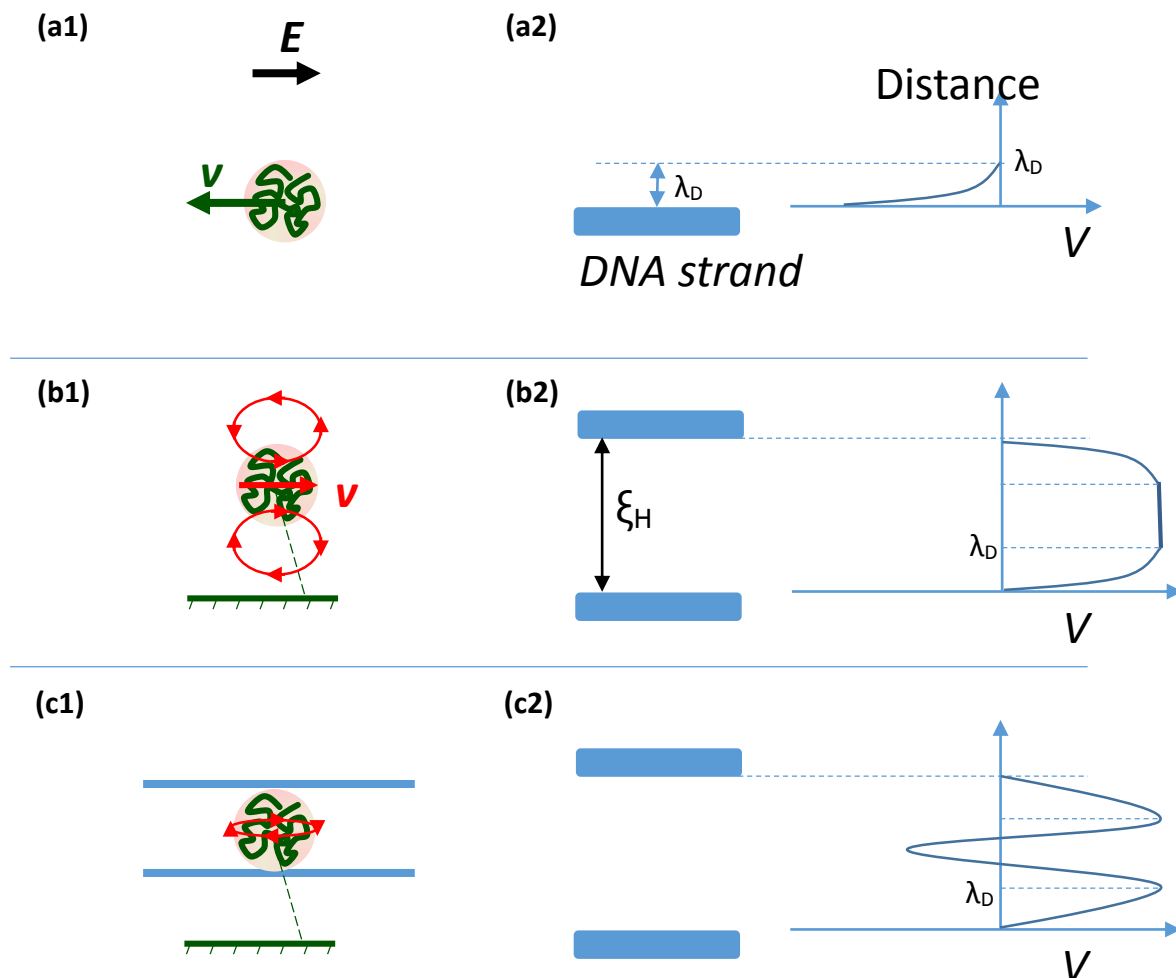


Figure 4.6 Electrohydrodynamic flow profiles for DNA molecule in different systems. a1, b1, and c1 are the schematics of the DNA and the flow profiles. a2, b2 and c2 are the flow profile at a distance away from a DNA strand. **a)** The free DNA electrophoresis. a2 shows the flow velocity is the same as the DNA strand at zero distance, and zero at a distance λ_D . **b)** DNA molecule held against the electric field in free solution. The flow velocity shown in b2 reaches a maximum value at a distance λ_D away from the strand. **c)** DNA molecule held against the electric field in a nanochannel. The flow velocity reaches a maximum value at a distance λ_D . This figure is adapted from a figure kindly provided by collaborators Yanqian Wang, Dr. Sergey Panyukov, and Prof. Michael Rubinstein.

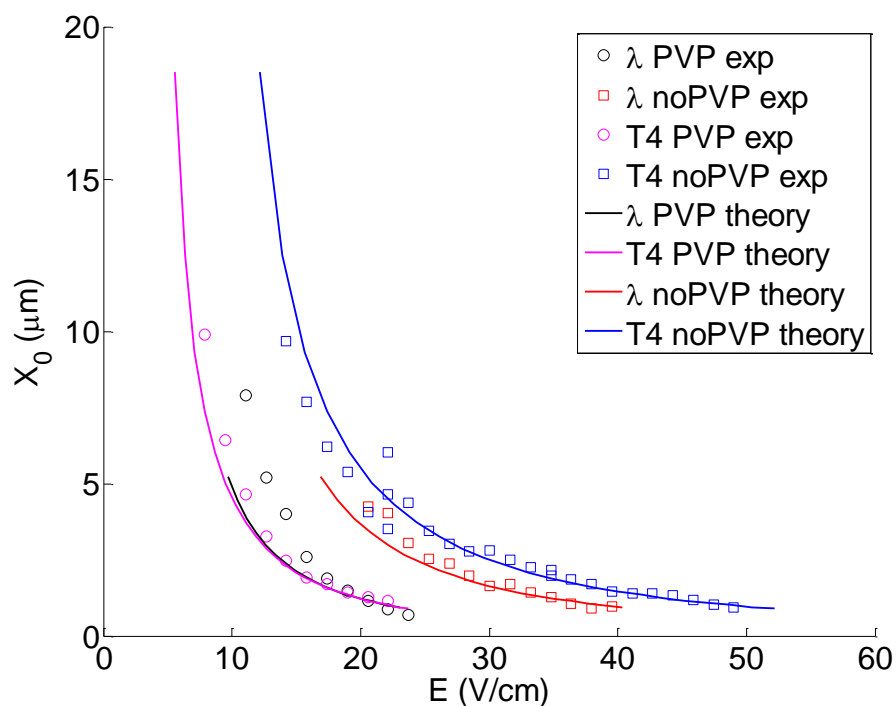


Figure 4.7 Dependence of the leading end of the DNA molecule in the nanofunnel (x_0) on the nanochannel electric field. Experimental data are represented by the markers while solid lines represent the theoretical predictions. This figure is kindly provided by collaborators Yanqian Wang, Dr. Sergey Panyukov, and Prof. Michael Rubinstein.

Chapter 5: Concentration Polarization in Three-Dimensional Nanofunnel

Systems Introduction

In the previous Chapters, the confinement effects of nanochannels and nanofunnels on the analysis of DNA molecules were discussed. Additional fluidic phenomena unique to nanoscale systems were also observed in these three-dimensional nanofunnel systems. When an electric field is applied across a nanochannel filled with low ionic strength solutions, the creation of enriched and depleted ionic concentration regions at the interfaces can occur. This is an effect called concentration polarization (CP).¹⁻³ CP also affects the voltages across the fluidic system, which in turn influences the transport behavior.⁴ Such perturbations are often unwanted in fluidic manipulation, when proportional responses to applied voltages are desired.⁵⁻⁷ For example, Hlushkou et al. used a nanoporous hydrogel as a size-exclusion membrane to concentrate charged analytes with diameters greater than the mesh size.⁶ The same degree of concentration required a higher voltage for the charged hydrogel compared to the neutral hydrogel, because of CP, which has the potential to increase Joule heating. On the other hand, novel applications are possible through the exploitation of CP and the generation of local field gradients.⁸ Many experiments and theories have been developed to understand and predict this effect.^{4,6,8-16}

Early work on this topic can be traced back 50 years, when colloidal dispersions and ionic exchange membranes were extensively studied.¹⁷ For an ionic exchange membrane with pore sizes on the order of a few nanometers in an electric field, the current is carried almost exclusively by the counterions because of the membrane's charged surface.¹⁷ This is

in contrast to conductance in the bulk solution, where the current is also carried by the co-ions (Figure 5.1). The counterion flux across the membrane is therefore higher than in the bulk (arrows in Figure 5.1). This mismatch is partially compensated by diffusion of the ions, which is a function of the ionic concentration gradient (purple lines in Figure 5.1) according to Fick's first law.¹⁷ For low ionic concentrations and high current density, this flux mismatch creates ion enrichment and depletion regions at the two interfaces of the membrane, called the diffusive boundary layer (DBL).^{3,17} The depletion region increases the overall ionic resistance of the system. At a certain point the concentration in this region continues to decrease with an increase in the applied voltage. At this point, any increase in voltage is compensated by a proportional increase in resistance. The current therefore fails to increase further, despite the increased voltage. This plateau in the I-V curve is referred to as the "limiting current".³ Eventually, as one continues to increase the driving voltage, the current starts to again increase,¹⁸ a phenomena called "over-limiting current." Initially, this was explained by invoking water dissociation, so that the ionic strength never reaches zero because of the dissociated water ions.¹⁷ Rubinstein et al. pointed out that water dissociation alone couldn't account for all of the effects.¹⁹ Instead, when the concentration in the depletion region approaches zero the flow becomes unstable, inducing convective mixing and preventing a further decrease of concentration in the depletion region.²⁰

The first observation of concentration polarization in a nanochannel system was reported by Pu et al. in 2004.¹⁰ Two microchannels (100 μm deep \times 750 μm wide) were bridged by an array of eight nanochannels (60 nm deep \times 100 μm wide) in devices fabricated in borofloat glass. They used a negatively charged fluorophore (fluorescein) and a positively charged fluorophore (rhodamine 6G) to visualize the concentration changes at the

microchannel-nanochannel interfaces when a voltage was applied. The solution was a 70 μM to 3 mM sodium tetraborate buffer ($\text{pH} = 8$) with either 30 μM of fluorescein or 10 μM of rhodamine 6G. For both probes, ionic depletion was observed at the anodic side of the nanochannel array while enrichment occurred at the cathodic side.¹⁰ Such effects were observed in low ionic strength solutions (<1 mM) but not for higher buffer concentrations (3 mM). The authors speculated that the degree of electrical double layer (EDL) overlap determined the occurrence of CP.

In 2007, Kim et al. used a 40 nm deep nanochannel array to study CP by monitoring fluorescently labeled probes and simultaneously measuring ionic current changes.¹² Concentration polarization was found to occur at relatively high ionic strengths, at which EDL overlap was not significant. The current measurements showed that the “limiting current” was correlated with the onset of the CP. As the applied voltage increased, an expansion of the enrichment and depletion regions was observed, reaching several millimeters in extent. The authors pointed out that the fixed DBL model of the classical CP theory is not valid and that the system is at non-equilibrium. Furthermore, the vortices predicted by Rubinstein et al.²⁰ were observed.

In the above experiments, in which low concentrations of fluorescent probes were used to monitor concentration polarization, only a small portion of the current was carried by the probes. The observed intensity change acted as an indicator of the background ionic concentration change. Additionally, the use of a nanochannel array is somewhat complex, because the CP for each nanochannel couples with that of adjacent nanochannels. In 2009, Zangle et al. conducted experiments using a single nanochannel filled with charged fluorescent probes (Alexa Fluor 488 or fluorescein) dissolved in deionized water.^{14,15} The

dye molecules therefore served not only as concentration probes but also, along with their counterions, as charge carriers (i.e., 2Li^+ and (Alexa Fluor) $^{2-}$ or 2Na^+ and fluorescein $^{2-}$). The nanochannel was 50 or 100nm deep \times 20 μm wide and coupled 1 μm \times 20 μm microchannels at both ends. By applying a constant current, CP regions were found to expand linearly as a function of time in the microchannels, and this expansion was called “CP propagation.” Models were developed to describe the CP propagation in the context of an inverse Duklin number, which represents the relative importance of bulk and surface conductance.¹⁴ Along with a review paper later,¹ the authors pointed out that EDL overlap, the often cited requirement for concentration polarization, is not a prerequisite for the effect. Concentration polarization and CP propagation can occur when the double layers are significantly thinner than the nanochannel height.

Another phenomenon that is related to the surface charge is ionic current rectification (ICR) in an asymmetric nanofluidic system. In symmetric systems discussed previously (nanochannel or nanoporous membrane), an applied voltage produces a given current magnitude regardless of polarity. However, voltages with different polarities applied to an asymmetric system results in different current magnitudes (an asymmetric I-V curve). This non-ohmic phenomenon is referred to as ionic current rectification (ICR). ICR was first reported by Wei et al. and was observed in quartz nanopipet electrodes.¹⁹ Later studies showed that ICR is related to the surface charge, as evidenced by its sensitivity to the electrolyte used (KCl or KF) and to solution pH.²¹ Electrical potentials were calculated in the pore and a ratchet mechanism was used to explain the preferential direction of the ionic flow, which is strong enough to pump ions against a concentration gradient.^{22,23} Instead of the asymmetric channel geometry, a manipulation of the surface charge can also have the same

effect. Karnik et al. observed ICR in a geometrically symmetric channel in which half of the channel was positively charged while the other half was neutral.²⁴ A combination of both geometric and charge effects has resulted in rectification ratios [current(high conductance polarity):current(low conductance polarity)] up to ~200.²⁵ Vlassouk and Siwy studied such nanofluidic diodes and speculated the effect was caused by the enrichment and depletion zones in the funnel shaped channel.

For the ICR studies discussed above, a visualization of the local ionic concentrations and their evolution would be beneficial. In 2010, Perry et al. studied ionic current rectification in an in-plane two-dimensional (constant depth, varying width) funnel system, in which ion transport was monitored using fluorescent probes, a technique common in CP studies.²⁶ The system consisted of a nanofunnel connecting two nanochannels. The funnel was 1 μm wide at the base and 80 nm wide at the tip. The nanochannel was 1 μm wide and 40 μm long. Both the nanochannel and the funnel were 120 nm deep. The authors found that ICR correlated with the concentration change of the fluorescent probes, and that the taper of the funnel affected the degree of ICR. Hlushkou et al. simulated the ionic concentration in such a system and found the CP generated could propagate into the nanochannels but only when the system was driven in one direction, with cations migrating from funnel tip to base.²⁷

In this Chapter, the ionic current rectification in a three-dimensional nanofunnel system, similar to those fabricated for DNA single-molecule studies, is explored. By simultaneously measuring the concentration change and monitoring the current change over time, ICR was found to be correlated with the CP propagation into the microchannels.

Additionally, CP was found to be greatly influenced by the electro-osmotic flow (EOF), which was adjusted by adding a dynamic coating that changed the surface viscosity.

5.2 Materials and Methods

Device fabrication was performed in the same manner as described in Chapters 2 and 3. Schematic representations of fluidic device and the microchannel and nanochannel geometry are shown in Figure 5.2 a and b. The microchannels were 3 μm deep, 17 μm wide and 8-11 mm long from reservoir to nanochannel. Two microchannels were bridged by a nanochannel-nanofunnel conduit. The nanochannel was 6.5 μm long, 90 nm wide and 40 nm deep (Figure 5.2 c and d). It was connected smoothly with the nanofunnel which gradually increased in both width and depth to 1.5 μm over a 20 μm length with $\alpha = 0.5$ (see Chapter 3 for the meaning of α).

The buffered electrolyte solution used was 0.1x TBE (9 mM Tris, 9 mM boric acid, 0.2 mM EDTA). This was diluted from a 10x TBE stock solution (Fisher Scientific). For some experiments, the buffer contained 2% (by mass) polyvinylpyrrolidone (PVP, 10 kDa, Sigma-Aldrich). Fluorescein (Sigma-Aldrich) solutions were prepared in these buffers at a concentration of 500 μM . The solution conductivity and pH were measured using a Mettler Toledo meter. The fluorescein solution in 0.1x TBE solution (no PVP) had a bulk conductivity of 585 $\mu\text{S}/\text{cm}$ and a pH of 8.4. The fluorescein solution in 0.1x TBE (2% PVP) had a bulk conductivity of 560 $\mu\text{S}/\text{cm}$ and a pH of 8.2.

The device was mounted on an inverted fluorescence microscope (Eclipse TE2000-U, Nikon) and imaged through a 40x objective (Nikon). Fluorescence was excited using a 100-W mercury arc lamp filtered through a GFP-3035 filter set (excitation at 472 nm, emission at 520 nm, Semrock) and images were recorded using a Cascade II EM-CCD camera

(Photometrics). These images were analyzed using an automated image analysis program written in Matlab.

Two freshly prepared Ag/AgCl electrodes (polished and immersed in household bleach (~5% sodium hypochlorite) for 15 minutes) were inserted into the reservoirs accessing the microchannels (Figure 5.2 a). A single voltage was supplied using a Keithley 6487 Picoammeter Voltage Source (Keithley Instruments, Inc.) This same instrument, controlled by a custom Labview program, was also used to monitor the current response. The voltage applied was ± 0.5 V, ± 1 V, ± 2 V, ± 5 V, ± 10 V, and ± 20 V, where the positive designation indicates that a positive bias was applied at the nanochannel side of the nanochannel-nanofunnel duplex. The collection of both fluorescence images and ionic currents was initiated, followed by application of the voltage after 10 seconds. Images were collected at 25 frames per second (fps) for the first 30 seconds and 9 fps thenceforth. The ionic current was sampled at 13 Hz (medium sampling rate setting on the Keithley 6487).

Because of the CP and its propagation, the ionic concentration in the microchannels was altered during the course of each experiment (i.e., collection of each current trace). To ensure that each experiment was conducted with the same initial bulk concentration, a fresh solution was introduced to the microchannels after each experiment and before collecting the next current trace.

5.3 Results and Discussion

Figure 5.2b and c show SEM images of the microchannel/nanochannel area of the device. In Figure 5.2c, the nanofunnel runs from right to left into the nanochannel. To investigate concentration polarization, both positively and negatively biased voltages were applied across the nanochannel-nanofunnel junction. A positive voltage meant that cations

were driven from the nanochannel side to the nanofunnel side. Figure 5.3 is a series of fluorescence images showing the concentration (intensity) change of fluorescein (negatively charged) over time. Figure 5.3 a shows the response when +5 V was applied while Figure 5.3 b shows the response with a negative voltage. At $t=0$ s, with no voltage applied to the device, the intensities on both sides of the nanochannel-funnel were identical. When +5 V was applied (Figure 5.3 a), the intensity in the nanofunnel increased, while the intensity at the intersection between the microchannel and nanochannel decreased. This intensity change shows the enrichment and depletion of fluorescein molecules in the nanofunnel and the nanochannel end, respectively. At long times (> 2 s), the regions of fluorescein enrichment and depletion propagated from the nanofluidic components into the microchannels. At 60 seconds, the depletion area had completely propagated out of the field of view. When -5 V was applied (Figure 5.3b), the intensity decreased at the nanofunnel side and increased at the nanochannel side, with the enrichment and depletion zones similarly propagating out into the microchannels.

To better appreciate the dynamics of CP propagation into the microchannels, a linear intensity profile was extracted (the red dashed line in Figure 5.3 a, 0 s) from each frame. This process is illustrated in Figure 5.4. At 0 s, the intensities in the microchannels are roughly equivalent. The intensity in the nanochannel-nanofunnel region is significantly less because of the shallower depth and shorter path length of this region (Figure 5.4 b). Figure 5.4 c and d show similar intensity profiles from the same line generated from frames collected at 2 s and 5 s, respectively. Over time, the intensity at the funnel side increases while the intensity at the channel side decreases. Figure 5.5 a and c show two-dimensional image plots that were generated from intensity profiles similar to those shown in Figure 5.4 b-d. Here, the

intensities are represented by the color scale and the profiles from all of the collected frames are stacked vertically. The intensities are normalized with the highest intensity in the plot equal to one and the lowest intensity equal to zero. The images show that, in addition to propagation of the enrichment and depletion regions into the microchannels, the concentration in the enrichment area continues to increase over several minutes.

The buffer ionic strength is ~ 3.4 mM,²⁸ which has a corresponding Debye length of ~ 5 nm. This Debye length is smaller than the channel depth, 40 nm, but strong CP was still observed. Past studies by others have described the ionic transport through simulations using the Poisson-Nernst-Planck equation and the Navier-Stokes equation,^{3,27,29} and simple models have been proposed to study CP propagation.¹⁴ Here, a very simple model is discussed to help understand CP.¹⁰

The ionic current in the system is carried by both the cations and anions. The buffer solution is assumed to be composed of a symmetric univalent electrolyte and the mobile ion concentration is noted as $[+]$ and $[-]$.³⁰ The ionic current in the microchannel is:

$$J_m = J_m^+ + J_m^- \quad (5.1)$$

where J_m is the total ionic current in the microchannel, J_m^+ is the cationic current, and J_m^- is the anionic current. Similarly, in the nanochannel,

$$J_n = J_n^+ + J_n^- \quad (5.2)$$

These currents (in units of mol/s) can be described by the following equations:

$$J_m^+ = E_m \mu_m^+ [+]_m A_m \quad (5.3)$$

$$J_m^- = E_m \mu_m^- [-]_m A_m \quad (5.4)$$

$$J_n^+ = E_n \mu_n^+ [+]_n A_n \quad (5.5)$$

$$J_n^- = E_n \mu_n^- [-]_n A_n \quad (5.6)$$

Where E is the electric field, μ is the ionic mobility, and A is the cross-sectional area of the respective channels. Assuming the concentration $[+]$ and $[-]$ follows:

$$[+]_m = \beta_m [-]_m \quad (5.7)$$

$$[+]_n = \beta_n [-]_n \quad (5.8)$$

Where β_m and β_n are the ratio of the cation and anion concentrations in the microchannel and nanochannel, respectively. At any time, the ionic current through both microchannels and nanochannels must be equivalent:

$$J_m = J_n \quad (5.9)$$

Combining Equations 5.1-5.9 gives:

$$\frac{J_m^+}{J_n^+} = \frac{\frac{1}{\beta_n} \mu_n^- \mu_m^+ + \mu_n^+ \mu_m^+}{\frac{1}{\beta_m} \mu_m^- \mu_n^+ + \mu_n^+ \mu_m^+} \quad (5.10)$$

Assuming that the mobility of each ion in a nanochannel is identical to its mobility in the microchannel and that the concentration of $[+]$ and $[-]$ are identical in the microchannel ($\beta_m = 1$), Equation 5.10 becomes

$$\frac{J_m^+}{J_n^+} = \frac{\mu^+ + \frac{1}{\beta_n} \mu^-}{\mu^+ + \mu^-} \quad (5.11)$$

The fused quartz substrate used here is negatively charged. The cation thus has a higher concentration than the anion in the nanochannel ($\beta_n > 1$). As a result, $\frac{J_m^+}{J_n^+} < 1$, meaning the flux of cations in the nanochannel is larger than in the microchannel. This mismatch causes

cations to accumulate on the cathodic side of the nanochannel, and deplete on the anodic side. A similar analysis predicts that the anion will be enriched at the cathodic side and depleted at the anodic side. The ratio $\frac{J_m^+}{J_n^+}$ is a parameter roughly indicating the degree of concentration polarization across a nanochannel, with ratios approaching 1 corresponding to lesser CP. Note that this analysis is for a negatively charged nanochannel surface.

This simplified model correctly predicts the occurrence of CP, but a real system has much richer phenomena. As seen in the fluorescence signal, the ionic concentration continues to change in the microchannels. This changes the local resistance, as well as the total resistance, which is reflected in the current measurements. Figure 5.5 b and d shows the current traces corresponding to the fluorescence profiles.

Identical experiments were performed at various voltages. Figure 5.6 a provides a summary of the current traces recorded for buffer solutions with PVP at various applied voltages (± 0.5 V, ± 1 V, ± 2 V, ± 5 V, ± 10 V, and ± 20 V). The voltage was applied at $t = 10$ s and maintained for 300 s. For small voltages (< 1 V), the current remained relatively constant while at higher voltages the current decayed over time. At higher voltages, two distinctive regimes were observed: a sharp spike at the beginning of the trace followed by a slow decay over time. The sharp spike is hypothesized to result from the initial concentration change near the nanochannel-microchannel interface (nanochannel side) or in the funnel (nanofunnel side), while the slower decay is caused by the CP propagation into the microchannel. Converting the current traces in Figure 5.6 a into resistance traces yields Figure 5.6 b. As expected, no significant change in the resistance of the system was seen at low voltages (< 1 V). In contrast, the resistance increased throughout the experiment at higher voltages (> 5 V).

The resistance of the system was also greater at higher voltages, indicating a greater degree of concentration polarization.

Because the device consisted of an asymmetric geometry, current rectification was expected to occur. Previous studies characterized this rectification by plotting an I-V curve to determine its symmetry.^{19,21–26} Such methods are appropriate as long as the current quickly approaches a steady-state value. This criterion was not met in the nanochannel-nanofunnel measurements, as is evident in Figure 5.6. The system did not reach equilibrium during the course of the experiments and, according to the above hypothesis of the current response, it would not do so until the CP propagated the length of the microchannels into the reservoirs. The time variant concentrations and currents preclude the characterization of the system using a single I-V curve. The voltage scan rate and direction would be expected to dramatically affect the curve.

In light of the time dependence of the current traces, one way to present these data without obscuring the system's complexity is to plot the temporal response of the current ratio. Figure 5.7 shows the current traces measured for fluorescein solutions in both 0.1x TBE buffers (no PVP and 2% PVP) and the current ratio traces at different voltages. For the sake of clarity, only the data from experiments using voltages of ± 1 V, ± 5 V, and ± 20 V are displayed.

A couple of conclusions can be drawn from the results presented in Figure 5.7. First, the degree of ionic current rectification and concentration polarization was greater in the electrolyte solution containing PVP, as evidenced by the greater current ratios at all voltages for this solution (compare Figure 5.7 b and d). The addition of PVP suppresses EOF by dynamically coating the channel walls, increasing the viscosity near the surface.^{31,32} This

attenuation of the EOF affects the net mobility of both cations and anions, thus impacting the CP. Assuming the EOF is constant throughout the system, the differences in ion mobilities that result from a change in the EOF mobility are given by the following equations:

$$\mu_{noPVP}^+ = \mu_{PVP}^+ + \Delta\mu \quad (5.12)$$

and

$$\mu_{noPVP}^- = \mu_{PVP}^- - \Delta\mu \quad (5.13)$$

where $\Delta\mu$ is the difference in the EOF mobilities in the two solutions:

$\mu_{EOF,no PVP} - \mu_{EOF,PVP}$, which is a positive value. Substituting Equations 5.12 and 5.13 into Equation 5.11 gives:

$$\begin{aligned} \frac{J_m^+}{J_n^+}(noPVP) &= \frac{\mu_{PVP}^+ + \frac{1}{\beta_n} \mu_{PVP}^-}{\mu_{PVP}^+ + \mu_{PVP}^-} + \frac{\Delta\mu \left(1 - \frac{1}{\beta_n}\right)}{\mu_{PVP}^+ + \mu_{PVP}^-} \\ &= \frac{J_m^+}{J_n^+}(PVP) + \frac{\Delta\mu \left(1 - \frac{1}{\beta_n}\right)}{\mu_{PVP}^+ + \mu_{PVP}^-} \end{aligned} \quad (5.14)$$

This equation indicates that a greater contribution from EOF (observed, for example, when PVP is omitted from the buffer) results in the ratio, $\frac{J_m^+}{J_n^+}$, becoming closer to 1. This corresponds to lesser concentration polarization (and ionic current rectification). It should be noted that surface treatments that suppress EOF by neutralizing the surface charge of the nanofluidic conduits will further reduce concentration polarization by resulting in equivalent concentrations of cations and anions in the nanofluidic elements (i.e., $\beta_n = 1$).

A second conclusion that can be drawn from Figure 5.7 is that the current ratios evolve with time. In the case of the solution containing the EOF suppressor PVP (Figure 5.7 b), there is a gradual decrease in the current ratio over the course of the experiment. The

effect is more dramatic in the solution omitting PVP, where EOF is greater (Figure 5.7d). At ± 5 V and ± 20 V, the relative current magnitudes actually invert over the course of the experiment and the ratio drops below 1. This inversion is not accounted for in the models of concentration polarization introduced above, which are more appropriate for the initial system response. Instead, it reflects the asymmetric nature of the CP propagation and the dependence of propagation rates on voltage polarity.

5.4 Conclusion and Future Directions

Concentration polarization was studied in a nanochannel-nanofunnel system by the simultaneous measurement of dye fluorescence and ionic current. The current decrease of the system corresponded to the enrichment and depletion of charge carriers at the ends of the nanochannel and nanofunnel. During the course of these measurements, this enrichment and depletion did not reach an equilibrium state. Rather these regions propagated down the microchannels. The resistance thus kept increasing at an applied voltage. When a voltage with the same magnitude but different polarity was applied, both the magnitude and the changing rate of the resistance were different. The presence of the additive PVP affects this ratio and its temporal response.

It is clear from these initial experiments that additional investigations into the contribution of EOF are required to generate a complete understanding of these asymmetric nanofluidic systems. In the future, I would like to explore how the CP propagation is influenced by the EOF by running ion transport simulations. The knowledge developed would be used to direct the design of nanofluidic devices for biomolecule analyses (e.g., for analyte pre-concentration).

5.5 REFERENCES

1. Zangle, T. a, Mani, A. & Santiago, J. G. Theory and experiments of concentration polarization and ion focusing at microchannel and nanochannel interfaces. *Chem. Soc. Rev.* **39**, 1014–35 (2010).
2. Sparreboom, W., van den Berg, A. & Eijkel, J. C. T. Principles and applications of nanofluidic transport. *Nat. Nanotechnol.* **4**, 713 (2009).
3. Schoch, R., Han, J. & Renaud, P. Transport phenomena in nanofluidics. *Rev. Mod. Phys.* **80**, 839 (2008).
4. Plecis, A., Nanteuil, C., Haghiri-Gosnet, A.-M. & Chen, Y. Electropreconcentration with charge-selective nanochannels. *Anal. Chem.* **80**, 9542 (2008).
5. Bilenko, O. *et al.* Formation of a resistive region at the anode end in DNA capillary electrophoresis. *Electrophoresis* **24**, 1176 (2003).
6. Hlushkou, D., Dhopeswarkar, R., Crooks, R. M. & Tallarek, U. The influence of membrane ion-permselectivity on electrokinetic concentration enrichment in membrane-based preconcentration units. *Lab Chip* **8**, 1153 (2008).
7. Hatch, A. V, Herr, A. E., Throckmorton, D. J., Brennan, J. S. & Singh, A. K. Integrated preconcentration SDS-PAGE of proteins in microchips using photopatterned cross-linked polyacrylamide gels. *Anal. Chem.* **78**, 4976 (2006).
8. Song, S. & Singh, A. K. On-chip sample preconcentration for integrated microfluidic analysis. *Anal. Bioanal. Chem.* **384**, 41 (2006).
9. Dai, J., Ito, T., Sun, L. & Crooks, R. M. Electrokinetic trapping and concentration enrichment of DNA in a microfluidic channel. *J. Am. Chem. Soc.* **125**, 13026 (2003).
10. Pu, Q., Yun, J., Temkin, H. & Liu, S. Ion-enrichment and ion-depletion effect of nanochannel structures. *Nano Lett.* **4**, 1099 (2004).
11. Wang, Y.-C., Stevens, A. L. & Han, J. Million-fold preconcentration of proteins and peptides by nanofluidic filter. *Anal. Chem.* **77**, 4293 (2005).
12. Kim, S., Wang, Y.-C., Lee, J., Jang, H. & Han, J. Concentration Polarization and Nonlinear Electrokinetic Flow near a Nanofluidic Channel. *Phys. Rev. Lett.* **99**, 1 (2007).
13. Dhopeswarkar, R., Crooks, R. M., Hlushkou, D. & Tallarek, U. Transient effects on microchannel electrokinetic filtering with an ion-permselective membrane. *Anal. Chem.* **80**, 1039 (2008).

14. Mani, A., Zangle, T. a & Santiago, J. G. On the propagation of concentration polarization from microchannel-nanochannel interfaces. Part I: Analytical model and characteristic analysis. *Langmuir* **25**, 3898 (2009).
15. Zangle, T. a, Mani, A. & Santiago, J. G. On the propagation of concentration polarization from microchannel-nanochannel interfaces. Part II: Numerical and experimental study. *Langmuir* **25**, 3909 (2009).
16. Chun, H., Chung, T. D. & Ramsey, J. M. High Yield Sample Preconcentration Using a Highly Ion-Conductive Charge-Selective Polymer. *Anal. Chem.* **82**, 6287 (2010).
17. Helfferich, F. G. *Ion Exchange*. 1, 61 (New York, McGraw-Hill, 1962).
18. Peers A M. No Title. *Disc. Faraday Soc.* **21**, 124 (1956).
19. Wei, C., Bard, A. J. & Feldberg, S. W. Current Rectification at Quartz Nanopipet Electrodes. *Anal. Chem.* **69**, 4627 (1997).
20. Zaltzman, B. & Rubinstein, I. Electro-osmotic slip and electroconvective instability. *J. Fluid. Mech.* **579**, 173 (2007).
21. Siwy, Z., Heins, E., Harrell, C. C., Kohli, P. & Martin, C. R. Conical-nanotube ion-current rectifiers: the role of surface charge. *J. Am. Chem. Soc.* **126**, 10850 (2004).
22. Siwy, Z. & Fuliński, A. A nanodevice for rectification and pumping ions. *Am. J. Phys.* **72**, 567 (2004).
23. Diego, S. & Fresnel, B. X. Asymmetric pores in a silicon membrane acting as massively parallel brownian ratchets. *Nature* **424**, 53 (2003).
24. Karnik, R., Duan, C., Castelino, K., Daiguji, H. & Majumdar, A. Rectification of ionic current in a nanofluidic diode. *Nano Lett.* **7**, 547 (2007).
25. Vlassioug, I. & Siwy, Z. S. Nanofluidic diode. *Nano Lett.* **7**, 552 (2007).
26. Perry, J. M., Zhou, K., Harms, Z. D. & Jacobson, S. C. Ion transport in nanofluidic funnels. *ACS nano* **4**, 3897 (2010).
27. Hlushkou, D., Perry, J. M., Jacobson, S. C. & Tallarek, U. Propagating concentration polarization and ionic current rectification in a nanochannel-nanofunnel device. *Anal. Chem.* **84**, 267 (2012).
28. Hsieh, C.-C., Balducci, A. & Doyle, P. S. Ionic effects on the equilibrium dynamics of DNA confined in nanoslits. *Nano Lett.* **8**, 1683 (2008).

29. Inglis, D. W., Goldys, E. M. & Calander, N. P. Simultaneous concentration and separation of proteins in a nanochannel. *Angew. Chem. Int. Edit.* **50**, 7546 (2011).
30. The fluorescein solution in TBE is more complicated than this idealization, considering the presence of dianionic fluorescein, various borate constituents, and conjugate forms of EDTA.
31. Milanova, D., Chambers, R. D., Bahga, S. S. & Santiago, J. G. Effect of PVP on the electroosmotic mobility of wet-etched glass microchannels. *Electrophoresis* **33**, 3259 (2012).
32. Kaneta, T., Ueda, T., Hata, K. & Imasaka, T. Suppression of electroosmotic flow and its application to determination of electrophoretic mobilities in a poly(vinylpyrrolidone)-coated capillary. *J. Chromatogr. A* **1106**, 52 (2006).

5.6 Figures

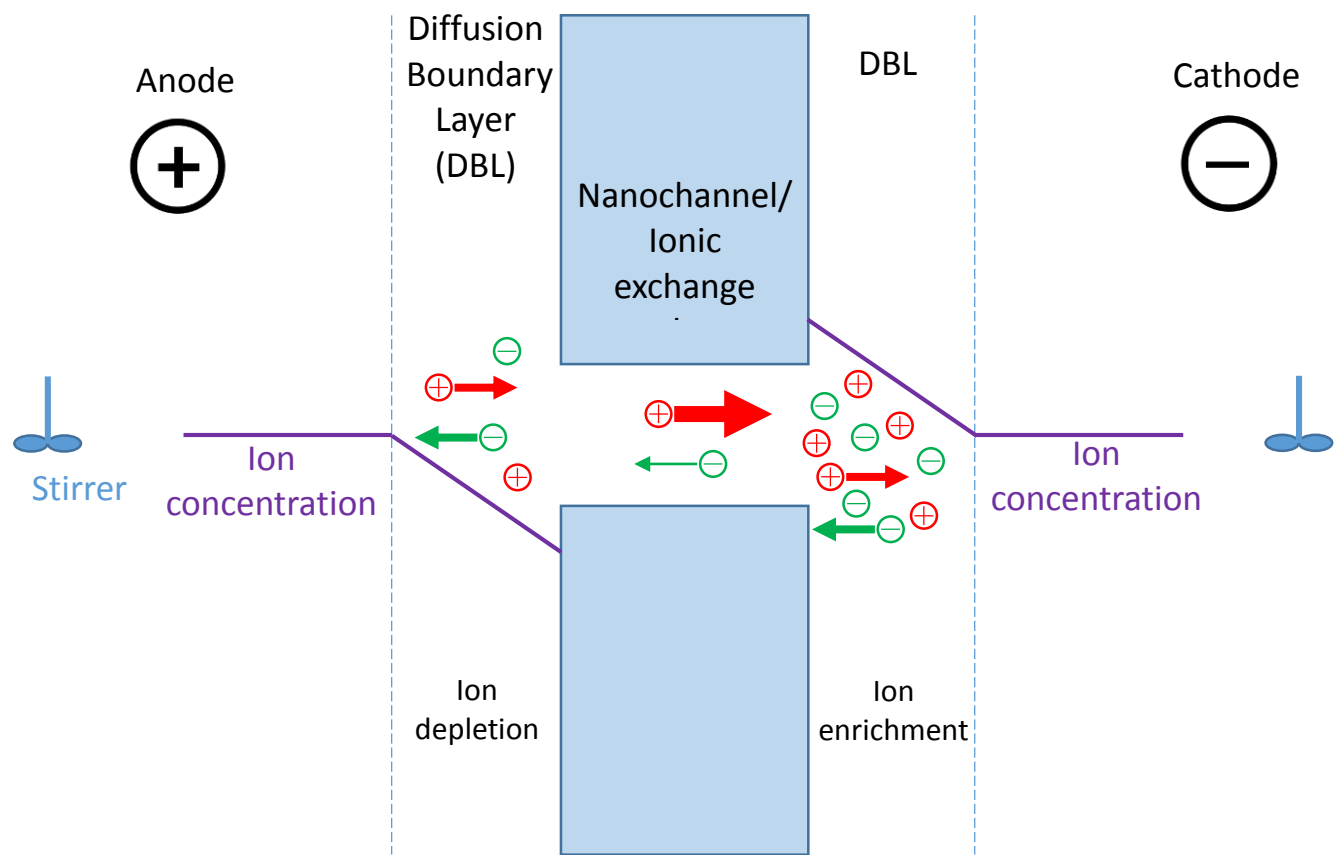


Figure 5.1 Schematic showing the concentration polarization. The depletion and enrichment in the DBL are caused by the ionic flux mismatch. The purple lines shows the ion concentration profile in the bulk and in the DBL. The size of the arrow shows the magnitude of the ion flux.

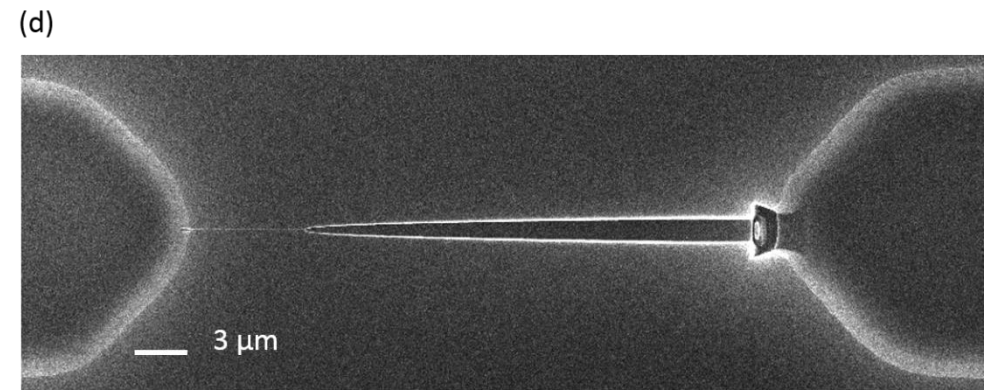
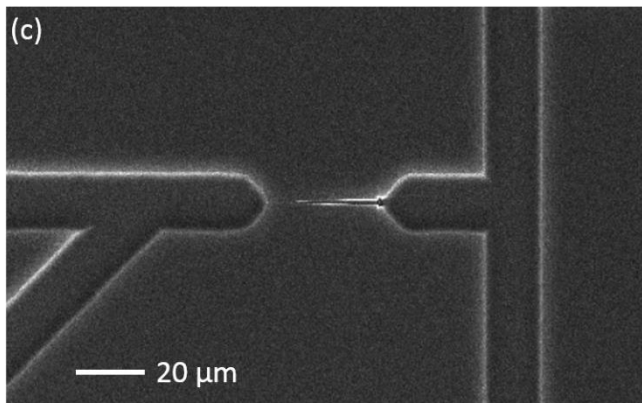
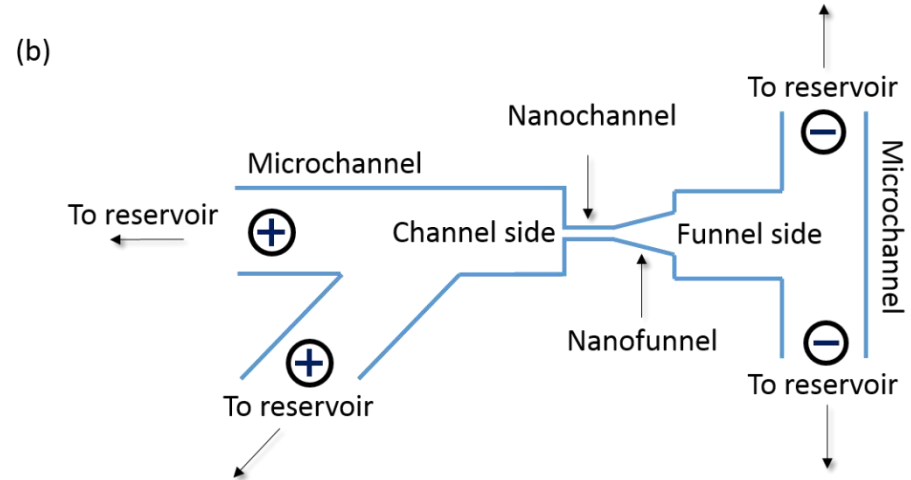
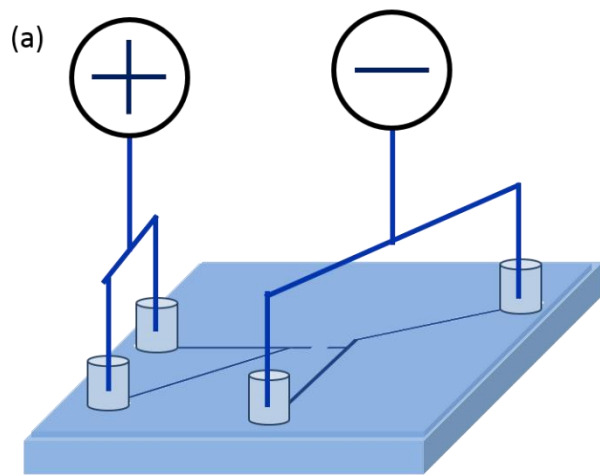


Figure 5.2 Experiment configurations. a) Schematic representation of the fluidic device and the microchannel patterns. b) Schematic representation of the geometry of the micro and nanochannels. c) SEM image of the channels. d) SEM image of the funnel and the nanochannel.

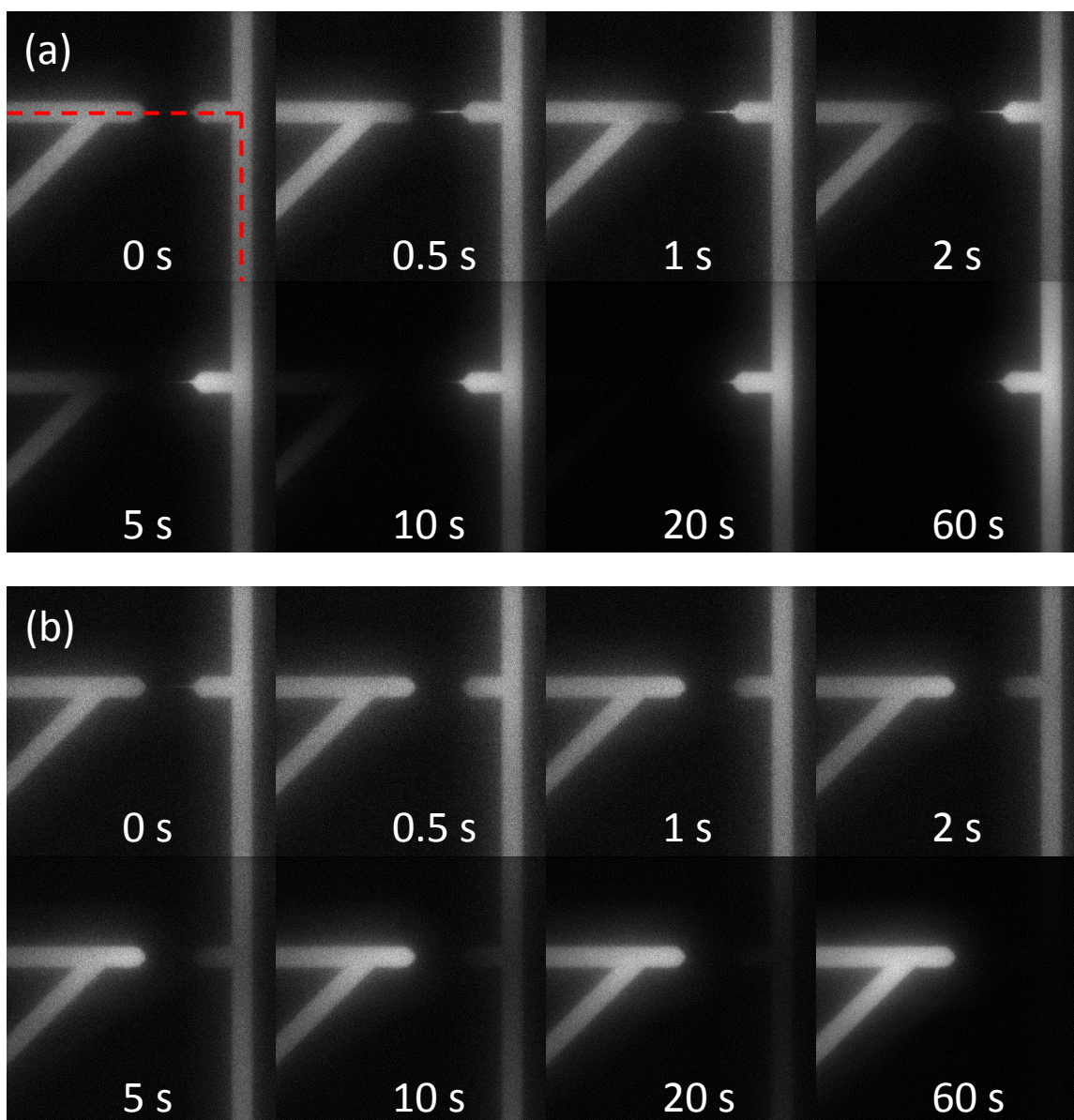


Figure 5.3 Fluorescence intensity change showing the concentration polarization under an electric field. The solution used is 0.1x TBE with 500 μ M fluorescein. A serial of images taken at 0, 0.5, 1, 2, 5, 10, 20, 60 seconds are shown. Zero second is defined when the voltage is applied. The microchannels are 17 μ m wide. The dashed line shows the path for extracting the intensity profile. **a)** 5 V is applied to the channel side (left) and funnel side (right) is ground. **b)** The voltage with a different polarity but the same magnitude is applied (-5 V).

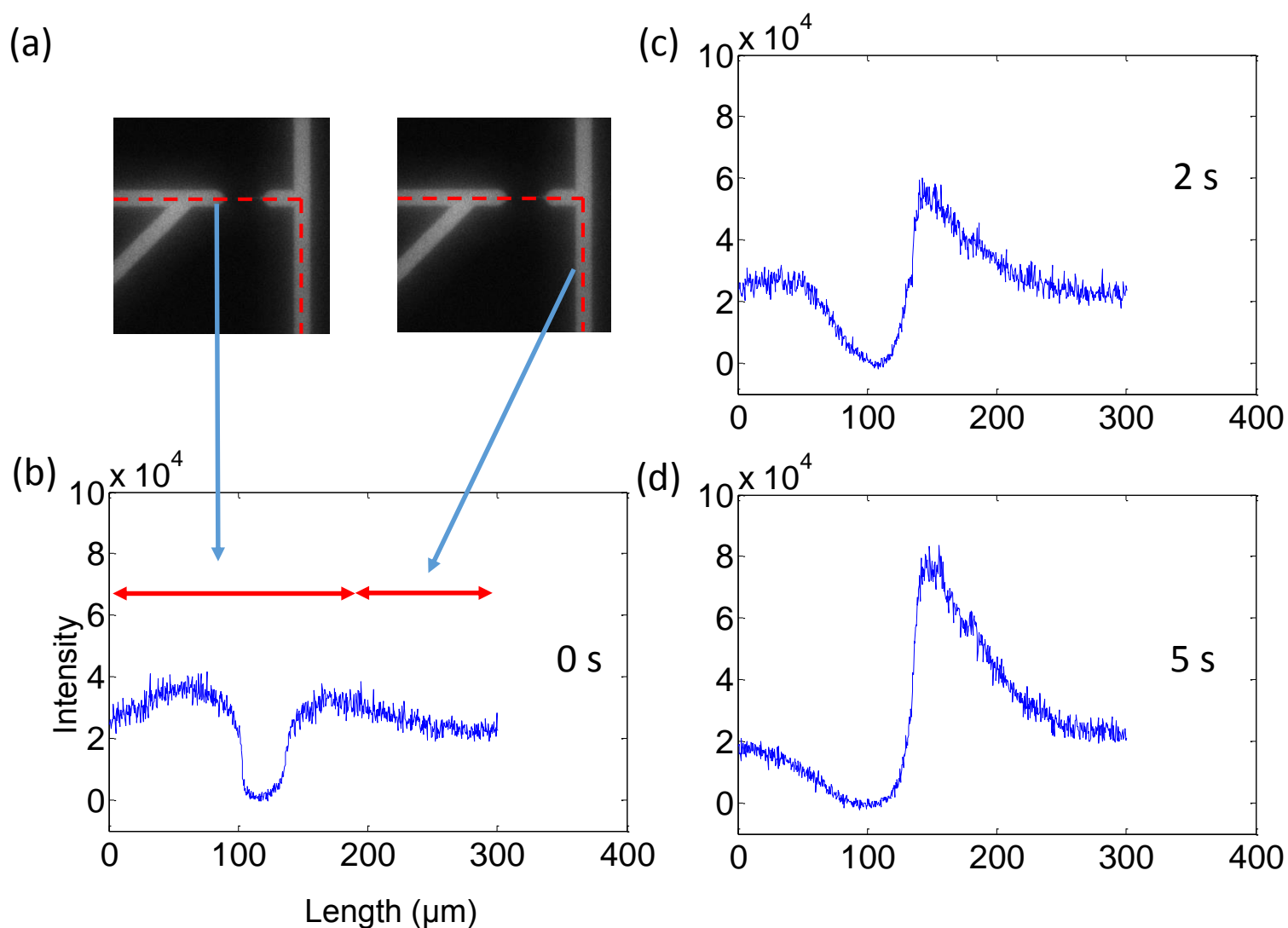


Figure 5.4 Data processing for constructing Figure 5.5. **a)** Frame at 0 s from Figure 5.3 a. **b)** The intensity profile scanned along the red dashed line in a. The arrows indicate the segments of the intensity profile that correspond to the orthogonal segments of the path in a. **c)** The intensity profile at 2 s. **d)** The intensity profile at 5 s.

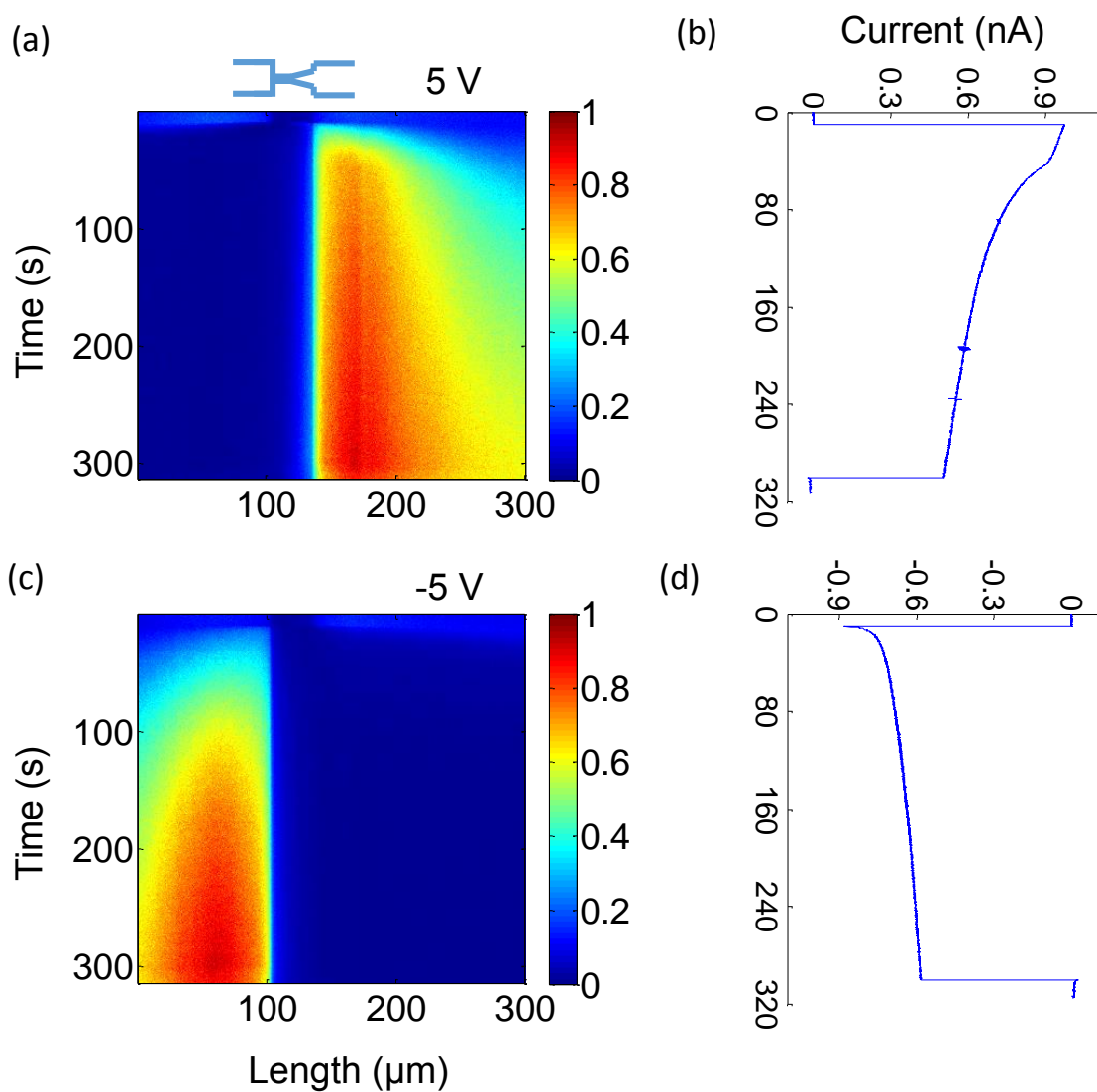


Figure 5.5 Simultaneous measurements of the optical and the electrical signal indicating concentration polarization. **a)** and **c)** Image plots of relative fluorescence intensity showing the change in fluorescein concentration. **b)** and **d)** Corresponding current changes over time. The voltage is zero at both the beginning and the end of the measurements. 0.1x TBE, no PVP. The schematic shows the location of the nanochannel-nanofunnel relative to position axis of the intensity plots. **a** and **b**: 5 V data. **c** and **d**: -5 V data.

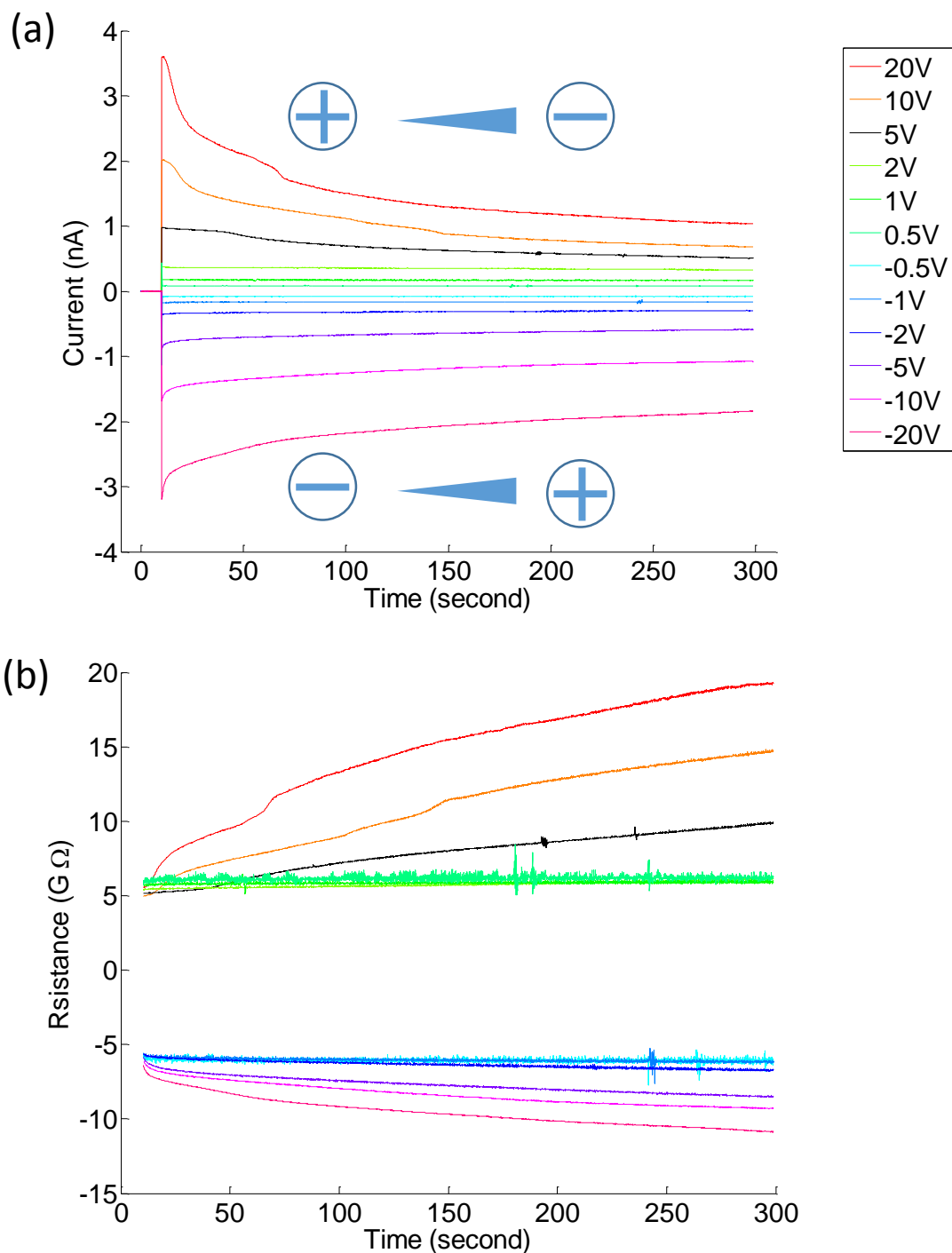


Figure 5.6 Current and resistance changes reflecting the CP propagation at different voltages for a solution of fluorescein in 0.1x TBE, no PVP. **a)** Current traces. **b)** Resistance traces. The schematic in **a** shows the polarity conventions corresponding to positive or negative currents.

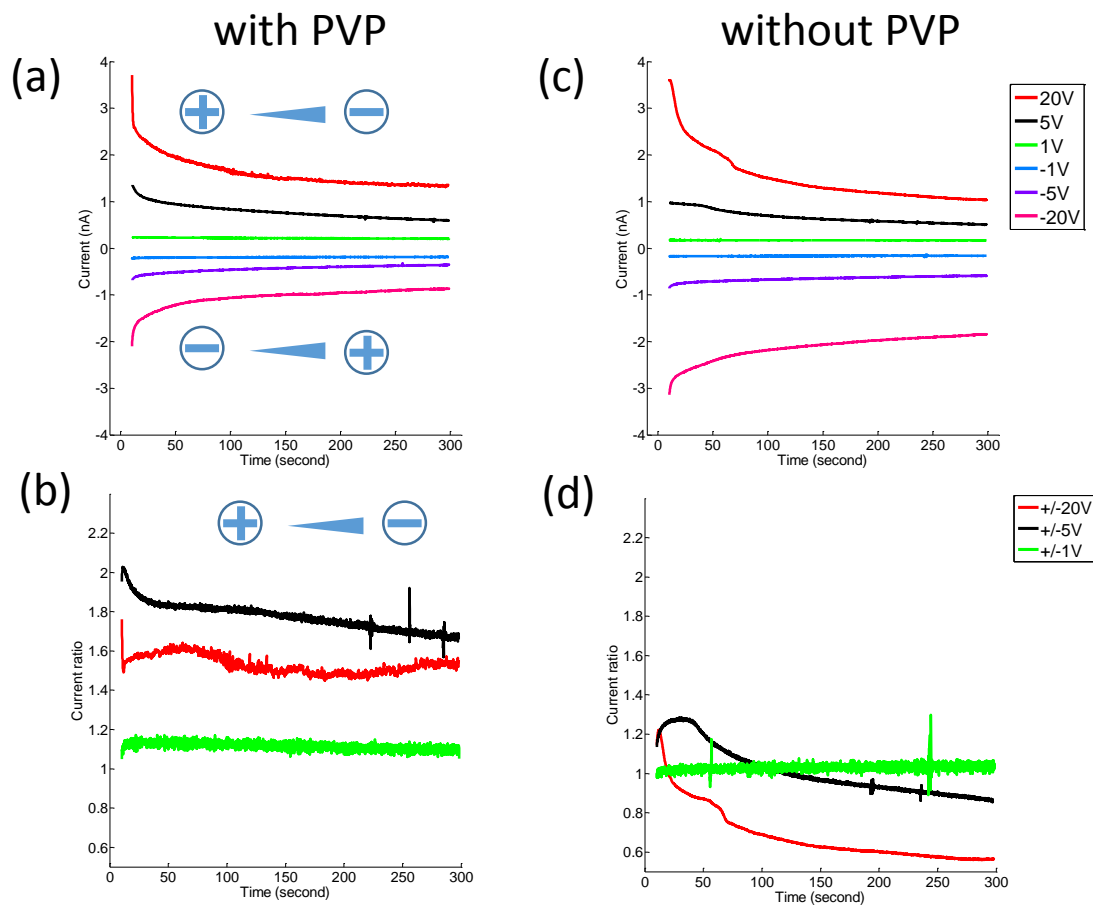


Figure 5.7 Current traces and current ratios showing the concentration polarization as affected by voltage and EOF. **a** and **b** show the results for a fluorescein solution in 0.1x TBE with 2% PVP. **c** and **d** show results for a fluorescein solution in 0.1x TBE without PVP. The schematics in **a** and **c** show the polarity conventions.